UCSF
UC San Francisco Electronic Theses and Dissertations

Title
Beige adipocyte maintenance is regulated by autophagy-induced mitochondrial clearance

Permalink
https://escholarship.org/uc/item/38k6n8m0

Author
Keylin, Svetlana

Publication Date
2016

Peer reviewed|Thesis/dissertation

eScholarship.org Powered by the California Digital Library
University of California

Beige adipocyte maintenance is regulated by autophagy-induced mitochondrial clearance

by

Svetlana Keylin

DISSERTATION

Submitted in partial satisfaction of the requirements for the degree of

DOCTOR OF PHILOSOPHY

in

Developmental and Stem Cell Biology

in the

GRADUATE DIVISION

of the

UNIVERSITY OF CALIFORNIA, SAN FRANCISCO

© Copyright 2016

by

Svetlana Keylin

Dedication

To my daughters, Gabriella and Elizabeth, to show that through hard work you can achieve anything.

To dedushka, the first scientist I knew.

Acknowledgements

I would like to express my gratitude to the individuals that contributed to the completion of this dissertation. First and foremost, I would like to thank my mentor, Shingo Kajimura, whose continuous guidance, support and enthusiasm had an eminent effect on my scientific development.

I am very grateful to the members of my dissertation committee, Michael German, Jay Debnath, and Todd Nystul for their time, knowledge, and invaluable advice on my project and beyond. I thank Jay for sharing his lab's resources with me and for being a great collaborator.

I have been fortunate to work with amazing people in the Kajimura lab throughout the years. In particular, I thank Kosaku for teaching me the basics of Bioinformatics analysis and for sharing numerous coffee and lunch sessions with me.

Most importantly, I am grateful to my family. I cannot thank my parents enough for being incredibly supportive of my career choice, for continuing to put my needs before their own, and for spending countless days, nights, weekends taking care of my kids. Thank you to my parents-in-law for always being there for me and for making the Sundays fun for the kids when I couldn't. Thank you to my sister for always being a great friend and a good listener. Thank you to my husband who has been my biggest fan during each step of graduate school, and whose patience, love, and support kept me sane and happy throughout the years.

Lastly, I'd like to thank my friends. Thank you to Sasha and Milla, who always know how to have a good time outside the lab. Thank you to Kathryn, Cass and Kevin for your encouragement and friendship both on the research front and personal front.

Contributions

Chapters 1 and 3 contain unpublished material that is currently under review in *Science Signaling*: Altshuler-Keylin S and Kajimura S. Mitochondrial homeostasis in adipose tissue remodeling. We thank Pema Maretich for constructive comments and edits of the manuscript.

Chapters 2 and 4 contain materials reproduced and modified from the following publication: Altshuler-Keylin S, Shinoda K, Hasegawa Y, Ikeda K, Hong H, Kang Q, Yang Y, Perera RM, Debnath J, Kajimura S. Beige adipocyte maintenance is regulated by autophagy-induced mitochondrial clearance. *Cell Metabolism* 24, 1–18 (2016).

Svetlana Keylin and Shingo Kajimura conceived the study, designed experiments, and analyzed and interpreted the data, and wrote the manuscript. Kosaku Shinoda performed bioinformatics analyses. Yutaka Hasegawa and Kenji Ikeda assisted with performing and interpreting the metabolic experiments. Haemin Hong and Qianqian Kang assisted with molecular analysis. Yangyu Yang provided technical help. Rushika Perera and Jay Debnath provided reagents and expertise in the field of autophagy and also edited the manuscript.

We are grateful to Dr. Luke Cassereau and Dr. Valerie Weaver at University of California, San Francisco for their help in developing the single-cell monitoring system, Anthony Jose from the FACS Core for his help in isolating mature adipocytes, Dr. Noboru Mizushima at the University of Tokyo for providing *GFP-LC3* mice and and *Atg5* $^{flox/flox}$ mice, Dr. Evan Rosen in Beth Israel Deaconess Medical Center and Harvard Medical School for providing *Ucp1* $^{Cre/+}$ mice and *Adiponectin* $^{Cre/+}$ mice, Dr. Christophe Paillart for his help in the CLAMS studies, and Larry Ackerman for his help with EM.

Beige adipocyte maintenance is regulated by autophagy-induced mitochondrial clearance

By Svetlana Keylin

Abstract

Beige adipocytes gained much attention as an alternative cellular target in anti-obesity therapy. While recent studies have identified a number of regulatory circuits that promote beige adipocyte differentiation, the molecular basis of beige adipocyte maintenance remains unknown. Here, we demonstrate that beige adipocytes progressively lose their morphological and molecular characteristics after withdrawing external stimuli, and directly acquire white-like characteristics bypassing an intermediate precursor stage. The beige-to-white adipocyte transition is tightly coupled to a decrease in mitochondria, increase in autophagy, and activation of MiT/TFE transcription factor-mediated lysosome biogenesis. The autophagy pathway is crucial for mitochondrial clearance during the transition; inhibiting autophagy by $UCP1^{+}$-adipocyte-specific deletion of *Atg5* or *Atg12* prevents beige adipocyte loss after withdrawing external stimuli, maintaining high thermogenic capacity and protecting against diet-induced obesity and insulin resistance. The present study uncovers a fundamental mechanism by which autophagy-mediated mitochondrial clearance controls beige adipocyte maintenance, thereby providing new opportunities to prevent obesity.

Table of contents

Chapter 1: Introduction……..……1

Introduction to beige adipocytes……..……..…1

Introduction to autophagy and mitophagy……4

Role of autophagy in adipose biology……..…11

Physiological regulation of autophagy in adipocytes.....…….....…….14

Pathological regulation of autophagy in metabolic disease……..……16

Methodologies for detecting mitophagy in adipocytes.....19

Chapter 2: Beige adipocyte maintenance is regulated by autophagy-induced mitochondrial clearance.....23

Chapter 3: Conclusions and future directions.....88

Chapter 4: Materials and methods.....93

References.....102

List of tables

Chapter 1: Introduction

Table 1. Overview of adipose tissue phenotypes in animals that lack autophagy-related genes.....13

Chapter 2: Beige adipocyte maintenance is regulated by autophagy-induced mitochondrial clearance

Supplementary table 1. Cluster 1 gene list and associated membership values.....81

Supplementary table 2. qRT-PCR primers.....87

List of figures

Chapter 1: Introduction

Figure 1. Beige adipocyte development.....3

Figure 2. Regulation of mitochondrial dynamics.....8

Figure 3. Overview of the autophagy and mitophagy pathways.....9

Chapter 2:

Figure 1. Beige adipocytes directly acquire morphological characteristics of white adipocytes after withdrawing external stimuli.....46

Figure 2. Beige adipocytes directly acquire molecular characteristics of white adipocytes after withdrawing external stimuli.....49

Figure 3. Beige-to-white adipocyte transition is accompanied by mitochondrial clearance.....52

Figure 4. Activation of autophagy during the beige-to-white adipocyte transition.....54

Figure 5. Regulation of autophagy-related lysosome biogenesis through MiT/TFE transcription factors during the beige-to-white adipocyte transition.....57

Figure 6. Genetic ablation of *Atg12* or *Atg5* maintains beige adipocyte characteristics after removal of ß3-AR agonist.....60

Figure 7. Maintenance of beige adipocytes by autophagy inhibition protects animals from diet-induced obesity and insulin resistance.....63

Supplementary Figure 1. The experimental system to monitor brown and beige adipocytes *in vivo.*.....66

Supplementary Figure 2. Time-dependent decline in endogenous UCP1 expression in the inguinal WAT after withdrawal of external cues.....67

Supplementary Figure 3. Ex vivo system to track morphological and functional changes of beige adipocytes.....68
Supplementary Figure 4. Gene expression profile of beige adipocytes and BAT following β3-AR agonist withdrawal.....69
Supplementary Figure 5. Morphological evidence of mitophagy in beige adipocytes following β3-AR agonist withdrawal.....70
Supplementary Figure 6. Measuring autophagic flux in beige adipocytes.....71
Supplementary Figure 7. Regulation of *Foxo3* expression in beige adipocytes.....72
Supplementary Figure 8. Molecular characterization of the inguinal WAT depots in *Atg12*^{Ucp1} KO mice and *Atg5*^{Ucp1} KO mice.....73
Supplementary Figure 9. Phenotype of the interscapuar BAT depots in *Atg12*^{Ucp1} KO mice.....74
Supplementary Figure 10. Phenotype of the interscapuar BAT depots in *Atg5*^{Ucp1} KO mice.....75
Supplementary Figure 11. Genetic and pharmacological inhibition of autophagy promotes beige adipocyte maintenance after withdrawal of external cues.....76
Supplementary Figure 12. Metabolic phenotype of *Atg12*^{Ucp1} KO mice.....78
Supplementary Figure 13. Morphological analysis of classical brown adipocytes under obesity.....79
Supplementary Figure 14. Metabolic characterization of *Atg12*^{Ucp1} KO mice in the absence of β3-AR agonist treatment.....80
Chapter 3: Conclusions and future directions
Figure 1. Cross-talk between mTOR and β3-AR pathways in beige adipocytes.....90

Chapter 1: Introduction

Introduction to beige adipocytes.

Mammals possess two functionally distinct types of adipocytes: white adipocytes which store excess energy as triglycerides, and brown adipocytes which dissipate energy in the form of heat and whose presence can counteract obesity and obesity-associated diseases, such as type 2 diabetes (Sidossis and Kajimura, 2015). Recent studies indicate that adult humans and rodents have a 'recruitable' form of brown adipocytes, termed 'beige adipocytes', whose development can be induced by certain environmental stimuli, such as chronic cold exposure (Shinoda et al., 2015; van der Lans et al., 2013; Yoneshiro et al., 2013). Notably, beige adipocytes revert to white adipocytes shortly after the requisite stimuli are removed.

While brown and beige adipocytes possess similar biochemical and morphological characteristics, including expression of uncoupling protein 1 (UCP1), high mitochondrial contents, and multilocular lipid droplets, their developmental origins are distinct (Frontini and Cinti, 2010; Lidell et al., 2013; Petrovic et al., 2010; Sharp et al., 2012; Shinoda et al., 2015; Wu et al., 2012). Brown adipocytes, whose development is stalled during postnatal stages, arise early during development from a subset of dermomyotome precursors. On the other hand, beige adipocytes arise postnatally in response to environmental cues from *Ebf2*, *Pdgfr*α, and *Sca1* precursors (Lee et al., 2012; Schulz et al., 2011; Wang et al., 2014) (**Figure 1**). Cold exposure which activates the β3-adrenergic receptor (β3AR) signaling pathway, is a dominant activator of brown/beige adipocyte development. Transcriptional co-regulator PRDM16 together with C/EBPs,

PGC1α, EBF2 and PPARα, promotes transcription of beige adipocyte genetic program (Inagaki et al., 2016). Interestingly, within 2-3 weeks of absence from prolonged cold exposure or a β3-AR agonist, beige adipocytes lose their thermogenic molecular characteristics, acquire large lipid droplets, resembling white adipocytes and express genetic signature of white-adipocytes (Rosenwald et al., 2013). Given the crucial role of the mitochondria in the function of beige, brown, or white adipocytes, it is important to understand the mechanisms involved in regulating mitochondrial homeostasis.

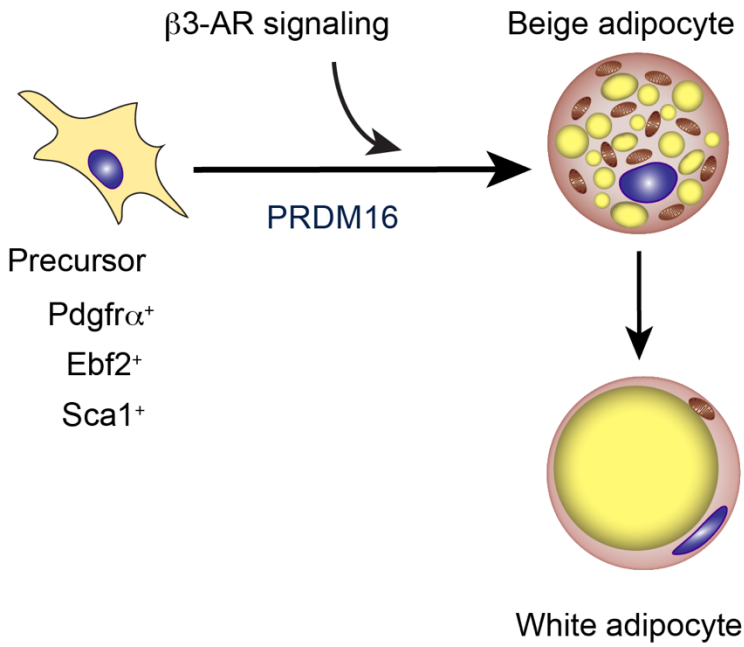

Figure 1. Beige adipocyte development. Activation of β3-adrenergic receptor (β3-AR) signaling, stimulated by cold exposure or β3-AR agonists, induces differentiation of precursors into UCP1+ beige adipocytes. Upon withdrawal of the cue, beige adipocytes convert to white adipocytes.

Introduction to autophagy and mitophagy.

Mitochondria are double-membrane organelles that serve as the major source of ATP: the coenzyme with which cells carry out various functions. The cell must undergo both mitochondrial biogenesis and mitochondrial degradation to maintain homeostasis and appropriately respond to the varying energetic demands of the cell (Figure 2). On one end, mitochondrial biogenesis is tightly regulated by a number of transcriptional regulators coded in the nucleus, including *PGC-1α, Nrf1/2*, and *Tfam*. Transcriptional control of mitochondrial biogenesis has been discussed in great detail in the cited review (Kelly and Scarpulla, 2004). On the other end, mitochondrial degradation is carried out through autophagy. Autophagy is a method of intracellular degradation to break down unwanted or damaged cellular components. A main hallmark of autophagy that distinguishes it from other degradation processes, is the formation of a double-membrane vesicle, the autophagosome, to deliver large cytoplasmic components to the lysosome for degradation. The detailed processes of autophagosome formation are described elsewhere (Lamb et al., 2013; Mizushima and Komatsu, 2011). Figure 3a summarizes the key components of autophagy. In short, the molecular signal from the mammalian target of rapamycin complex 1 (MTORC1) triggers activation of unc-51 like autophagy activating kinase 1 (ULK) complex, consisting of ULK1, ATG13, and FIP200, to initiate formation of the isolation membrane from existing membrane sources such as ER or Golgi. The membrane further expands to produce a completely enclosed, double-membraned vesicle, known as the autophagosome. Autophagosome formation is orchestrated by a number of core autophagy-related (ATG) proteins. A key step for

autophagosome formation is the conjugation of phosphatidylethanol- amine (PE) to microtubule-associated protein 1 light chain 3 (LC3), an ATG8 homolog, to generate a lipidated form of LC3, LC3-PE. This conjugation is mediated in part by ATG7 and ATG5-ATG12-ATG16L1 complex (Lamb et al., 2013). LC3 is retained inside the autophagosome and serves as a common marker of autophagy (e.g. GFP-LC3) (Mizushima, 2009). Once the autophagosome is developed, it fuses with the lysosome, forming an autolysosome: a single-membraned acidic vesicle where lysosomal hydrolytic enzymes, such as cathepsins, degrade the enclosed contents. Lysosome biogenesis is an important component of autophagy machinery and has been recently shown to be regulated by MiT/TFE family of transcription factors, including MITF, TFEB, TFE3 (Palmieri et al., 2011; Perera et al., 2015; Sardiello et al., 2009; Settembre et al., 2011).

Though the later elements of the autophagy machinery are pivotal in regulation of degradation, the initial selective degradation of cytoplasmic components through autophagy is worth exploring in depth. A particularly interesting example is mitophagy, the selective clearance of mitochondria via autophagy. Selectivity is driven by specific proteins that physically connect the intended target (e.g. mitochondria) with the autophagosomal protein LC3. These receptors interact with the autophagosome through the LC3-interacting region (LIR) (Figure 3b). Mitochondrial damage is a major physiological trigger for selective mitochondrial clearance. Damage-induced mitophagy can occur through two different mechanisms: 1) adapter-mediated, ubiquitin-dependent mitophagy, and 2) direct, ubiquitin-independent mitophagy (Figure 3b). Adapter-mediated mitophagy, regulated by PTEN-induced putative kinase 1 (PINK1) and the E3 ubiquitin ligase Parkin, depends on ubiquitination of the target. Damage to the mitochondria leads

to reduced mitochondrial membrane potential, stabilization of PINK1 on the outer mitochondrial membrane, and subsequent recruitment of Parkin, which ubiquitinates outer mitochondrial proteins (Narendra et al., 2010). The ubiquitinated substrates are then recognized by a number of autophagy adapter proteins (including p62, Optineurin, NDP52, and NBR1) that link the ubiquitinated targets to LC3 (Heo et al., 2015; Kirkin et al., 2009; Lazarou et al., 2015; Sarraf et al., 2013). Adapter proteins contain two defining domains: a ubiquitin-binding domain for cargo recognition and a LIR domain that interacts with LC3 to promote encapsulation by the autophagosome. Whether adapter proteins have tissue specific/cell type specific functions have yet to be revealed.

Damage-induced mitophagy can also occur through direct interaction of mitochondria-localized proteins with LC3, independent of ubiquitination. For example, Bcl2/E1B 19 kDa-interacting protein 3 (BNIP3) and FUN14 domain-containing protein 1 (FUNDC1) directly interact with LC3 to promote mitophagy in response to hypoxia-triggered mitochondrial damage (Hanna et al., 2012; Liu et al., 2012). A newly identified mitophagy receptor, BCL2L13, a mammalian homolog of Atg32, directly interacts with LC3 through the LIR domain. The mechanism that activates BCL2L13 remains to be determined (Murakawa et al., 2015).

Though fewer models have been established, mitophagy can take place independent of mitochondrial damage during developmental processes. For instance, NIX (BNIP3L), a BNIP3 homolog, is required for mitochondrial clearance during erythrocyte maturation (Mortensen et al., 2010; Zhang et al., 2009a). NIX mediates mitophagy in ubiquitin-independent manner: blocking the direct interaction between NIX

and LC3 leads to accumulation of mitochondria in maturing erythrocytes (Novak et al., 2010).

Additionally, mitochondrial degradation occurs when sperm mitochondria is removed during fertilization. Interestingly, the mechanism of paternal mitochondrial degradation is not conserved between species. In C. *elegans*, this process requires autophagosome formation and is independent of ubiquitination (Rawi et al., 2011; Sato and Sato, 2011). In *Drosophila*, paternal mitophagy also requires autophagosome formation although it is ubiquitin dependent, and requires p62, but does not require PARKIN (Politi et al., 2014). Examples in *C. elegans* and *Drosophila* suggest that there are uncharacterized proteins that target mitochondria for degradation. In mammals, including the mouse, pig, and rhesus monkey, mitochondrial degradation appears to occur through the ubiquitin-proteosome system, independent of LC3-mediated autophagy (Song et al., 2016; Sutovsky et al., 2000; Thompson et al., 2003).

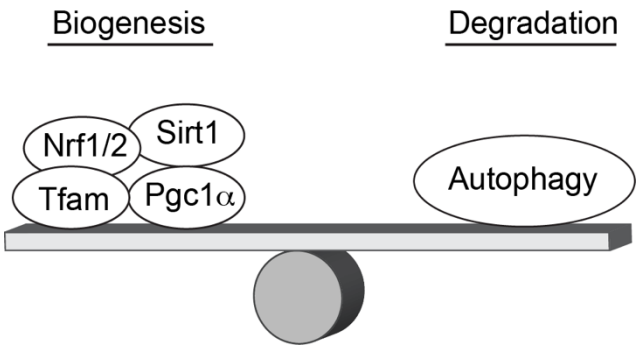

Figure 2. Regulation of mitochondrial dynamics. Mitochondrial content is regulated by a balance between mitochondrial biogenesis and degradation. Nuclear-coded transcriptional regulators, such as PGC1α, NRF1/2, and TFAM control mitochondrial biogenesis, whereas autophagy removes damaged or unwanted mitochondria.

Figure 3

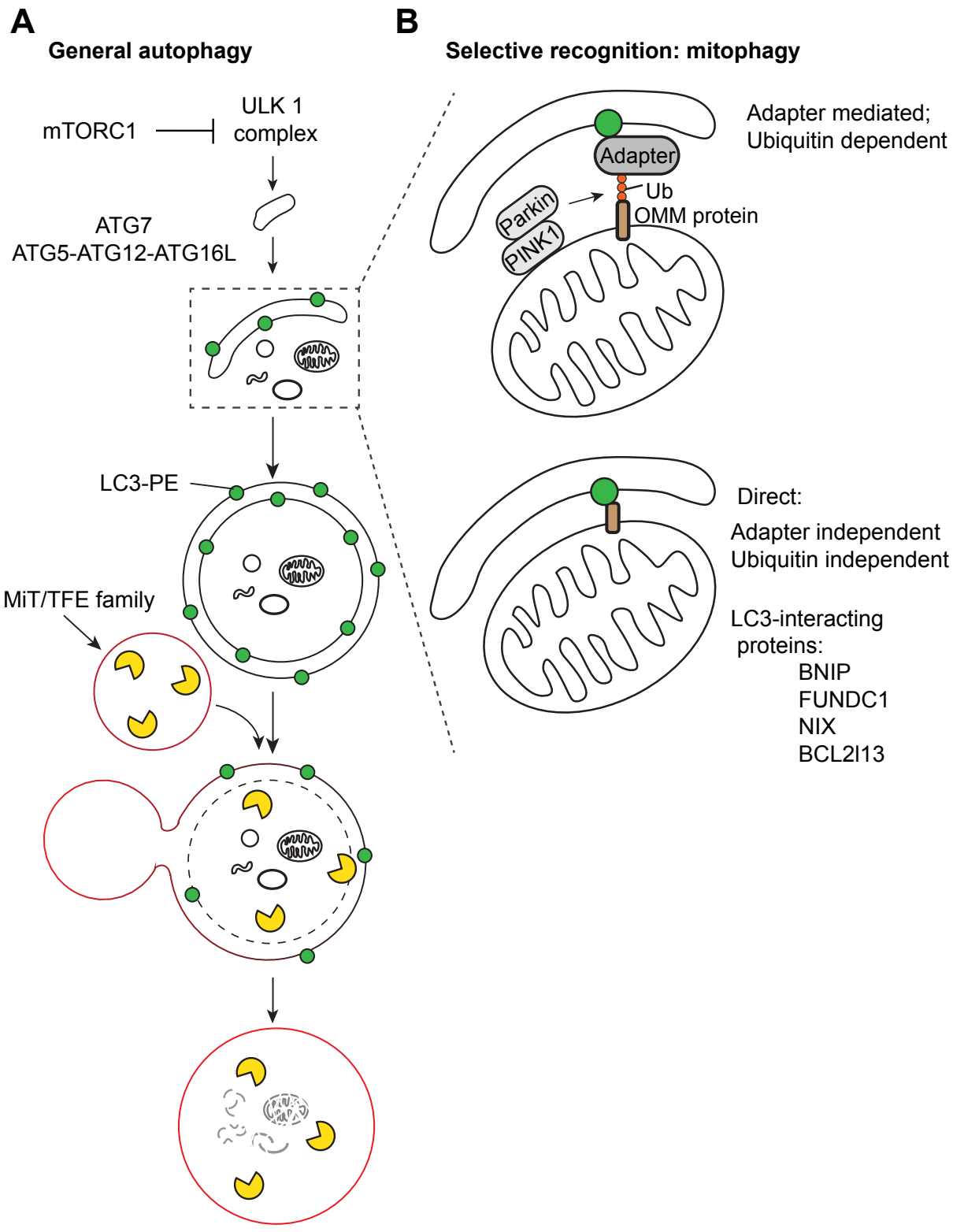
A
General autophagy
mTORC1
ULK 1
complex
ATG7
ATG5-ATG12-ATG16L
LC3-PE
MiT/TFE family
B
Selective recognition: mitophagy
Adapter
Ub
OMM protein
Parkin
PINK1
Adapter mediated;
Ubiquitin dependent
Direct:
Adapter independent
Ubiquitin independent
LC3-interacting
proteins:
BNIP
FUNDC1
NIX
BCL2l13

Figure 3. Overview of the autophagy and mitophagy pathways. (A) Autophagy begins with the formation of the isolation membrane. Initiation of the isolation membrane requires ULK1 complex, which is regulated by mTORC1. The isolation membrane then encloses cytosolic components and elongates to completely enclose and form the autophagosome. The elongation and closure of the autophagosome involves two ubiquitin-like conjugation systems: one forms the ATG5-ATG12-ATG16L complex and the other one forms the phosphatidyl-ethanolomine (PE) conjugated LC3 or LC3-PE. LC3-PE is required for autophagosome formation and serves as a marker of autophagy. Subsequently, the autophagosome fuses with the lysosome and the enclosed components are degraded by the lysosomal enzymes. MiT/TFE family of transcription factors regulates transcription of the lysosomal autophagy genes. **(B)** Selective mitochondrial degradation, or mitophagy, relies on autophagy receptors that are able to interact with LC3-PE proteins (green). In adapter mediated, ubiquitin dependent mitophagy (top), PINK1 stabilization recruits Parkin and promotes ubiquitination of outer mitochondrial proteins. Ubiquitin chains are recognized by adapter proteins that also contain the LC3 interacting region (LIR) and promote encapsulation of the mitochondria by the autophagosome. In adapter independent, ubiquitin independent mitophagy, specific mitochondrial proteins directly interact with LC3. Several such proteins have been identified. Abbreviations: Ub, ubiquitin; OMM, outer mitochondrial proteins.

Role of autophagy in adipose biology.

Autophagy has been implicated in remodeling mitochondrial content and thus regulating adipogenesis as well as mature adipocyte function. Understanding the development and maintenance of brown and beige adipocytes at a cellular level is critical for understanding the particular role of autophagy in energy homeostasis.

To determine the functional role of autophagy in terminally differentiated adipocytes, it is important to use an appropriate Cre mouse line that can target specific cell types and differentiation stage of adipocytes. In fact, several genetic autophagy-deficient animal models have been reported to study the function of autophagy in adipose tissues, but exhibit inconsistent phenotypes (Table 1). For instance, a total knockout of *Atg5* results in a differentiation defect of WAT, whereas deletion of *Atg7* via muscle and brown adipocyte specific Cre, *Myf5*-Cre, affects brown adipocyte differentiation (Baerga et al., 2009; Martinez-Lopez et al., 2013). These models assess the role of autophagy during adipogenesis and preclude from understanding autophagy function in terminally differentiated adipocytes. Additionally, *aP2*-Cre mediated deletion of *Atg7* or *p62* affects not only mature brown and white adipocytes but also some non-adipose tissues (Müller et al., 2013; Singh et al., 2009b; Zhang et al., 2009b). Unspecific expression of *aP2*-Cre in skeletal muscle, liver, and the brain can cause indirect effects on adipocyte differentiation and/or function (Mullican et al., 2013). In fact, inhibiting autophagy in POMC neurons and skeletal muscle is known to cause browning of white adipose tissue (Kim et al., 2013; Martinez-Lopez et al., 2013).

Yet another potential cause for the variety of phenotypes observed in autophagy-deficiency models may reside in the promiscuity of autophagy machinery components,

many of which have broad cellular functions beyond autophagy (Subramani and Malhotra, 2013). Deletion of Atg7 via *ap2*-Cre resulted in increased mitochondrial content and increased UCP1 expression in inguinal WAT and BAT (Singh et al., 2009b; Zhang et al., 2009b). In contrast, deletion of *p62*, a cargo receptor that mediates selective autophagy, via *ap2*-Cre, resulted in impaired mitochondrial function including reduced UCP1 expression in both BAT and inguinal WAT (Müller et al., 2013). These apparently conflicting phenotypes can be explained by the fact that *p62* functions in various signaling pathways, including NF-kB, ERK, and Nrf2 (Komatsu et al.; Moscat et al., 2007). Assessing multiple components of the autophagy process by using the mature adipocyte-specific Cre lines, such as Adiponectin-Cre or UCP1-Cre, would clarify the specific biological processes that are regulated specifically by each autophagy regulator.

Table 1. Overview of adipose tissue phenotypes in animals that lack autophagy-related genes.

Molecule	System	Adipocyte phenotype	References
Atg5	Total KO	Impaired development of WAT	(Baerga et al., 2009)
Atg5	MEFs in-vitro	Impaired differentiation, white adipocytes	(Baerga et al., 2009)
Atg5	*Ucp1*-Cre	Beige adipocyte maintenance; mitochondria and UCP1 retention;	(Altshuler-Keylin et al., 2016)
Atg7	*aP2*-Cre	Reduced WAT, increased mitochondrial content, small lipid droplets, resemble beige adipocytes	(Singh et al., 2009b; Zhang et al., 2009b)
Atg7	*Mlclf*-Cre	Deletion in skeletal muscle induces browning of WAT	(Kim et al., 2013)
Atg7	POMC-Cre	Deletion in POMC neurons induces browning of WAT	(Martinez-Lopez et al., 2015)
Atg12	*Ucp1*-Cre	Beige adipocyte maintenance; mitochondria and UCP1 retention; prevents diet-induced obesity and insulin resistance	(Altshuler-Keylin et al., 2016)
p62	total KO	Enlarged adipocytes due to lipid accumulation, obesity, obesity, glucose intolerance, decreased insulin sensitivity	(Rodriguez et al., 2006)
p62	*aP2*-Cre	Accumulation of defective mitochondria, increased lipid droplets in BAT, obesity, glucose intolerance, decreased insulin sensitivity	(Müller et al., 2013)
Parkin	total KO	Resistant to HFD induced obesity; reduced lipid accumulation in epiWAT and BAT on HFD	(Kim et al., 2011)
Raptor	*Adiponectin-Cre*	Disrupted browning of WAT in response to chronic cold	(Liu et al., 2016)

Physiological regulation of autophagy

Autophagy and biogenesis occur in concordance with response to nutrient availability and are thus tightly regulated by the mTORC1 complex of the mTOR signaling pathway, which acts as a nutrient sensor to coordinate cellular response (**Part 3, Figure 1**). Abundance of nutrients leads to activation of mTORC1 and its downstream targets, including S6K1 to promote protein synthesis for anabolic functions. In the absence of nutrients, mTORC1 is inhibited, leading to autophagy activation through regulation of ULK1, FIP200, ATG13 complex (Laplante and Sabatini, 2009).

Yet another form of physiological regulation is β3-AR signaling: a key mediator of beige adipocyte biogenesis in the face of cold exposure, it has recently been shown to block autophagy in beige adipocytes. Beige adipogenesis occurs when environmental cues, such as cold exposure, trigger the release of norepinephrine (NE) from the sympathetic nervous system, which in turn acts on the β3-AR, leading to increased cellular levels of cAMP, activation of protein kinase A (PKA), and subsequent transcription of the thermogenic program (Kajimura and Saito, 2013). In response to cold or β3-AR stimulation, PKA also activates MTORC1, a major regulator of autophagy. Mechanistic analysis revealed that PKA directly phosphorylates mTOR and its partner, RAPTOR, to promote mTORC1 activity (Liu et al., 2016). This data suggests that PKA-mTORC1 signaling axis concurrently regulates beige adipocyte development and autophagy.

It is also worth mentioning that the cAMP-PKA signaling pathway has been implicated in regulating adipocyte lipophagy. Lipophagy is a selective degradation of lipids by autophagy and has been first demonstrated in hepatocytes in 2009, where pharmacological and genetic inhibition of autophagy in cultured hepatocytes lead to

increased triglyceride accumulation (Singh et al., 2009a). Thus far, lipophagy has been implicated in hepatocytes and hepatic stellate cells, neurons, and brown adipocytes (Hernández-Gea et al., 2012; Kaushik and Cuervo, 2016; Kaushik et al., 2011; Martinez-Vicente et al., 2010; Seok et al., 2014). Two recent studies showed that lipophagy in brown adipocytes is regulated by cold exposure. In one study, chronic cold exposure inhibited lipophagy and associated autophagy components though the cAMP – PKA signaling pathway (Cairó et al., 2016). In a different study, however, acute cold exposure activated autophagy-mediated lipid degradation (Martinez-Lopez et al., 2015). The inconsistent results could potentially be attributed to differences in cold treatments. An aspect of concern is the shortage of tools to monitor lipophagy, making it difficult to assess selective lipophagy. The biological significance of lipophagy over lipolysis for lipid breakdown awaits future studies.

Pathological regulation of autophagy in metabolic disease

Autophagy plays a central role in the function and maintenance of metabolic tissues such as liver, pancreas, and adipose tissues. Emerging evidence suggests that dysregulation of autophagy contributes to the initiation or progression of metabolic disorders in the following organs.

Adipocytes:

Obesity in humans is associated with blunted metabolic activity of thermogenic adipocytes in response to cold exposure (Orava et al., 2013). Beige adipocyte development is impaired in obese mice due to activation of negative regulators such as TGF-β signaling and Notch signaling (Sidossis and Kajimura, 2015). Blockade of TGF-β signaling or Notch signaling pathways by genetic or pharmacological approaches promotes beige adipocyte biogenesis and protects mice from diet-induced obesity (Bi et al., 2014; Samad et al., 1997; Yadav et al., 2011). Furthermore, autophagy negatively regulates beige adipocyte development. Inhibiting autophagy through deletion of *Atg7* in adipocytes leads to increased browning of white adipose tissue, resistance to diet-induced obesity and improved insulin sensitivity (Singh et al., 2009b; Zhang et al., 2009b). Of note, upregulation of adipose autophagy has been observed in human obesity and type 2 diabetes (Jansen et al., 2012; Kovsan et al., 2011; Nuñez et al., 2013; Ost et al., 2010). Additionally, activation of autophagy in human subjects with T2D and obesity is party attributed to repression of mTORC1 activity (Ost et al., 2010). Whether beige adipocyte maintenance is dysregulated under obesity is unclear.

Pancreas:

Defects in pancreatic islet β-cell function and insulin sensitivity are the fundamental cause for type 2 diabetes. Pancreatic β-cells rely heavily on mitochondria and endoplasmic reticulum (ER) to maintain glucose-stimulated insulin production and secretion. Autophagy plays a protective role in regulating β-cell homeostasis by removing damaged mitochondria and/or ER. β-cell-specific deletion of *Atg7* resulted in accumulation of defective mitochondria and distended ER, leading to an impaired glucose tolerance and reduced insulin secretion (Ebato et al., 2008; Jung et al., 2008). Interestingly, autophagy deficient β-cells fail to proliferate in order to adapt to increased insulin demand in obesity (Jung et al., 2008; Quan et al., 2012). The mechanism by which autophagy controls β-cell cycle remains unclear.

A limited number of studies investigated the metabolic consequences of dysfunctional mitophagy in β-cells. Total Parkin null mice display reduced insulin secretion following glucose challenge under pathological stress conditions such as streptozotocin (STZ) exposure, whereas Parkin overexpression in pancreatic β-cell lines maintains insulin secretion under diabetic conditions (Hoshino et al., 2014). Additionally, C-type lectin domain family 16 member A (Clec16a) was recently implicated in β-cell mitophagy through a Parkin-dependent mechanism. Pancreas-specific deletion of *Clec16a* using *Pdx1*-Cre leads to accumulation of abnormal mitochondria, impaired glucose tolerance and insulin secretion in response to glucose challenge. Surprisingly, these *Clec16a* deficient pancreas exhibited an increase in Parkin expression, questioning the role of Parkin in regulating mitophagy in β-cells. Even though the role of Parkin in β-

cell mitophagy remains unclear, these results emphasize that that dysfunction in selective mitophagy alone could lead to β-cell failure and diabetes.

Liver:

Obesity is closely associated with hepatic steatosis. It has been reported that mice under diet-induced obesity or a genetic form of obesity (ob/ob) display reduced hepatic autophagy, as assessed by decreased number of GFP-LC3 puncta, reduced LC3-II expression and accumulation of p62 (Yang et al., 2010). Liver-specific deletion of *Atg7*, *Vps34*, or *Tfeb* results in lipid accumulation and enlarged livers (Jaber et al., 2012; Settembre et al., 2013; Singh et al., 2009a). Conversely, overexpression of *Atg7* or *Tfeb* by adenovirus reverses hepatic lipid accumulation, reduces liver size, and prevents body weight gain in response to genetic or HFD-induced obesity, as well as improves glucose tolerance and insulin sensitivity (Settembre et al., 2013; Yang et al., 2010). On the other hand, two studies have shown that, contrary to the other studies, liver-specific deletion of *Atg7* leads to reduced hepatic lipid accumulation (Shibata et al., 2009). As the diverging phenotypes come from the same genetic model, the discrepancies are presumably due to differences in experimental conditions or analyses.

Starvation is a powerful stimulus that induces autophagy in the liver that controls hepatic gluconeogenesis. During the early neonatal period, when the placental nutrient supply is cut off at birth, autophagy-deficient (*Atg5*$^{-/-}$) pups die soon after birth from severe hypoglycaemia and hypolipidaemia (Kuma et al., 2004). Dysregulation of autophagy under starvation in adult livers leads to enlarged liver and increased hepatic lipid content (Settembre et al., 2013; Singh et al., 2009b). Additionally, liver-specific deletion of *Atg7*

using inducible Mx1-Cre resulted in hypoglycaemia due to reduced gluconeogenesis (Ezaki et al., 2011).

Positive regulators of starvation-induced autophagy include TFEB and PPARα

For instance, liver-specific deletion of *Tfeb* prevents transcription of a number of autophagy genes and leads to increased hepatic lipid content, increased circulating free fatty acids (FFAs) and impaired FFA oxidation *in vitro* (Settembre et al., 2013). Similarly, PPARα also activates transcription of autophagy components. Pharmacological activation of PPARα induces autophagy in non-starved cells, mimicking a starvation response, whereas the liver from fasted Pparα$^{-/-}$ mice is unable to induce autophagy and exhibits increased lipid content (Lee et al., 2014a). On the other hand, FXR functions as an upstream negative regulator; FXR represses autophagy under a fed state. Pharmacological activation of FXR blunted starvation-induced hepatic autophagy, whereas *Fxr*$^{-/-}$ mice maintained high levels of autophagy in the liver even under a fed state (Lee et al., 2014a; Seok et al., 2014). It would be important to determine whether the same regulation applies to non-starvation induced autophagy in other organs.

Methodologies for detecting mitophagy in adipocytes

Mitophagy structures were initially identified by electron microscopy. A number of studies from the 1950s described double membrane vesicles, later termed autophagic vacuoles, containing recognizable mitochondrial cristae (Eskelinen et al., 2011). Identification and quantification of mitophagy has been challenging due, in large, to a significant overlap with autophagy machinery and an absence of a universally defined

marker for mitophagy per se. Despite the current limitations, there are several tools available for monitoring mitophagy as described below.

Colocalization of mitochondria-localized proteins with GFP-LC3:

Mitophagy can be assessed based on colocalization of the autophagosome with mitochondria. To this end, GFP-LC3 transgenic mice have been successfully used to visualize autophagosomes in vivo and in cultured cells (Klionsky et al., 2012). Vital dyes, such as MitoTracker red are reliable options for labeling mitochondria *in vitro*; however, they possess several limitations for *in vivo* studies. Labeling less than 50% of existing mitochondria and losing signal after fixation preclude using vital dyes *in vivo* (Romanelli et al., 2013). An alternative approach to vital dyes is to label mitochondria using mitochondria-localized proteins and assess their sequestration into the autophagosome using GFP-LC3.

Monitoring mitochondrial turnover: indirect measurement of mitophagy

Mitophagy is a transient event that cannot be fully examined through snapshots of mitochondria using mitochondria-localized proteins. MitoTimer is a fluorescent reporter that able to measure the kinetics of mitochondrial biogenesis and degradation. A mutant of the red fluorescent protein is attached to the mitochondria localization sequence of COX VIII and fluoresces green when the protein is newly synthesized and then gradually transitions to red as the protein matures (Hernandez et al., 2013; Terskikh et al., 2000). This system has been used to assess mitochondrial turnover in the skeletal muscle and the heart (Laker et al., 2014; Stotland and Gottlieb, 2016). Quantifying the loss of red

fluorescence would determine the kinetics of mitophagy process. This method is an indirect assessment of mitophagy and as such, a major concern would be that protein degradation is also measured independent of macroautophagy machinery.

Monitoring delivery of mitochondria to the lysosome:

A more direct way of measuring mitophagy is to assess mitochondria delivery to the lysosome. A tandem mCherry-GFP fusion protein is attached to the mitochondrial localization sequence of the mitochondrial protein FIS1. Different chemical properties of mCherry and GFP allow the identification of mitochondria that is being degraded by the lysosome; GFP gets immediately degraded in the acidic lysosomal environment, whereas mCherry persists (Allen et al., 2013). This system, however, has not yet been adapted for use *in vivo.*

A similar strategy for assessing mitophagy directly has recently been developed using the mt-Keima transgenic mouse system. A tandem repeat of COX VIII tagged with Keima is targeted to the mitochondria. Keima's fluorescence is pH dependent; it emits different colors at neutral or acidic pH, making it possible to determine whether mitochondria are in the cytosol (neutral pH) versus the lysosome (acidic pH). Additionally, Keima fluorescence is derived from corals and is resistant to lysosomal degradation (Katayama et al., 2011; Sun et al., 2015). Having a dual fluorescence allows direct and quantitative assessment of mitophagic flux using FACS, which often is a more sensitive and quantitative tool than imaging analysis (Nezich et al., 2015). These direct tools of assessing mitophagy can be applied to metabolic organs, including adipose tissues.

Chapter 2: Beige adipocyte maintenance is regulated by autophagy-induced mitochondrial clearance

Abstract

Beige adipocytes gained much attention as an alternative cellular target in anti-obesity therapy. While recent studies have identified a number of regulatory circuits that promote beige adipocyte differentiation, the molecular basis of beige adipocyte maintenance remains unknown. Here, we demonstrate that beige adipocytes progressively lose their morphological and molecular characteristics after withdrawing external stimuli, and directly acquire white-like characteristics bypassing an intermediate precursor stage. The beige-to-white adipocyte transition is tightly coupled to a decrease in mitochondria, increase in autophagy, and activation of MiT/TFE transcription factor-mediated lysosome biogenesis. The autophagy pathway is crucial for mitochondrial clearance during the transition; inhibiting autophagy by $UCP1^{+}$-adipocyte-specific deletion of *Atg5* or *Atg12* prevents beige adipocyte loss after withdrawing external stimuli, maintaining high thermogenic capacity and protecting against diet-induced obesity and insulin resistance. The present study uncovers a fundamental mechanism by which autophagy-mediated mitochondrial clearance controls beige adipocyte maintenance, thereby providing new opportunities to prevent obesity.

Introduction

Brown adipose tissue (BAT) contains thermogenic adipocytes that dissipate energy in the form of heat as an evolutionally conserved defense mechanism against hypothermia. Recent works have uncovered that humans and rodents possess two distinct forms of thermogenic adipocytes; namely classical brown adipocytes and beige (or brite) adipocytes. Brown and beige adipocytes are both competent for thermogenesis via the brown/beige-specific protein uncoupled protein 1 (UCP1), and possess similar morphological characteristics, such as multilocular lipid droplets and highly abundant mitochondria (reviewed in Kajimura et al., 2015). Nevertheless, brown and beige adipocytes arise from a distinct developmental origin. For instance, Kozak and colleagues demonstrated that the genetic variability in controlling *Ucp1* expression was observed only in the subcutaneous WAT of mice but not in the interscapular BAT, suggesting that brown and beige adipocytes are under different regulation and may belong to distinct developmental lineages (Guerra et al., 1998; Xue et al., 2007). Furthermore, classical brown adipocytes develop prenatally from a dermomyotome population marked by *Engrailed-1, Myf5,* and *Pax7*, whereas beige adipocytes arise postnatally from progenitor populations in WAT expressing *Ebf2, Pdgfra,* and *Sca1* (Atit et al., 2006; Lee et al., 2012; Sanchez-Gurmaches et al., 2012; Schulz et al., 2011; Seale et al., 2008; Wang et al., 2014).

Of note, adult human BAT depots from the supraclavicular and other regions contain UCP1-positve adipocytes that exhibit molecular signatures resembling murine beige adipocytes (Cypess et al., 2013; Lee et al., 2013a; Lidell et al., 2013; Sharp et al., 2012; Shinoda et al., 2015; Wu et al., 2012), whereas the interscapular BAT of human

infants resemble the murine classical brown adipocytes (Lidell et al., 2013). Importantly, promoting beige adipocyte biogenesis leads to a protection from diet-induced obesity and insulin resistance (Cederberg et al., 2001; Guerra et al., 1998; Seale et al., 2011). In adult human BAT, glucose uptake activity is highly induced after prolonged cold exposure, in parallel with an increase in non-shivering thermogenesis and/or an improvement in insulin sensitivity, even in subjects who had previously lacked detectable BAT depots before chronic cold exposure (Lee et al., 2014b; van der Lans et al., 2013; Yoneshiro et al., 2013). These data all support the potential significance of beige adipocytes in human obesity and diabetes, and illuminate the importance of better understanding the molecular basis of beige adipocyte development and maintenance in order to pioneer future anti-obesity interventions.

An essential characteristic of beige adipocytes is its dynamic regulation of the thermogenic gene program by external stimuli. Beige adipocytes can express high levels of UCP1 in response to chronic cold exposure or ß3-AR agonists, whereas classical brown adipocytes constitutively express high levels of UCP1 (Kajimura et al., 2015). Intriguingly, UCP1 expression in the inguinal WAT became undetectable in mice within 2-3 weeks following transfer from cold environment to ambient or thermoneutral conditions (Gospodarska et al., 2015; Rosenwald et al., 2013). The cold-induced UCP1-positive beige cells became unilocular adipocytes that expressed several white adipocyte-enriched genes when re-acclimated to ambient temperature, some of which re-activate UCP1 expression in response to a subsequent bout of cold exposure (Rosenwald et al., 2013). However, the molecular mechanism of beige adipocyte maintenance remains poorly understood. Here, we demonstrate that beige adipocytes directly acquire a “white-

like" phenotype after withdrawal of ß3-AR agonist bypassing an intermediate precursor stage. We further show that the beige-to-white adipocyte transition is initiated by active mitochondrial clearance via autophagy. Accordingly, inhibition of autophagy by pharmacological or genetic approaches maintains thermogenically functional beige adipocytes for prolonged period of time even after withdrawal of ß3-AR agonist or cold stimulus. Overall, we uncover a fundamental mechanism by which autophagy-mediated mitochondrial turnover controls beige adipocyte maintenance and whole-body energy homeostasis.

Beige adipocytes directly acquire white-like phenotype.

To illuminate the molecular mechanisms by which beige adipocyte maintenance is regulated, we first utilized *Ucp1*$^{Cre/+}$*;Rosa26-GFP* reporter mice and examined morphological and molecular changes of UCP1-positive beige adipocytes *in vivo*. Seven-day-treatment with the ß3-AR agonist CL316,243 profoundly increased the number of GFP-positive beige adipocytes in the inguinal WAT (**Fig. 1A and B**). These adipocytes contained multilocular lipids and co-expressed UCP1. Of note, GFP-positive beige adipocytes were undetected in the inguinal WAT of the reporter mice under thermoneutrality (30˚C), but highly induced in response to the ß3-AR agonist treatment (**Supplementary Fig. 1A**). Additionally, all GFP-positive adipocytes expressed endogenous UCP1 protein immediately following the ß3-AR agonist treatment, further validating the experimental system (**Fig. 1C and Supplementary Fig. 1B**). Notably, 15 to 20 days following ß3-AR agonist withdrawal, GFP-positive adipocytes exhibited near-complete loss of multilocular lipids and endogenous UCP1 expression (**Fig. 1B and C**).

A similar time-dependent decline in UCP1 protein expression was observed in the inguinal WAT depots after mice were acclimated from cold (6˚C) to ambient temperature (**Supplementary Fig. 2**). These results are consistent with previous studies (Gospodarska et al., 2015; Rosenwald et al., 2013). In contrast, classical brown adipocytes in the interscapular BAT retained multilocular lipid droplets and expressed constitutively high levels of UCP1 even 30 days after withdrawing the ß3-AR agonist (**Fig.1D and E**).

We postulate two potential explanations for the above results: 1) beige adipocytes de-differentiate to an intermediate precursor state, and subsequently re-differentiate into unilocular adipocytes, or 2) beige adipocytes directly acquire unilocular adipocyte characteristics without going through an intermediate precursor stage. To distinguish the above two possibilities, we developed a single-cell monitoring system and tracked morphological changes of the individual beige adipocytes *ex vivo* for 10 days following ß3-AR agonist withdrawal (**Supplementary Fig. 3A**). As shown in **Fig. 1F and G**, all of the freshly isolated beige adipocytes contained multilocular lipids and began to change morphology as early as day 3, eventually becoming unilocular adipocytes. By day 10, more than 80% of the GFP-positive beige adipocytes exhibited the unilocular lipid state (Stage III, **Fig. 1G and Supplementary Fig. 3B** for defining adipocyte stages). Importantly, throughout these assays, we did not observe any GFP-positive fibroblast-like cells reminiscent of precursors (**Supplementary Fig. 3C)**. Consistent with the observations *in vivo*, the cultured beige fat progressively lost its thermogenic properties in parallel with these morphological changes (**Supplementary Fig. 3D**). In stark contrast, classical brown adipocytes retained their multilocular lipid morphology up to 10 days

under the same culture conditions, although an increase in lipid size was observed in some adipocytes (**Fig. 1F and H**). These data indicate that the beige adipocyte state is distinctly transient, and that there is a cell-intrinsic difference between beige adipocytes and classical brown adipocytes in maintaining the multilocular lipid state after ß3-AR agonist withdrawal.

Since the unilocular lipid droplet is a morphological characteristic of white adipocytes, we employed global gene expression analyses to address whether the beige adipocyte-derived unilocular adipocytes indeed acquired the molecular characteristics of white adipocytes. To this end, we performed RNA-sequencing analysis of the following cell populations directly isolated from mice. First, we isolated GFP-positive adipocytes from the inguinal WAT of *Ucp1*$^{Cre/+}$*;Rosa26-GFP* reporter mice by FACS, which were subject to RNA-sequencing analyses at 1, 5, 10, 15, and 30 days post ß3-AR agonist withdrawal (**Fig. 2A**). As *bona fide* white adipocytes, we isolated GFP-positive adipocytes from the inguinal WAT of age-matched *Adiponectin* $^{Cre/+}$;*Rosa26-GFP* reporter mice (Eguchi et al., 2011). Lastly, to obtain undifferentiated adipocyte precursors, we sorted Lin$^-$/CD34$^+$/CD29$^+$/Sca1$^+$ cells from the stromal vascular fraction (SVF) of inguinal WAT of age-matched wild-type mice (Rodeheffer et al., 2008). As shown in **Fig. 2B,** mRNA expression of the WAT-enriched genes, such as *Resistin*, *Wfdc21, Spi2, Ednra,* and *Psat1* (Kajimura et al., 2008; Vernochet et al., 2009), were low in beige adipocytes at day 1 and day 5 following withdrawal of ß3-AR agonist, however, began to increase 10 days post ß3-AR agonist withdrawal. At day 30 of withdrawal, the WAT-enriched gene expression reached levels similar to *bona fide* white adipocytes. In parallel to this increase, we observed a concomitant progressive decline in mRNA expression of the

brown/beige-selective thermogenic genes, such as *Ucp1, Cidea*, *Cox8b,* and *Elovl3* (**Fig. 2B**).

Principal Component Analysis (PCA) during the transition phase indicates that the gene expression profiles of the GFP-positive adipocytes at day 30 of withdrawal exhibited a molecular signature resembling white adipocytes. Most importantly, the beige adipocytes at day 5, 10, and 15 of withdrawal progressively acquired the gene signature of white adipocytes, whereas all the beige adipocytes during the transition phase were far remote from the precursors (**Fig. 2C**, precursor cells are shown as purple dots**)**. As an independent approach, hierarchical clustering based on the global gene signatures found that GFP-positive adipocytes at day 30 following ß3-AR agonist withdrawal formed a cluster together with white adipocytes, which was clearly distinct from the beige adipocyte cluster at day 1 (**Fig. 2D)**. The cluster analysis demonstrated that beige adipocytes during the transition phase (day 5, 10, and 15 of withdrawal) were truly distinct from that of preadipocytes. Altogether, our data provide evidence that beige adipocytes directly acquire both the morphological and molecular characteristics resembling white adipocytes after ß3-AR agonist withdrawal, bypassing an intermediate precursor stage.

The beige-to-white adipocyte transition is coupled to mitochondrial clearance.

To understand the mechanism by which beige-to-white adipocyte transition is regulated *in vivo*, we performed the Fuzzy C-Means (FCM) clustering analysis based on the obtained RNA-sequencing dataset and identified 9 distinct gene expression patterns during the beige-to-white adipocyte transition (**Supplementary Fig. 4A**). The most frequently observed expression profile (cluster I) contained 1517 genes that were

expressed highly in beige adipocytes immediately after the chronic treatment with ß3-AR agonist (day 1), and progressively declined during the transition phase (**Fig. 3A**). This cluster contained brown/beige fat-selective mitochondrial genes, including *Cox7a and Cox4i1,* and transcriptional regulators of mitochondrial biogenesis, such as *Pgc1a*, *Nrf1/2* and *Tfam* (**Fig. 3B and Supplementary Table 1**).

The gene-annotation enrichment analysis found that the majority of the cluster I genes were related to mitochondrial components and function including electron transport chain and oxidative phosphorylation (**Fig. 3C and D**). Furthermore, mitochondria in the inguinal WAT depots, as visualized by optical tissue clearing, were abundant immediately after the chronic treatment with ß3-AR agonist, but gradually became undetected at day 15 following ß3-AR agonist withdrawal or thereafter (**Fig. 3E,** upper panel). In contrast, the interscapular BAT depots maintained high amounts of mitochondria even at day 15 or thereafter (**Fig. 3E,** lower). Consistent with this result, protein expression of multiple mitochondrial respiratory chain components in complex I, II and IV, followed the pattern of UCP1 expression in inguinal WAT: highly induced upon chronic treatment with ß3-AR agonist and progressively declined during the transition, reaching basal levels at 15 days post ß3-AR agonist withdrawal (**Fig. 3F**). In contrast, mitochondrial components in interscapular BAT were highly expressed and remained relatively unchanged even after ß3-AR agonist withdrawal (**Fig. 3G)**. This is likely due to active mitochondrial biogenesis, since transcriptional regulators of mitochondrial biogenesis, such as *Pgc1a* and *Tfam*, persist at high levels in the BAT following ß3-AR agonist withdrawal (**Supplementary Fig. 4B**). These data indicate that the beige-to-white adipocyte transition in inguinal WAT is tightly coupled to a progressive decline in mitochondria.

Activation of autophagy during the beige-to-white adipocyte transition.

What is the underlying mechanism of the drastic decline in mitochondria during the beige-to-white adipocyte transition? Mitochondrial content is tightly maintained by the balance between mitochondrial biogenesis and clearance. In fact, transcriptional regulators of mitochondrial biogenesis, including *Pgc1a*, *Nrf1/2* and *Tfam,* were quickly down-regulated in the early phase of beige-to-white adipocyte transition, as shown in Fig. 3B. On the other hand, mitochondrial degradation is mediated by a form of autophagy, termed mitophagy (Kimura et al., 2007). Notably, our RNA-sequencing analysis indicated an up-regulation of numerous core components of the autophagy machinery, including *Atg4b, Atg12, and Atg16* (**Fig. 4A**). In addition, many of the autophagy-related components and lysosomal enzymes, including *Cts* genes, *Arsg*, and *Naga* (Perera et al., 2015), were highly increased during the transition and remained high in unilocular adipocytes. The gene enrichments in the autophagy pathway and the lysosome pathway were highly significant, as Kurtosis (an indicator of peakedness of a distribution) in both pathways was platykurtic (K= -0.03 and -0.24, respectively), whereas that in randomly selected genes exhibited normal distribution (mesokurtic, K= 1.07) (**Fig. 4B**). Importantly, electron microscopic (EM) analyses of beige adipocytes during the transition phase identified a number of autophagic vacuoles containing remnant mitochondrial cristae structures (**Fig. 4C**), morphologically consistent with the induction of mitophagy (Klionsky et al., 2016). Additional morphological observations of mitophagy by EM are shown in **Supplementary Fig. 5A-F**.

Based on these results, we sought to confirm whether autophagy was indeed occurring *in vivo* during the beige-to-white adipocyte transition. To this end, we used *GFP-LC3* mice to assess the levels of punctate LC3, an indicator of autophagosome formation (Mizushima et al., 2004). We observed that these GFP-LC3 puncta were frequently co-localized with mitochondria, consistent with our findings by EM and suggestive of active mitophagy **(Fig. 4D and Supplementary Fig. 5G)**. No GFP signal was found in control mice that did not express GFP-LC3, validating the specificity of the GFP staining (**Supplementary Fig. 5G)**. To examine whether autophagy activity is regulated during the beige-to-white adipocyte transition, we performed the following experiments. First**,** we quantified the number of GFP-LC3 puncta in beige adipocytes during the transition; we observed a significantly lower number of GFP-LC3 puncta in beige adipocytes residing in the inguinal WAT of mice chronically treated with the ß3-AR agonist (day 0), as compared to adipocytes in the inguinal WAT of saline-treated GFP-LC3 mice (**Fig. 4D and E**). The number of GFP-LC3 puncta was significantly increased at 5 days post ß3-AR agonist withdrawal, and remained high 15 days following withdrawal. Second, we employed flow cytometric quantification of GFP-LC3 fluorescence levels to assess autophagic flux, as previously described (Shvets et al., 2008; Warr et al., 2013) (**Supplementary Fig. 6A**). We observed a clear increase in GFP-LC3 levels in day 0 beige adipocytes treated with ß3-AR agonist, as compared to white adipocytes from the saline-treated mice (**Fig. 4F**). After ß3-AR agonist withdrawal, GFP-LC3 levels in beige adipocytes gradually decreased, indicative of increased autophagic flux *in vivo*, eventually reaching the levels seen in white adipocytes from the saline-treated mice (day 5, 15, and 30 in **Fig. 4F**). Lastly, we found that LC3-II was reduced in the beige adipocytes at day 0, which

correlated with increased protein accumulation of the autophagy cargo receptors, NBR1 and p62/SQSTM1 (**Fig. 4G**), both of which are selectively degraded via autophagy (Klionsky et al., 2016). These markers subsequently returned to the basal levels observed in the saline-treated WAT at 30 days after ß3-AR agonist withdrawal (**Fig. 4G**). Notably, LC3-II was reduced upon forskolin treatment (an adenylyl cyclase activator that generates cAMP, the primary second messenger downstream of β-AR) in beige adipocytes in the presence and absence of the lysosomal inhibitor Bafilomycin A1 (BafA1) (**Supplementary Fig. 6B**). These data collectively suggest that autophagy activity is low in beige adipocytes, whereas it is transiently re-activated during the beige-to-white adipocyte transition following ß3-AR agonist withdrawal.

Autophagy in beige adipocytes is regulated by the cAMP-PKA pathway and the MITF transcription factor.

Next, we aimed to identify the upstream regulatory circuits controlling autophagy during the beige-to-white adipocyte transition. DAVID analysis identified a “lysosome” gene ontology signature (P = 7.0 x 10^{-4} after Bonferroni correction) as the top biological pathway that was elevated during the transition phase (**Fig. 5A**). Recent studies have highlighted the importance of transcriptional regulation in autophagosome formation and lysosome biogenesis by the MiT/TFE family of transcription factors (MITF, TFEB, and TFE3) (Perera et al., 2015; Sardiello et al., 2009; Settembre et al., 2011) as well as by other transcriptional regulators, such as FOXK (Bowman et al., 2014), FOXO3 (Warr et al., 2013), FXR/CREB (Lee et al., 2014a; Seok et al., 2014),and ZKSCAN3 (Chauhan et al., 2013). Therefore, we employed the Hypergeometric Optimization of Motif Enrichment

analysis (HOMER) (Heinz et al., 2010) to identify conserved transcription factor binding motifs on the regulatory regions of the autophagy genes that were activated during the beige-to-white adipocyte transition. We found that the most enriched sequence motif from this analysis was the "CLEAR" consensus sequence (GTCACGTGAC) to which the MiT/TFE family of transcription factors (MITF, TFEB, and TEF3) are known to bind (**Fig. 5B**) (Sardiello et al., 2009; Settembre et al., 2011). In a completely independent unbiased analysis from our previous RNA-sequencing dataset (Shinoda et al., 2015), we found that 91.6% (121 out of 132 genes) of the autophagy-related lysosome genes (Perera et al., 2015) were significantly down-regulated in the inguinal WAT by chronic cold exposure for 5 days (**Fig. 5C)**. Importantly, 78.8% of the autophagy-related lysosome genes (104 out of 132 genes) were decreased both by chronic cold exposure and chronic administration of ß3-AR agonist (**Fig. 5D**), indicating that cold exposure and ß3-AR agonist similarly repress lysosome biogenesis *in vivo*. The HOMER-based motif analysis on the cold/ß3-AR agonist-regulated lysosome gene signature similarly identified the CLEAR sequence as the most enriched transcription factor-binding site (not shown).

Of the three MiT/TFE family transcription factors, we found that *Mitf* expression was activated during the initiation of beige-to-white adipocyte transition. In contrast, expression of *Tfeb* and *Tef3* remained unchanged during the transition (**Fig. 5E**). Notably, previous studies (Perera et al., 2015; Sardiello et al., 2009; Settembre et al., 2011) have shown that all the autophagy-related lysosome genes, including *Cts* genes (Cathepsins gene family), and several autophagy components activated during the beige-to-white adipocyte transition (as listed in Fig. 4A) are direct targets of MiT/TFE transcription factors.

We further investigated the extent to which MITF and its downstream autophagy-lysosome signature are regulated by ß-AR signaling in beige adipocytes. Protein kinase A (PKA) is well known to negatively regulate autophagy either by phosphorylation of LC3 or by activating mTORC1 which inhibits autophagy (He and Klionsky, 2009). On the other hand, activation of PKA in response to stimulation of β-AR positively promotes beige adipocyte development through transcriptional activation of the thermogenic gene program and mTORC1 (Collins, 2011; Liu et al., 2016). Thus, we hypothesized that activation of the PKA pathway via β-AR stimulation represses the autophagy network in beige adipocytes, whereas removal of the β-AR agonist leads to autophagy activation during the beige-to-white adipocyte transition. Accordingly, when differentiated beige adipocytes in culture were treated with forskolin (cAMP), *Mitf* expression was significantly decreased (**Fig. 5F)**. Importantly, co-treatment with the PKA inhibitor, H89, largely alleviated both cAMP-mediated repression of *Mitf* levels (**Fig. 5F**) and LC3-II turnover (**Supplementary Fig. 6B**), thereby corroborating a critical role of the PKA pathway for inhibiting autophagy in beige adipocytes. Similarly, *Foxo3* expression was transiently activated during the beige-to-white adipocyte transition and repressed by cAMP through the PKA pathway, although a FOXO-binding motif was much less enriched than the CLEAR binding element (**Supplementary Fig. 7A, B and C**). Importantly, the cAMP-PKA-mediated repression of *Mitf* and *Foxo3* was accompanied by a transcriptional repression of their target genes that encode components of autophagy machinery, such as *Wipi, Bnip, Bnip3l,* and autophagy-related lysosome genes (**Fig. 5G**). Of note, the cAMP pathway was able to repress *Mitf* and autophagy-related lysosome gene expression in beige adipocytes even under starvation conditions, suggesting that the

cAMP-mediated repression on autophagy is independent from nutritional cues (**Fig. 5H and I**). Taken together, these results indicate that autophagy in beige adipocytes is regulated by the cAMP-PKA pathway and the MITF transcription factor.

Autophagy-mediated mitochondrial clearance controls beige adipocyte maintenance.

The results above motivate the hypothesis that autophagy-induced mitochondrial clearance is functionally required for beige adipocyte maintenance. Previous studies showed that genetic deletion of *Atg7* via *Fabp4-Cre* resulted in increased beige adipocyte differentiation *in vivo* (Singh et al., 2009b; Zhang et al., 2009b). However, as *Fabp4-Cre* is active in brown, beige, and white adipocytes as well as some non-adipose tissues including skeletal muscle (Lee et al., 2013b; Mullican et al., 2013), and because *Atg7* deletion in skeletal muscle promotes beige adipocyte differentiation (Kim et al., 2013), the *Fabp4-Cre* model is not suitable to test the specific requirement of autophagy for "maintenance" of beige adipocytes. Thus, we used *Ucp1-Cre* mice (Kong et al., 2014) to generate mature brown/beige adipocyte-specific deletion of *Atg5* or *Atg12*, two core autophagy regulators that are essential for the early steps of autophagosome formation (Mizushima and Komatsu, 2011). Although no *Cre* line currently exists to specifically target mature beige adipocytes without affecting classical brown adipocytes, this model allows us to test the requirement of autophagy for maintenance of newly developed beige adipocytes in response to cold or ß3-AR agonist, given the specific expression of *Ucp1* in mature brown and beige adipocytes.

The ATG12-ATG5 complex was deleted selectively in the BAT but not in the liver, using two systems: *Ucp1*$^{Cre/+}$*;Atg12*$^{flox/flox}$ mice (*Atg12*^{Ucp1} KO), and *Ucp1*$^{Cre/+}$*; Atg5*$^{flox/flox}$ mice (*Atg5*^{Ucp1} KO) (**Fig. 6A**, upper and lower panel, respectively). *Atg5*^{Ucp1} KO*, Atg12*^{Ucp1} KO mice or control mice (*Atg5*$^{flox/flox}$ or *Atg12*$^{flox/flox}$, respectively) were treated with the ß3-AR agonist CL316,243 for seven consecutive days (day 0 of ß3-AR agonist withdrawal), and subsequently rested for 15 days after withdrawing ß3-AR agonist (day 15 of withdrawal) (**Fig. 6B**). We further confirmed that *Atg12* and *Atg5* were significantly reduced in beige adipocytes from *Atg12*^{Ucp1} KO and *Atg5*^{Ucp1} KO mice, respectively (**Supplementary Fig. 8A and B**).

As shown in **Fig. 6C**, beige adipocyte biogenesis was highly induced both in control (*Atg12*$^{flox/flox}$) and *Atg12*^{Ucp1}KO mice at day 0, as assessed by protein expression of UCP1, COX IV, and mitochondrial respiratory chain complexes. Mitochondrial DNA (mtDNA) transcripts and mRNA expression of nuclear-coded beige-enriched genes were significantly increased by chronic ß3-AR agonist treatment both in control (*Atg12*$^{flox/flox}$) and *Atg12*^{Ucp1}KO mice (**Supplementary Fig. 8C**). No difference was found in the basal expression levels of UCP1 and mitochondrial components in inguinal WAT between control and *Atg12*^{Ucp1}KO mice without ß3-AR agonist treatment (*i.e.,* saline treatment). These results indicate that beige adipocyte differentiation *per se* is intact in *Atg12*^{Ucp1}KO mice in response to chronic ß3-AR agonist treatment. However, at 15 days post ß3-AR agonist withdrawal, we observed a striking difference between control (*Atg12*$^{flox/flox}$) and *Atg12*^{Ucp1} KO mice; *i.e.,* the inguinal WAT from the *Atg12*^{Ucp1} KO mice expressed higher levels of UCP1, COX IV, and mitochondrial respiratory chain complexes, as compared to that from control mice (**Fig. 6C**). Importantly, a similar trend in UCP1 and mitochondrial

protein expression was observed in the inguinal WAT from *Atg5*^{Ucp1} KO mice (**Fig. 6D**). Furthermore, mtDNA transcripts, such as *Nd2, Cox2,* and *Cox3*, were significantly higher in the inguinal WAT of *Atg12*^{Ucp1} KO mice at day 15 following ß3-AR agonist withdrawal (**Fig. 6E**, left), whereas no significant differences in the mRNA expression of nuclear coded beige-enriched genes, such as *Pgc1a, Ucp1,* and *Cox7a,* were present between control and *Atg12*^{Ucp1} KO mice (**Fig. 6E**, right). The higher expression of UCP1 and mitochondrial proteins were preferentially found in beige adipocytes, with no major changes observed in classical brown adipocytes residing in interscapular BAT depots; rather, the interscapular BAT of *Atg12*^{Ucp1} KO mice expressed similar levels of UCP1 and mitochondrial proteins as compared to control mice after ß3-AR agonist withdrawal (**Supplementary Fig. 9A**). We also observed comparable, and in certain instances, lower levels of nuclear coded transcripts in the interscapular BAT of *Atg12*^{Ucp1} KO mice as compared to that of control (*Atg12*$^{flox/flox}$) mice at day 0 and day 15 after ß3-AR agonist withdrawal (**Supplementary Fig. 9B and C**). Similarly, no major difference was observed in the expression of UCP1 and mitochondrial contents in the interscapular BAT depots between control (*Atg5*$^{flox/flox}$) and *Atg5*^{Ucp1} KO mice at day 0 and day 15 after ß3-AR agonist withdrawal (**Supplementary Fig. 10A-C**). Since BAT possesses highly active mitochondrial biogenesis even after ß3-AR agonist withdrawal (Supplementary Fig. 4B), mitochondrial biogenesis rather than clearance may play a major role in the maintenance of high amount of mitochondria in BAT.

Next we asked whether *Ucp1*-specific deletion of *Atg12* similarly leads to high levels of mitochondria in the inguinal WAT after re-warming period following cold exposure (**Supplementary 11A**). Consistent with the findings after β3-AR agonist

withdrawal, we found that the inguinal WAT from the *Atg12*^{Ucp1} KO mice expressed higher levels of UCP1 and mitochondrial respiratory chain complexes, as compared to that from control (*Atg12*$^{flox/flox}$) mice at 15 days after re-warming (**Supplementary Fig. 11B**). We further asked whether pharmacological inhibition of autophagy is able to retain high levels of UCP1 and mitochondrial contents**.** To this end, we treated mice with chloroquine (CQ) at a dose of 60 mg kg^{-1} or saline for 15 consecutive days during the re-warming period following cold exposure (**Supplementary Fig. 11C**). We found that pharmacological inhibition of autophagy led to a significant retention of higher UCP1 levels and mitochondrial proteins in the inguinal WAT after re-warming (**Supplementary Fig. 11D**). Moreover, chloroquine treatment following ß3-AR agonist withdrawal significantly induced LC3 accumulation in beige adipocytes (**Supplementary Fig. 11E and F**) and maintained higher levels of UCP1 and mitochondrial proteins in the inguinal WAT after ß3-AR agonist withdrawal (**Supplementary Fig. 11G**). These data indicate that autophagy-mediated mitochondrial clearance via *Atg5* and *Atg12* is required for efficient beige-to-white adipocyte transition.

The distinct effects of autophagy deletion on beige adipocyte maintenance motivated the intriguing hypothesis that *Atg12*^{Ucp1} KO mice would exhibit higher thermogenic capacity after the removal of external cues. To test this hypothesis, we first measured oxygen consumption rate (OCR) of the inguinal WAT from control (*Atg12*$^{flox/flox}$) and *Atg12*^{Ucp1} KO mice at 15 days post ß3-AR agonist withdrawal. As shown in **Fig. 6F**, OCR was significantly higher in the inguinal WAT of *Atg12*^{Ucp1} KO mice than control mice when the tissues were treated with isoproterenol. In contrast, no significant difference was observed without isoproterenol treatment (at basal state). This cAMP-dependent

increase in thermogenesis is consistent with a previous report that UCP1-mediated proton uncoupling requires direct binding of long-chain free fatty acid to UCP1 protein in response to cAMP-stimulated lipolysis (Fedorenko et al., 2012). Thus, the beige adipocytes that persisted in *Atg12*^{Ucp1} KO were thermogenically active in response to cAMP stimulation. In contrast, no significant difference in OCR was found in the interscapular BAT between control (*Atg12*$^{flox/flox}$) and *Atg12*^{Ucp1} KO mice (**Supplementary Fig. 9C)**.

To examine the metabolic significance of retaining thermogenic beige adipocytes *in vivo*, we measured whole-body energy expenditure (VO_2) of control (*Atg12*$^{flox/flox}$) and *Atg12*^{Ucp1} KO mice during 17 to 18 days post ß3-AR agonist withdrawal. As shown in **Fig 6G**, *Atg12*^{Ucp1} KO mice exhibited significantly higher VO_2 levels compared to control mice during the night phase. The data were statistically significant regardless of body weight normalization (**Supplementary Fig. 12A**). On the other hand, no significant difference was found in locomotor activity and food intake between control and *Atg12*^{Ucp1} KO mice (**Supplementary Fig. 12B**).

Prolonged maintenance of beige adipocytes prevents diet-induced obesity and insulin resistance.

Obesity is known to impair beige adipocyte biogenesis, partly through activation of TGFß and Notch signals in WAT (Bi et al., 2014; Yadav et al., 2011). Here, we determined the extent to which obesity also affects the kinetics of beige-to-white adipocyte transition. To this end, we examined the morphological change of beige adipocytes in the inguinal WAT using *Ucp1-Cre; mT/mG* reporter mice under a regular diet (body weight, 29.5 $\pm$ 1.4

g) and age-matched obese mice under a high-fat diet (body weight, 49.8 ± 0.8 g). We found that beige adipocytes (*i.e.,* UCP1+/GFP+ multilocular adipocytes) in the inguinal WAT of obese mice acquired a "white-like" state (*i.e.,* unilocular lipids and loss of UCP1 expression) at a faster rate than age-matched lean mice (**Fig. 7A and B**). On the other hand, no major change was found in the morphology of UCP1+ brown adipocytes between obese and lean mice (**Supplementary Fig. 13**). This observation is intriguing because recent studies indicate that autophagy is altered in the adipose tissues of obese and type 2 diabetes patients (Jansen et al., 2012; Kosacka et al., 2015; Kovsan et al., 2011; Nuñez et al., 2013; Ost et al., 2010). For instance, obesity-induced insulin resistance and type 2 diabetes impair mTOR signaling, thereby leading to autophagy activation in human adipose tissues (Kosacka et al., 2015; Ost et al., 2010). These results indicate that obesity not only impairs beige adipocyte differentiation but also accelerates the beige-to-white adipocyte transition, at least in part, through the activation of autophagy-lysosome biogenesis.

The above results motivated us to ask whether the persistence of thermogenic beige adipocytes in *Atg12*^{Ucp1} KO mice impacts weight gain in response to an obesogenic diet. Based on the previous observation that *Ucp1* deletion induces obesity specifically under conditions of thermoneutrality (Feldmann et al., 2009), individually-housed wild-type and *Atg12*^{Ucp1} KO mice were chronically treated with the ß3-AR agonist CL316,243 for seven consecutive days to induce beige adipocyte development, and the mice were subsequently fed a high-fat diet for 8 weeks under thermoneutrality (**Fig. 7C**). While there was no significant difference in body weight between control (*Atg12*$^{flox/flox}$) and *Atg12*^{Ucp1} KO mice immediately after ß3-AR agonist treatment (day 0), *Atg12*^{Ucp1} KO

mice gained significantly less body weight than wild-type mice after acclimation to thermoneutrality (**Fig. 7D**). The difference in body weight between control and *Atg12*^{Ucp1} KO was due to a significantly reduced adipose mass, but not due to changes in lean mass (**Fig. 7E**). Consistent with this result, white adipose tissue mass (inguinal WAT and epididymal WAT) in *Atg12*^{Ucp1} KO was lower than control (**Fig.7F**). Liver mass was slightly but significantly lower in *Atg12*^{Ucp1} KO mice, likely due to reduced hepatic triglyceride (TG) contents in *Atg12*^{Ucp1} KO mice (**Fig.7G**). Importantly, after 8 weeks of high-fat diet feeding, *Atg12*^{Ucp1} KO mice exhibited significantly improved systemic glucose homeostasis compared to control mice, as assessed by glucose-tolerance test (**Fig. 7H**) and insulin-tolerance test (**Fig. 7I**). In contrast, such metabolic phenotypes were not observed in the absence of ß3-AR agonist treatment (**Supplementary Fig. 14**). Thus the metabolic phenotypes, *i.e.,* reduced body-weight gain and improved glucose homeostasis, found in *Atg12*^{Ucp1} KO mice after ß3-AR agonist treatment are largely due to retention of thermogenically active beige adipocytes that are recruited by chronic ß3-AR agonist treatment. These observations are consistent with the above finding that *Atg12*^{Ucp1} KO mice maintain higher amounts of UCP1 and other mitochondrial proteins in the inguinal WAT for prolonged periods compared to autophagy-competent controls, specifically following withdrawal of ß3-AR agonist. Altogether, these data indicate that prolonged maintenance of thermogenically active beige fat is sufficient to increase whole-body energy expenditure and protect mice from diet-induced obesity and insulin resistance.

Discussion

In the present study, we demonstrate that autophagy-induced mitochondrial turnover is crucial for beige adipocyte maintenance and energy expenditure *in vivo*. Accumulating evidence shows that beige adipocyte biogenesis is induced by a variety of external stimuli, such as chronic cold exposure, exercise, long-term treatment of PPARγ agonists, cancer cachexia, and environmental enrichment (Kajimura et al., 2015). The induced beige adipocytes appear to arise from *de novo* differentiation of beige precursors (Wang et al., 2013) or direct conversion from mature white adipocytes (Barbatelli et al., 2010; Himms-Hagen et al., 2000; Lee et al., 2015). Regardless of cellular origin, the newly recruited beige adipocytes gradually lose their morphological and molecular characteristics upon removal of external cues (Gospodarska et al., 2015; Rosenwald et al., 2013). Given the nature of lineage-tracing experiments, however, the prior studies were not able to determine whether this transition is mediated through de-differentiation of beige adipocytes to an intermediate precursor state and subsequent re-differentiation into white adipocytes, or through a direct conversion. Moreover, the inducible *Cre-ER* system used for the previous work may have certain technical limitations for lineage tracing; a recent study showed that newly recruited beige adipocytes during the chase phase (*i.e.,* after tamoxifen withdrawal) may be unintentionally labeled because the hydrophobic properties of tamoxifen make it difficult to “wash-out” in adipose tissues (Ye et al., 2015). Our data provide direct evidence that beige adipocytes possess cell-intrinsic capacity to acquire a white-like state bypassing an intermediate precursor stage. Future analysis of chromatin reorganization and epigenetic regulation during this transition will

additionally uncover the fundamental mechanisms by which environmental cues control maintenance of adipose cell fate.

While recent studies reported a variety of external and internal cues that promote beige adipocyte differentiation, the molecular mechanism of beige adipocyte "maintenance" remains unknown. Genetic knockout of ATG7, the E1-like enzyme required for autophagosome formation, results in increased beige adipocytes in WAT, indicating a role of autophagy in beige adipocyte differentiation (Singh et al., 2009b; Zhang et al., 2009b). However, these studies used *Fabp4-Cre* system, leading to knockout of ATG7 in all types of adipocytes (*i.e.,* brown, beige, and white adipocytes) and non-adipose tissues such as skeletal muscle and brain (Lee et al., 2013b; Mullican et al., 2013). Thus it remains unclear whether autophagy is involved in the specific differentiation of beige adipocyte from precursors, or maintenance of mature beige adipocytes. In addition, because ATG7 controls p53-dependent transcription and cell cycle progression independently of its E1-like enzymatic activity, it is difficult to ascertain a general role for autophagy in those previous studies (Lee, 2012). Thus, we selectively deleted either *Atg5* or *Atg12* in differentiated beige/brown adipocytes using *Ucp1-Cre* in order to test the specific requirement of autophagy for beige adipocyte maintenance *per se*. While ATG5 and ATG12 each possess unique functions in other cell types (Kimmey et al., 2015; Malhotra et al., 2015), we demonstrate that genetic deletion of *Atg5* or *Atg12* in beige adipocytes exhibit highly concordant phenotypes, most notably, the substantial retention of UCP1 and mitochondrial proteins in the subcutaneous WAT after withdrawing ß3-AR agonist (**Fig. 6**). These results strongly argue against any individual effects exerted by these ATGs. In further support, pharmacological autophagy inhibition with the anti-

malarial chloroquine also retains high levels of UCP1 and mitochondrial proteins after re-warming following cold exposure as well as after ß3-AR agonist withdrawal. Taken together, these results, obtained using genetic and pharmacological approaches, corroborate a critical requirement for the autophagy pathway in clearance of beige adipocyte mitochondria during the beige-to-white transition *in vivo*, thereby intimating a specific role of mitophagy in beige adipocyte maintenance.

Recent studies reported that adult human BAT from supraclavicular regions displays molecular signatures that resemble beige adipocytes(Cypess et al., 2013; Lee et al., 2013a; Lidell et al., 2013; Sharp et al., 2012; Shinoda et al., 2015; Wu et al., 2012) and that chronic cold acclimation increases glucose uptake in the BAT of adult humans who do not possess detectable BAT before cold treatment (Lee et al., 2014b; van der Lans et al., 2013; Yoneshiro et al., 2013). These studies indicate that adult humans possess beige-like “recruitable” thermogenic adipocytes. Notably, the prevalence of human BAT is inversely correlated with BMI and adiposity (Cypess et al., 2009; Saito et al., 2009; van Marken Lichtenbelt et al., 2009), whereas autophagy is up-regulated in adipose tissue of obese subjects, exhibiting a positive correlation with the degree of obesity and visceral fat distribution (Jansen et al., 2012; Kosacka et al., 2015; Kovsan et al., 2011; Nuñez et al., 2013; Ost et al., 2010). Our studies in rodents also indicate that obesity accelerates the beige-to-white adipocyte transition. It is possible that the altered kinetics of the transition under obesity is due partly to the activation of autophagy-related lysosome biogenesis; thus, autophagy/lysosome inhibition can be an effective approach to retain high thermogenically active beige adipocytes for prolonged period of time.

It has been appreciated that classical brown adipocytes in the interscapular BAT can acquire a “white-like” unilocular morphology in morbidly obese mice, such as *ob/ob* mice, or in aged mice (Cinti, 1999; Sellayah and Sikder, 2014). Our experiments, on the other hand, were performed in young mice under a relatively short-term high fat diet (4-8 weeks) in which mitochondrial biogenesis remains active in the BAT. It is possible that mitochondrial biogenesis rather than mitochondrial clearance largely contributes to the maintenance of high mitochondrial contents in BAT, whereas mitochondrial clearance plays a critical role in the mitochondrial homeostasis of beige fat when external cues are withdrawn. Our data, however, do not exclude the possibility that autophagy-mediated mitochondrial clearance also play a role in the maintenance of classical brown adipocytes under a morbidly obese state or in aged mice.

In summary, the present study identified autophagy-mediated mitochondrial clearance as a previously unappreciated mechanism that controls beige adipocyte maintenance and whole-body energy homeostasis. This may offer a new therapeutic opportunity to combat obesity and insulin resistance through prolonged maintenance of thermogenic beige adipocytes.

Figure 1

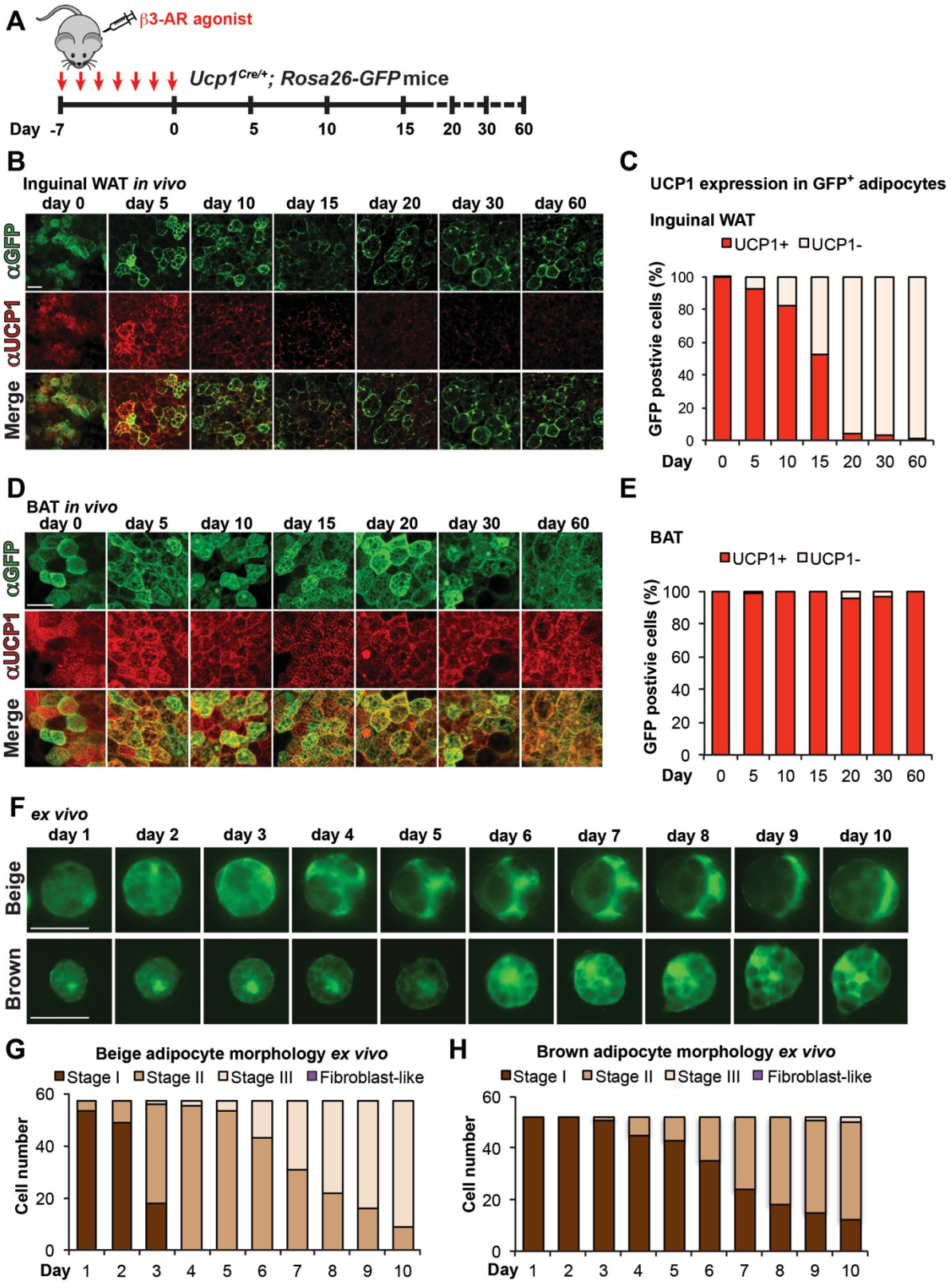
A
β3-AR agonist
Ucp1Cre/+; Rosa26-GFP mice
Day -7 0 5 10 15 20 30 60
B
Inguinal WAT in vivo
day 0 day 5 day 10 day 15 day 20 day 30 day 60
αGFP
αUCP1
Merge
C
UCP1 expression in GFP+ adipocytes
Inguinal WAT
UCP1+ UCP1-
GFP postivie cells (%)
100 80 60 40 20 0
Day 0 5 10 15 20 30 60
D
BAT in vivo
day 0 day 5 day 10 day 15 day 20 day 30 day 60
αGFP
αUCP1
Merge
E
BAT
UCP1+ UCP1-
GFP postivie cells (%)
100 80 60 40 20 0
Day 0 5 10 15 20 30 60
F
ex vivo
day 1 day 2 day 3 day 4 day 5 day 6 day 7 day 8 day 9 day 10
Beige
Brown
G
Beige adipocyte morphology ex vivo
Stage I Stage II Stage III Fibroblast-like
Cell number
60 40 20 0
Day 1 2 3 4 5 6 7 8 9 10
H
Brown adipocyte morphology ex vivo
Stage I Stage II Stage III Fibroblast-like
Cell number
60 40 20 0
Day 1 2 3 4 5 6 7 8 9 10

Figure 1. Beige adipocytes directly acquire morphological characteristics of white adipocytes after withdrawing external stimuli. (A) Schematic illustration of experiments to track beige adipocytes *in vivo*. *Ucp1*$^{Cre/+}$*;Rosa26-GFP* reporter mice were treated with the ß3-AR agonist CL316,243 at 1mg kg^{-1} for seven consecutive days. Interscapular BAT and inguinal WAT depots were harvested for morphological and molecular analyses at the indicated time points after ß3-AR agonist withdrawal. **(B)** Immunohistochemistry for GFP and endogenous UCP1 expression in the inguinal WAT from *Ucp1*$^{Cre/+}$*;Rosa26-GFP* reporter mice. Inguinal WAT depots were harvested at indicated time points after ß3-AR agonist withdrawal. Scale bar, 70 μm. **(C)** Quantification of GFP-positive adipocytes that express endogenous UCP1 in (B). n = 150 cells or more per group. **(D)** Immunohistochemistry for GFP and endogenous UCP1 expression in the interscapular BAT from *Ucp1*$^{Cre/+}$*; Rosa26-GFP* reporter mice. BAT depots were harvested at indicated time points after ß3-AR agonist withdrawal. Scale bar, 40 μm. **(E)** Quantification of GFP-positive adipocytes that express endogenous UCP1 in (D). n = 127 cells or more per group. **(F)** Morphological changes of beige adipocytes (top panel) and classical brown adipocytes (bottom panel) using the single-cell monitoring system. GFP-positive beige or brown adipocytes were isolated from *Ucp1*$^{Cre/+}$*;Rosa26-GFP* reporter mice treated with the ß3-AR agonist CL316,243 at 1mg kg^{-1} for seven days. Morphology of the individual GFP-positive adipocytes was monitored for 10 consecutive days. Scale bar, 70 μm. (**G**) Quantification of GFP-positive beige adipocytes in (F, top panel). Stage of each cell was estimated based on the criteria shown in Supplementary Figure 3B and C. *n* = 57 cells. (**H**) Quantification of GFP-positive classical brown

adipocytes in (F, bottom panel). Stage of each cell was estimated based on the criteria shown in Supplementary Figure 3B and C. *n* = 55 cells.

Figure 2

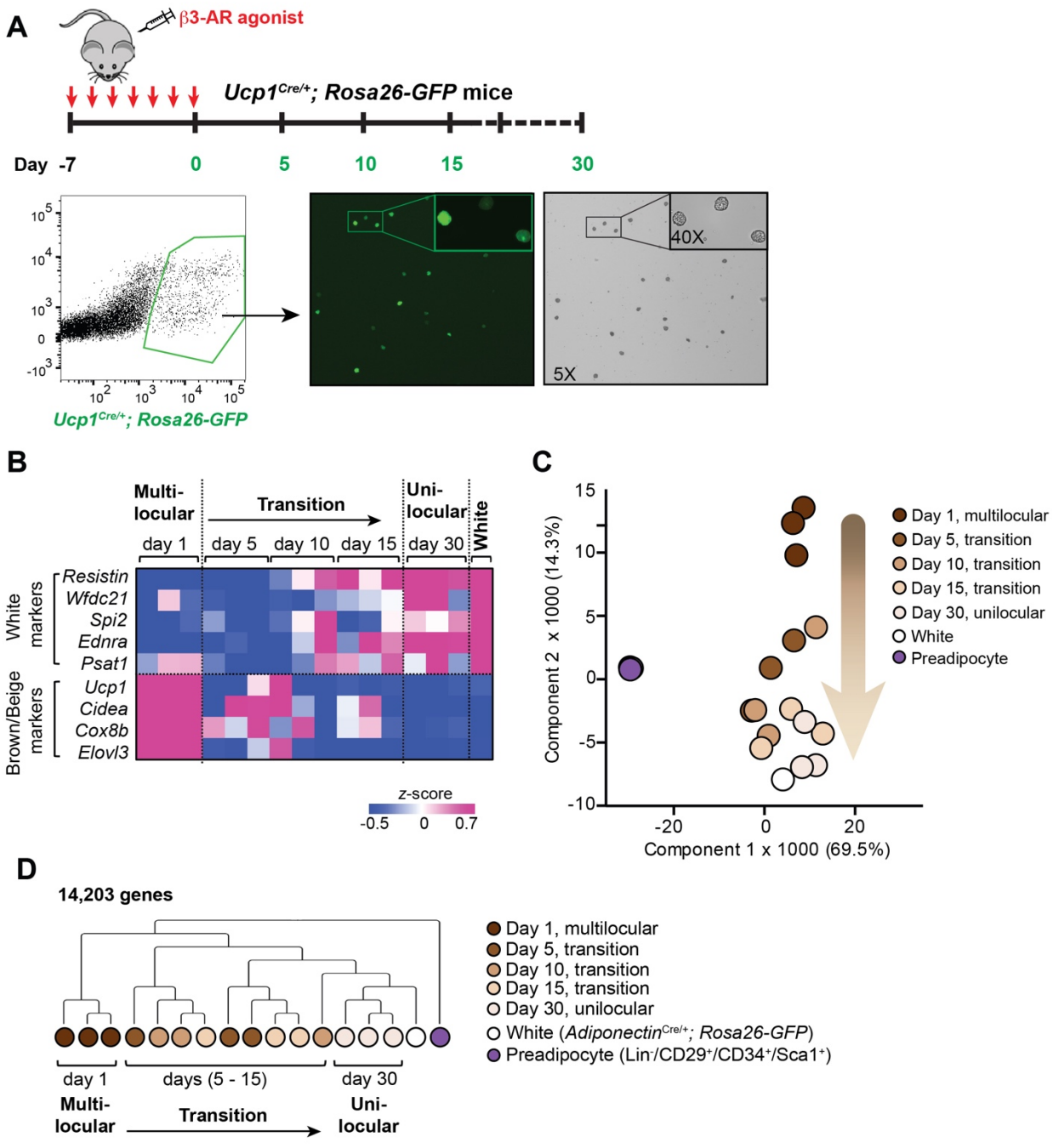
A
β3-AR agonist
Ucp1Cre/+; Rosa26-GFP mice
Day -7
0
5
10
15
30
40X
5X
Ucp1Cre/+; Rosa26-GFP
B
Multi-locular
Transition
Uni-locular
White
day 1
day 5
day 10
day 15
day 30
White markers
Resistin
Wfdc21
Spi2
Ednra
Psat1
Brown/Beige markers
Ucp1
Cidea
Cox8b
Elovl3
z-score
-0.5
0
0.7
C
Component 2 x 1000 (14.3%)
Component 1 x 1000 (69.5%)
Day 1, multilocular
Day 5, transition
Day 10, transition
Day 15, transition
Day 30, unilocular
White
Preadipocyte
D
14,203 genes
day 1
days (5 - 15)
day 30
Multi-locular
Transition
Uni-locular
Day 1, multilocular
Day 5, transition
Day 10, transition
Day 15, transition
Day 30, unilocular
White (AdiponectinCre/+; Rosa26-GFP)
Preadipocyte (Lin-/CD29+/CD34+/Sca1+)

Figure 2. Beige adipocytes directly acquire molecular characteristics of white adipocytes after withdrawing external stimuli. (**A**) Top panel: Schematic illustration for isolating GFP-positive adipocytes by FACS at the indicated time points in the inguinal WAT of *Ucp1*$^{Cre/+}$*;Rosa26-GFP* reporter mice. Bottom panel: Gating strategy for isolating GFP-positive adipocytes. GFP positive adipocytes were visualized after sorting at day 1 of ß3-AR agonist withdrawal. Note that all the FACS-isolated cells (bright-field) express GFP and that all of the GFP positive cells from day 1 of ß3-AR agonist withdrawal contained multilocular lipids. (**B**) Expression profiles of the WAT-enriched genes and brown/beige fat-enriched genes in the GFP-positive FACS-isolated beige adipocytes at indicated time points after ß3-AR agonist withdrawal as described in (A). The color scale shows z-scored FPKM representing the mRNA level of each gene in blue (low expression)-white-red (high expression) scheme. Gene expression in the white adipocytes FACS-isolated from the inguinal fat pad of age-matched *Adiponectin*$^{Cre/+}$;*Rosa26-GFP* reporter mice is shown in the right column. (**C**) Principal component analysis (PCA) of transcriptome in FACS-isolated beige adipocytes (*Ucp1*$^{Cre/+}$*;Rosa26-GFP)*, FACS-isolated white adipocytes (*Adiponectin*$^{Cre/+}$;*Rosa26-GFP),* and undifferentiated adipocyte precursors (Lin^{-}/CD34^{+}/CD29^{+}/Sca1^{+}) from the SV fraction of inguinal WAT of age-matched wild-type mice. The number in parentheses represents the proportion of data variance explained by each PC. (**D**) Hierarchical clustering of beige adipocytes, white adipocytes, and undifferentiated adipocyte precursors. The clustering was generated based on the RNA-sequencing data of GFP-positive beige adipocytes at day 1 of ß3-AR agonist withdrawal (multi-locular state), at days 5, 10, and 15 of withdrawal (transition phase), and at day 30 of withdrawal (unilocular

state). White adipocytes and undifferentiated precursors are shown in white and purple circles, respectively. The clustering was visualized by MeV. The horizontal distance represents similarities among each cluster.

Figure 3

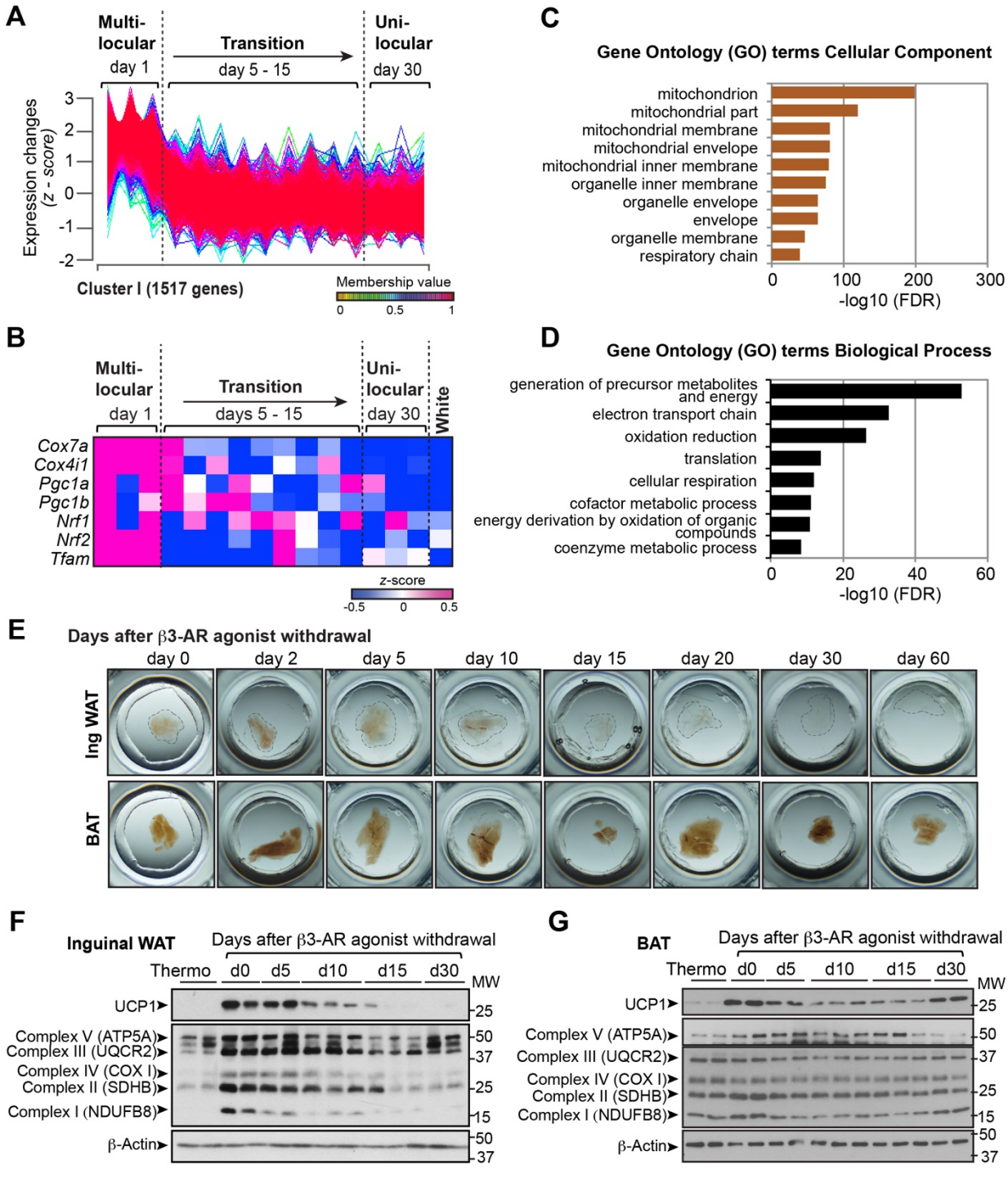
A
Multi-locular
day 1
Transition
day 5 - 15
Uni-locular
day 30
Expression changes (z - score)
Cluster I (1517 genes)
Membership value
B
Multi-locular
day 1
Transition
days 5 - 15
Uni-locular
day 30
White
Cox7a
Cox4i1
Pgc1a
Pgc1b
Nrf1
Nrf2
Tfam
z-score
C
Gene Ontology (GO) terms Cellular Component
mitochondrion
mitochondrial part
mitochondrial membrane
mitochondrial envelope
mitochondrial inner membrane
organelle inner membrane
organelle envelope
envelope
organelle membrane
respiratory chain
-log10 (FDR)
D
Gene Ontology (GO) terms Biological Process
generation of precursor metabolites and energy
electron transport chain
oxidation reduction
translation
cellular respiration
cofactor metabolic process
energy derivation by oxidation of organic compounds
coenzyme metabolic process
-log10 (FDR)
E
Days after β3-AR agonist withdrawal
day 0
day 2
day 5
day 10
day 15
day 20
day 30
day 60
Ing WAT
BAT
F
Inguinal WAT
Days after β3-AR agonist withdrawal
Thermo
d0
d5
d10
d15
d30
MW
UCP1
Complex V (ATP5A)
Complex III (UQCR2)
Complex IV (COX I)
Complex II (SDHB)
Complex I (NDUFB8)
β-Actin
G
BAT
Days after β3-AR agonist withdrawal
Thermo
d0
d5
d10
d15
d30
MW
UCP1
Complex V (ATP5A)
Complex III (UQCR2)
Complex IV (COX I)
Complex II (SDHB)
Complex I (NDUFB8)
β-Actin

Figure 3. Beige-to-white adipocyte transition is accompanied by mitochondrial clearance. (**A**) Gene expression profile of 1,517 genes that belongs to Cluster I during the beige-to-white adipocyte transition. Y-axis represents expression changes in the expression level (*z*-scored FPKM) of each gene. Gene expression profiles of other clusters are shown in Supplementary Fig. 4A. (**B**) Expression profiles of brown/beige-enriched mitochondrial genes (*Cox7a* and *Cox4i1*) and mitochondrial biogenesis genes (*Pgc1a, Pgc1b, Nrf1/2,* and *Tfam*) in the GFP-positive adipocytes at indicated time points after ß3-AR agonist withdrawal. The color scale shows z-scored FPKM representing the mRNA level of each gene in blue (low expression)-white-red (high expression) scheme. Gene expression in the white adipocytes isolated from *Adiponectin*$^{Cre/+}$;*Rosa26-GFP* reporter mice is shown in the right column. *n* = 3 for each time point of beige-to-white transition. (**C**) GO analysis (cellular component) of the genes in Cluster I (GO FAT). (**D**) GO analysis (biological process) of the genes in Cluster I (GO FAT). (**E**) Inguinal WAT and BAT depots (3-5mm diameter) at indicated time points after ß3-AR agonist withdrawal were fixed in 4% PFA and cleared for optical imaging. (**F**) Immunoblotting for UCP1 and the indicate mitochondrial complex components in the inguinal WAT depots of wild-type mice under thermoneutrality and at indicated time points (days 0 - 30) following ß3-AR agonist withdrawal. ß-actin was used as a loading control. Molecular weight (MW) is shown on the right. (**G**) Immunoblotting for UCP1 and the indicate mitochondrial complex components in the interscapular BAT depots of wild-type mice in (F). ß-actin was used as a loading control. Molecular weight (MW) is shown on the right.

Figure 4

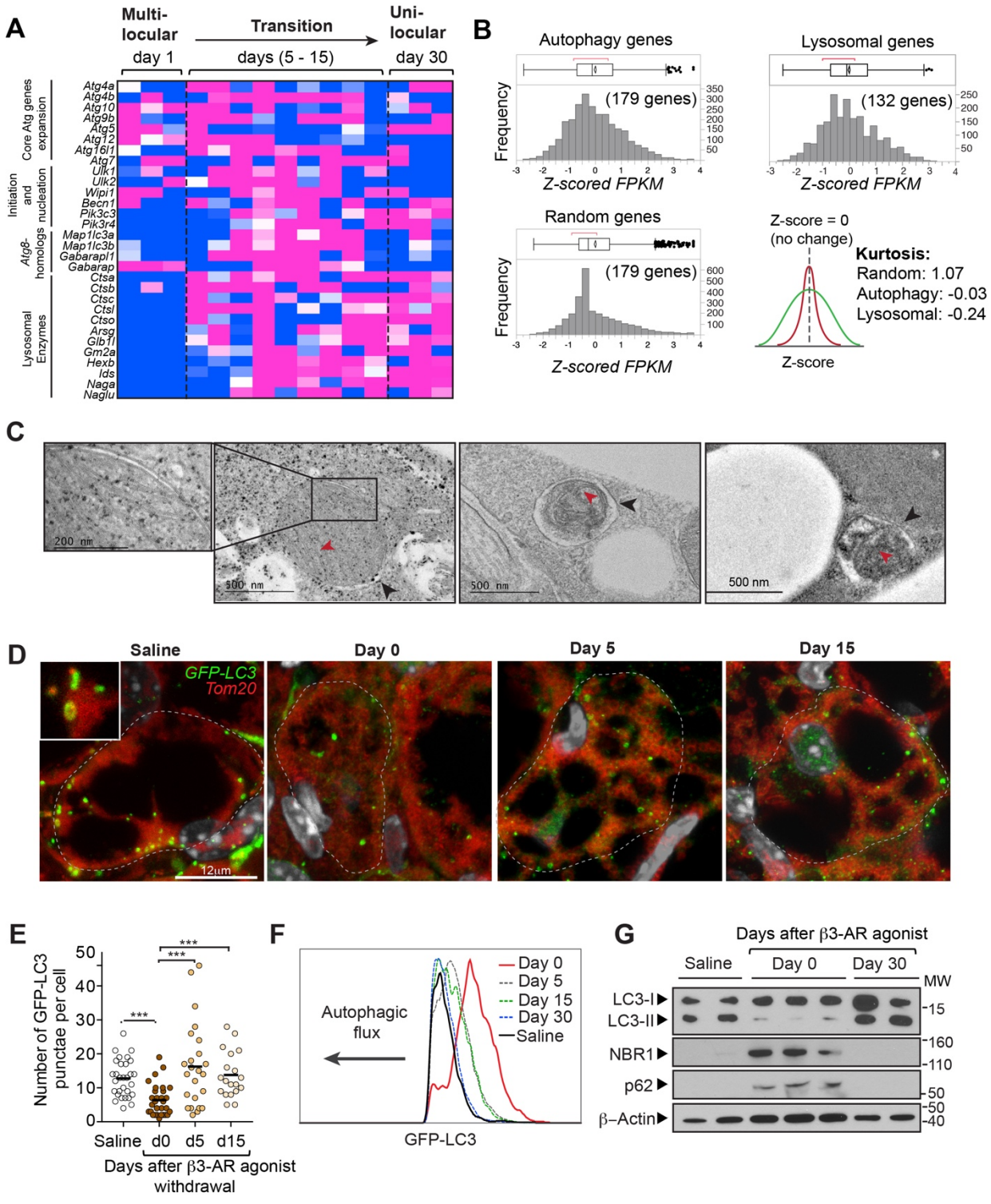
A
Multi-locular
Transition
Uni-locular
day 1
days (5 - 15)
day 30
Core Atg genes expansion
Initiation and nucleation
Atg8-homologs
Lysosomal Enzymes
Atg4a
Atg4b
Atg10
Atg9b
Atg5
Atg12
Atg16l1
Atg7
Ulk1
Ulk2
Wipi1
Becn1
Pik3c3
Pik3r4
Map1lc3a
Map1lc3b
Gabarapl1
Gabarap
Ctsa
Ctsb
Ctsc
Ctsl
Ctso
Arsg
Glb1l
Gm2a
Hexb
Ids
Naga
Naglu
B
Autophagy genes
(179 genes)
Frequency
Z-scored FPKM
Lysosomal genes
(132 genes)
Z-scored FPKM
Random genes
(179 genes)
Frequency
Z-scored FPKM
Z-score = 0
(no change)
Z-score
Kurtosis:
Random: 1.07
Autophagy: -0.03
Lysosomal: -0.24
C
200 nm
500 nm
500 nm
500 nm
D
Saline
Day 0
Day 5
Day 15
GFP-LC3
Tom20
12μm
E
Number of GFP-LC3 punctae per cell
***
***
***
Saline
d0
d5
d15
Days after β3-AR agonist withdrawal
F
Autophagic flux
Day 0
Day 5
Day 15
Day 30
Saline
GFP-LC3
G
Days after β3-AR agonist
Saline
Day 0
Day 30
MW
LC3-I
LC3-II
NBR1
p62
β–Actin
15
160
110
50
50
40

Figure 4. Activation of autophagy during the beige-to-white adipocyte transition.

(**A**) Expression profile of the autophagy-related genes during the beige-to-white adipocyte transition. The color scale shows z-scored FPKM representing the mRNA level of each gene in blue (low expression)-white-red (high expression) scheme. *n* = 3 for each time point. (**B**) Kurtosis of the autophagy-related genes and lysosomal enzymes in (A). Note that the autophagy and lysosome component genes were platykurtic (*K*= -0.03 and -0.24, respectively), while randomly selected genes showed mesokurtic distribution (*i.e,* normal distribution, *K*= 1.07). (**C**) Electron microscopy images of beige adipocytes during the transition (days 5 – 30 following ß3-AR agonist withdrawal). Black arrowheads indicate the autophagic vesicles containing mitochondrial remnants, as identified by remaining cristae (red arrowheads). Scale bar, 500 nm. (**D**) Confocal microscopy images of beige adipocytes from *GFP-LC3* mice. *GFP-LC3* mice were treated with saline or the ß3-AR agonist CL316,243 at 1mg kg^{-1} for seven consecutive days. The inguinal WAT depots were harvested at indicated time points (days 0 – 15) following ß3-AR agonist withdrawal. Mitochondria and GFP-LC3-labelled autophagosomes were visualized by immunohistochemistry for Tom20 (red) and GFP (green), respectively. Nuclei are labeled with Hoechst (grey). The image in inset shows co-localization of GFP-LC3 and mitochondria. Scale bar, 12 μm. (**E**) Quantification of the GFP-LC3 puncta in (A) at indicated time points. *** P <0.001 by Mann-Whitney U test. *n* = 20-30 cells per condition. (**F**) Autophagic flux in adipocytes from *GFP-LC3* mice at indicated time points (days 0 – 30) following ß3-AR agonist withdrawal (beige adipocytes) and from *GFP-LC3* mice treated with saline (white adipocytes). X-axis represents GFP-LC3 fluorescence intensity and Y-axis represents the number of adipocytes normalized to mode. Note that

decreased GFP-LC3 is associated with increased autophagic flux (Shvets et al., 2008; Warr et al., 2013). Data are representatives of two independent experiments. (**G**) Immunoblotting for NBR1, p62/SQSTM1, and LC3 (LC3-I and LC3-II) from lysates of adipocytes isolated from the inguinal WAT of wild-type mice treated with saline or the ß3-AR agonist CL316,243 (day 0 and 30 following ß3-AR agonist withdrawal). ß-actin was used as a loading control. Data are representatives of 3 independent experiments. Molecular weight (MW) is shown on the right.

Figure 5

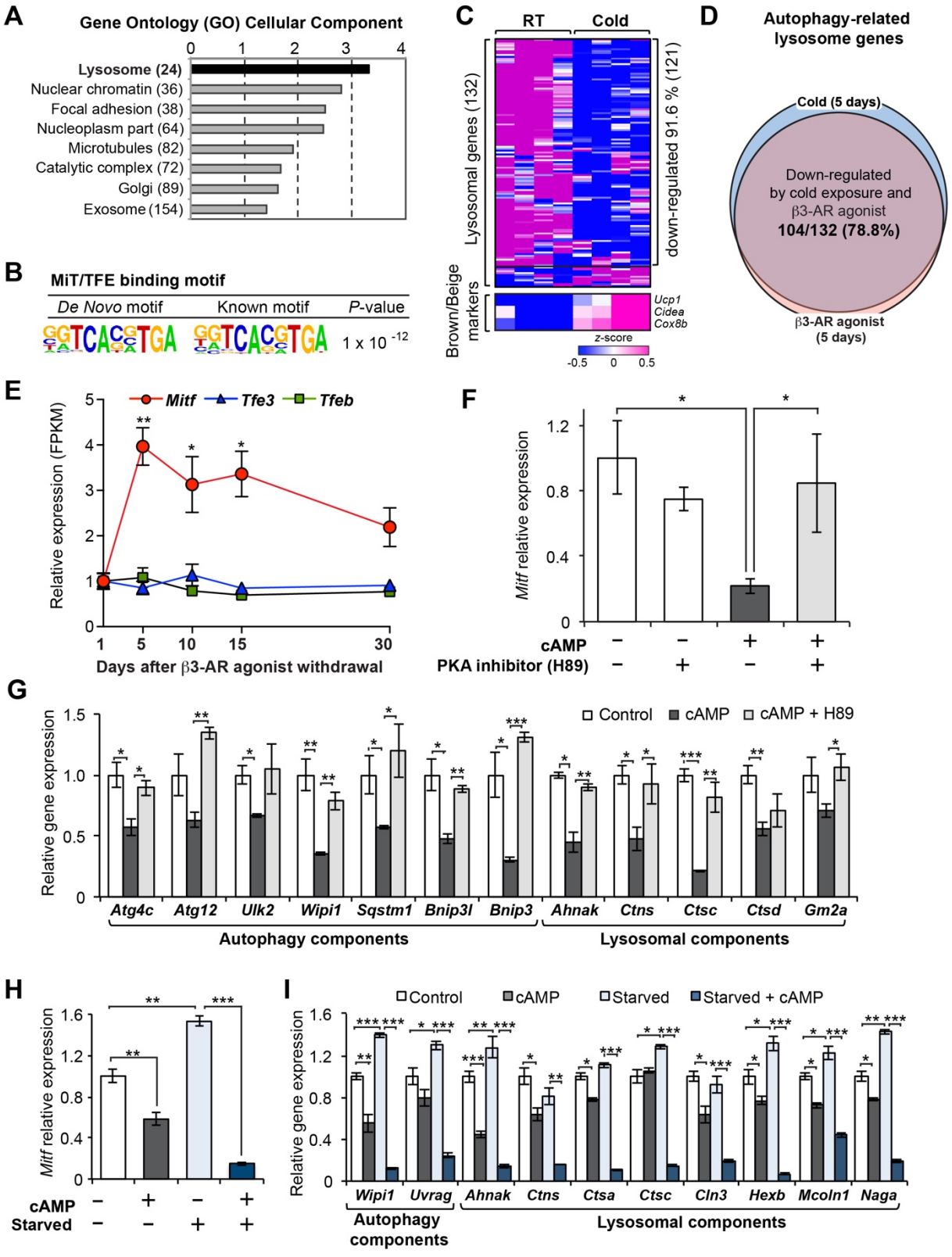
A
Gene Ontology (GO) Cellular Component
Lysosome (24)
Nuclear chromatin (36)
Focal adhesion (38)
Nucleoplasm part (64)
Microtubules (82)
Catalytic complex (72)
Golgi (89)
Exosome (154)
B
MiT/TFE binding motif
De Novo motif
Known motif
P-value
1 x 10 -12
C
RT
Cold
Lysosomal genes (132)
down-regulated 91.6 % (121)
Brown/Beige markers
Ucp1
Cidea
Cox8b
z-score
D
Autophagy-related lysosome genes
Cold (5 days)
Down-regulated by cold exposure and β3-AR agonist
104/132 (78.8%)
β3-AR agonist (5 days)
E
Mitf
Tfe3
Tfeb
Relative expression (FPKM)
Days after β3-AR agonist withdrawal
F
Mitf relative expression
cAMP
PKA inhibitor (H89)
G
Control
cAMP
cAMP + H89
Relative gene expression
Atg4c
Atg12
Ulk2
Wipi1
Sqstm1
Bnip3l
Bnip3
Ahnak
Ctns
Ctsc
Ctsd
Gm2a
Autophagy components
Lysosomal components
H
Mitf relative expression
cAMP
Starved
I
Control
cAMP
Starved
Starved + cAMP
Relative gene expression
Wipi1
Uvrag
Ahnak
Ctns
Ctsa
Ctsc
Cln3
Hexb
Mcoln1
Naga
Autophagy components
Lysosomal components

Figure 5. Regulation of autophagy-related lysosome biogenesis through MiT/TFE transcription factors during the beige-to-white adipocyte transition. (**A**) GO analysis (cellular component) of the genes transiently activated during the beige-to-white adipocyte transition (Gene cluster 2). **(B)** The HOMER-based motif analysis of lysosome genes in (A). **(C)** Expression of lysosome marker genes in the inguinal WAT of mice housed under cold or ambient temperature for 5 days. FPKM values were converted to z-score and visualized in blue (low)–white (no change)–red (high) color scheme. n=5. **(D)** Regulation of the autophagy-related lysosome genes by cold exposure (shown in C) and by chronic ß3-AR agonist treatment for 5 days. Note that 78.8% of the autophagy-related lysosome genes (104 out of 132 genes) were down-regulated both by cold exposure and ß3-AR agonist. (**E**) Relative expression of MiT/TFE members of transcription factors (*Mitf, Tfe3*, and *Tfeb*) during the beige-to-white adipocyte transition. * P <0.05, ** P <0.01 by two-tailed Student's *t*-test. n = 3. Data are expressed as means ± s.e.m as compared to day 1 after β3-AR agonist treatment. (**F**) Regulation of *Mitf* mRNA expression in response to cAMP in the presence or absence of a PKA inhibitor H89. Differentiated beige adipocytes were treated with by 10 μM forskolin (cAMP) for 4hr in the presence or absence of H89 at a dose of 10 μM. H89 was added 1 hr prior to forskolin treatment. * P <0.05, by two-tailed Student's *t*-test. n = 3. Data are expressed as means ± s.e.m. (**G**) mRNA expression of autophagy components that are known targets of MiT/TFE transcription factors. * P <0.05, ** P <0.01, *** P <0.001 by two-tailed Student's *t*-test. n = 3. Data are expressed as means ± s.e.m. (**H**) Regulation of *Mitf* mRNA expression in response to cAMP in a regular medium or amino acid depletion medium (starved). Differentiated beige adipocytes were cultured in amino acid free medium

supplemented with 10% dialyzed serum for 4hr prior to forskolin (cAMP) treatment (10 μM, 4hr). ** P <0.01, *** P <0.001 by two-tailed Student's t-test. n = 3. Data are expressed as means ± s.e.m. (**I**) mRNA expression of the MI/TFE-target autophagy-related genes in response to cAMP under a fed or fasted state. * P <0.05, ** P <0.01, *** P <0.001 by two-tailed Student's t-test. n = 3. Data are expressed as means ± s.e.m.

Figure 6

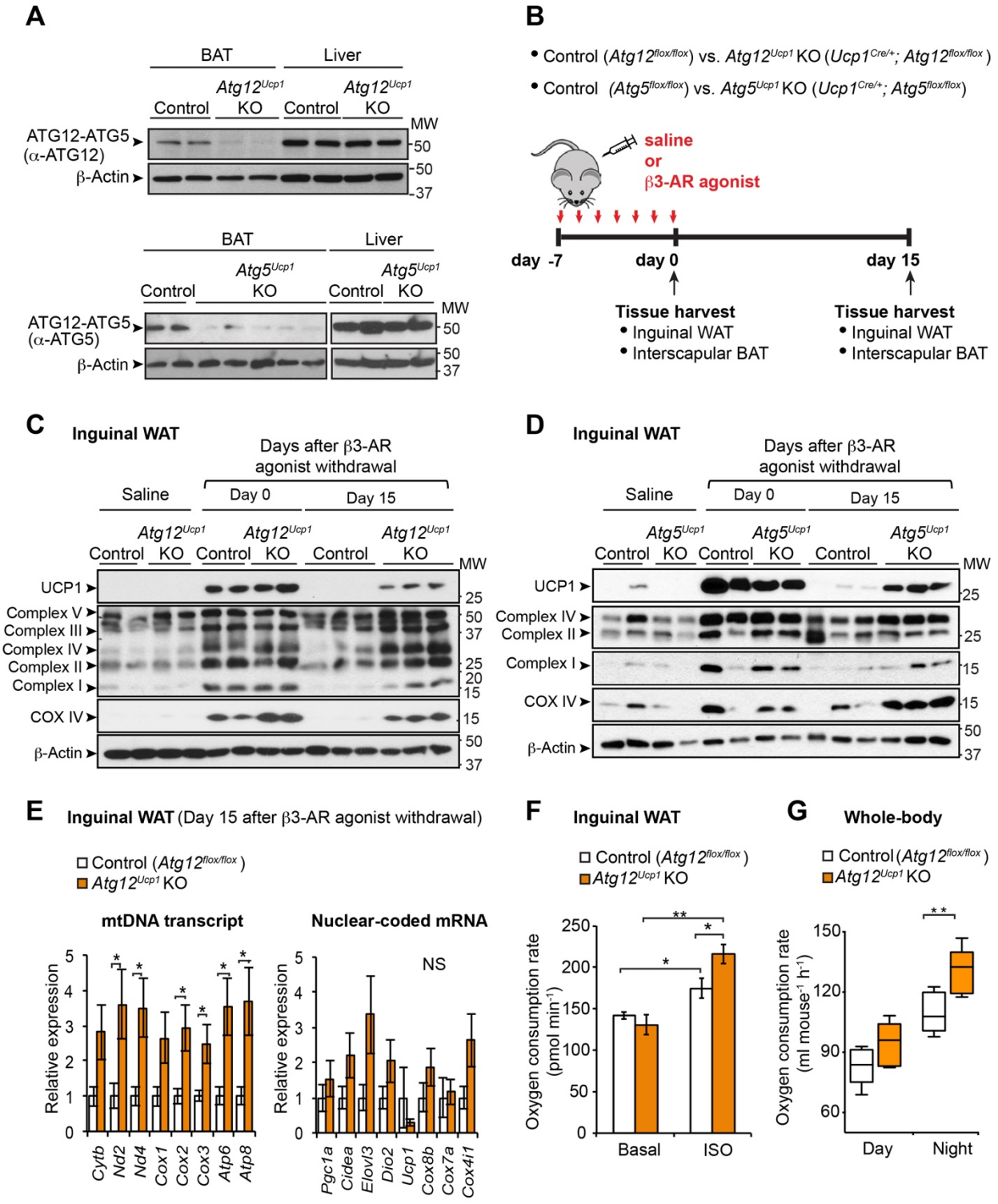
A
BAT
Liver
Atg12Ucp1
Control
KO
ATG12-ATG5 (α-ATG12)
β-Actin
MW
50
37
Atg5Ucp1
ATG12-ATG5 (α-ATG5)
B
Control (Atg12flox/flox) vs. Atg12Ucp1 KO (Ucp1Cre/+; Atg12flox/flox)
Control (Atg5flox/flox) vs. Atg5Ucp1 KO (Ucp1Cre/+; Atg5flox/flox)
saline
or
β3-AR agonist
day -7
day 0
day 15
Tissue harvest
Inguinal WAT
Interscapular BAT
C
Inguinal WAT
Days after β3-AR agonist withdrawal
Saline
Day 0
Day 15
UCP1
Complex V
Complex III
Complex IV
Complex II
Complex I
COX IV
D
E
Inguinal WAT (Day 15 after β3-AR agonist withdrawal)
mtDNA transcript
Nuclear-coded mRNA
Relative expression
Cytb
Nd2
Nd4
Cox1
Cox2
Cox3
Atp6
Atp8
NS
Pgc1a
Cidea
Elovl3
Dio2
Ucp1
Cox8b
Cox7a
Cox4i1
F
Inguinal WAT
Oxygen consumption rate (pmol min-1)
Basal
ISO
G
Whole-body
Oxygen consumption rate (ml mouse-1 h-1)
Day
Night

Figure 6. Genetic ablation of *Atg12* or *Atg5* maintains beige adipocyte characteristics after removal of ß3-AR agonist. (**A**) Immmunoblotting for the ATG12-ATG5 complex in the interscapular BAT and liver of control (*Atg12*$^{flox/flox}$) and *Atg12*^{Ucp1} KO (*Ucp1*$^{Cre/+}$;*Atg12*$^{flox/flox}$) mice (left) or control (*Atg5*$^{flox/flox}$) and *Atg5*^{Ucp1} KO (*Ucp1*$^{Cre/+}$;*Atg5*$^{flox/flox}$) mice (right) ß-actin was used as a loading control. Molecular weight (MW) is shown on the right. (**B**) Schematic illustration of experiments. Control (*Atg12*$^{flox/flox}$ *or* *Atg5*$^{flox/flox}$), *Atg12*^{Ucp1} KO (*Ucp1*$^{Cre/+}$;*Atg12*$^{flox/flox}$), and *Atg5*^{Ucp1} KO (*Ucp1*$^{Cre/+}$;*Atg5*$^{flox/flox}$) mice were treated with the ß3-AR agonist CL316,243 at 1mg kg^{-1} for seven consecutive days. Interscapular BAT and inguinal WAT depots were harvested for molecular analyses at day 0 and 15 following ß3-AR agonist withdrawal. (**C**) Immunoblotting for UCP1 and mitochondrial complexes (as indicated) in the inguinal WAT depots of control (*Atg12*$^{flox/flox}$) and *Atg12*^{Ucp1} KO mice at day 0 and day 15 following ß3-AR agonist withdrawal. Inguinal WAT depots from control and *Atg12*^{Ucp1} KO mice treated with saline were included as a reference of basal expression of UCP1 and mitochondrial complexes. ß-actin was used as a loading control. Molecular weight (MW) is shown on the right. (**D**) Immunoblotting for UCP1 and mitochondrial complexes (as indicated) in the inguinal WAT depots of control (*Atg5*$^{flox/flox}$) and *Atg5*^{Ucp1} KO mice. Samples were harvested as illustrated in (B). (**E**) Left, Mitochondrial DNA (mtDNA) transcripts (as indicated) were quantified in the inguinal WAT depots of control (*Atg12*$^{flox/flox}$) and *Atg12*^{Ucp1} KO mice at day 15 following ß3-AR agonist withdrawal. Right, mRNA levels of nuclear-coded beige-enriched markers (as indicated) are shown. * P <0.05 by two-tailed Student's t-test. n = 5. Data are expressed as means ± s.e.m. (**F**) Oxygen consumption rate (OCR) in the inguinal WAT depots of control (*Atg12*$^{flox/flox}$) and *Atg12*^{Ucp1} KO mice at

day 15 following ß3-AR agonist withdrawal. The isolated tissues were treated with isoproterenol or vehicle (basal). OCR was measured using the Seahorse XFe Extracellular Flux Analyzer and the data were shown per 1 mg of tissue. * $P < 0.05$, ** $P < 0.01$ by two-tailed Student's *t*-test. $n = 4$. Data are expressed as means ± s.e.m. (**G**) Quantification of whole-body oxygen consumption rate (VO_2) of control (*Atg12*$^{flox/flox}$) and *Atg12*^{Ucp1} KO mice during day 17-18 following ß3-AR agonist withdrawal. VO_2 was measured during day and night time. ** $P <0.01$ by two-tailed Student's *t*-test. $n = 5$ per genotype. Data are expressed as means ± s.e.m.

Figure 7

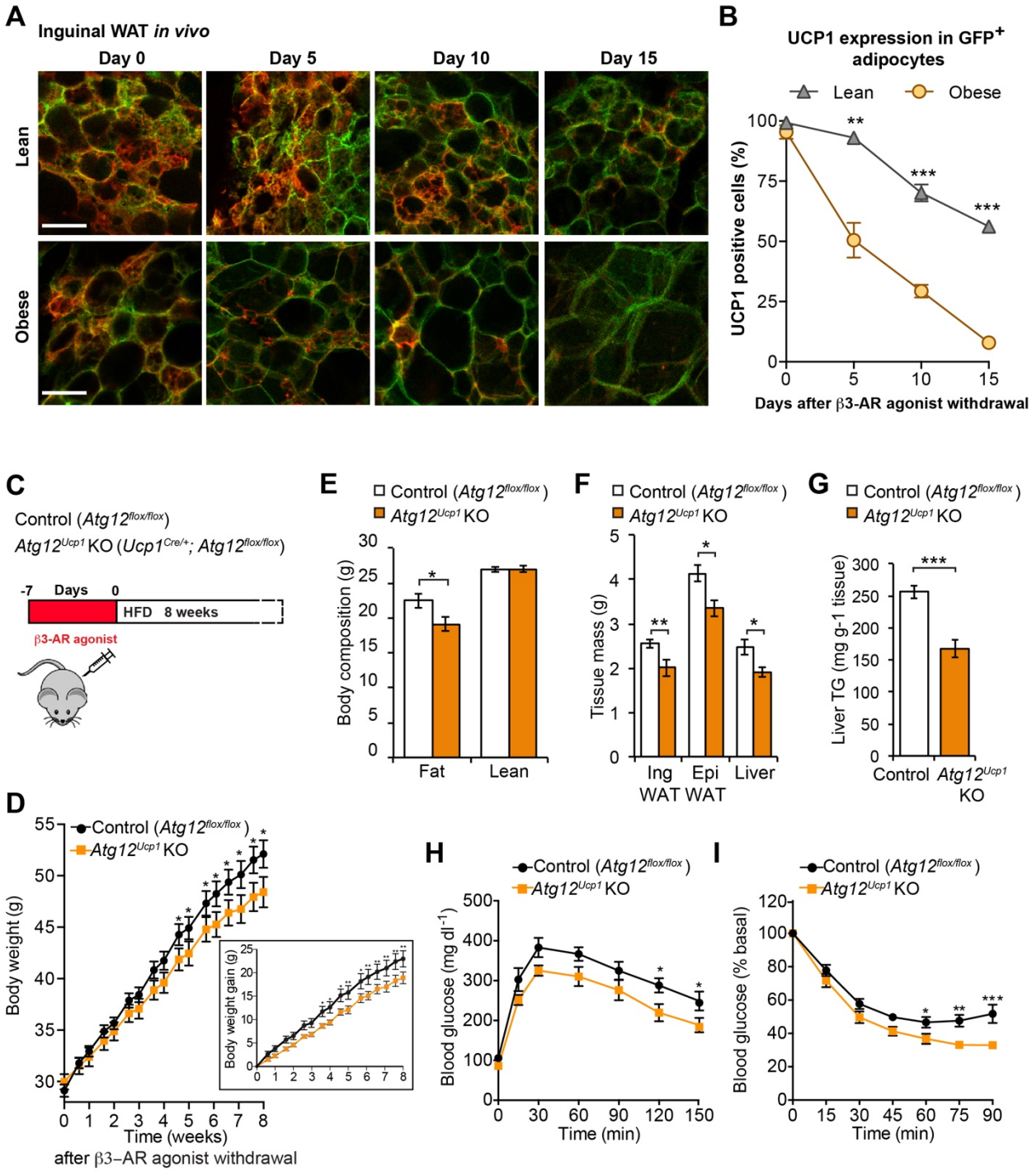
A
Inguinal WAT in vivo
Day 0
Day 5
Day 10
Day 15
Lean
Obese
B
UCP1 expression in GFP+ adipocytes
Lean
Obese
UCP1 positive cells (%)
Days after β3-AR agonist withdrawal
C
Control (Atg12flox/flox)
Atg12Ucp1 KO (Ucp1Cre/+; Atg12flox/flox)
-7 Days 0
HFD 8 weeks
β3-AR agonist
D
Control (Atg12flox/flox)
Atg12Ucp1 KO
Body weight (g)
Body weight gain (g)
Time (weeks)
after β3–AR agonist withdrawal
E
Control (Atg12flox/flox)
Atg12Ucp1 KO
Body composition (g)
Fat
Lean
F
Control (Atg12flox/flox)
Atg12Ucp1 KO
Tissue mass (g)
Ing WAT
Epi WAT
Liver
G
Control (Atg12flox/flox)
Atg12Ucp1 KO
Liver TG (mg g-1 tissue)
Control
Atg12Ucp1 KO
H
Control (Atg12flox/flox)
Atg12Ucp1 KO
Blood glucose (mg dl-1)
Time (min)
I
Control (Atg12flox/flox)
Atg12Ucp1 KO
Blood glucose (% basal)
Time (min)

Figure 7. Maintenance of beige adipocytes by autophagy inhibition protects animals from diet-induced obesity and insulin resistance. (**A**) Confocal images of fixed inguinal WAT sections from *Ucp1*$^{Cre/+}$*;mT/mG* reporter mice. Inguinal WAT depots from lean mice under a regular diet (top panel, body weight, 29.5 ± 1.4 g) and age-matched obese mice under a high-fat diet for x weeks (bottom panel, body weight, 49.8 ± 0.8 g) were immunostained for endogenous UCP1. Note that the cellular membranes of beige adipocytes were visualized by membrane-targeted GFP of the mT/mG reporter mice. Scale bar, 57 μm. **(B)** Quantification of mGFP-positive adipocytes in lean and obese mice that express endogenous UCP1 in (A). n = 100 cells or more per group. ** P <0.01, *** P <0.001 by two-tailed Student's *t*-test. (**C**) Schematic of the metabolic experiment in control (*Atg12*$^{flox/flox}$) and *Atg12*^{Ucp1} KO mice. Control and *Atg12*^{Ucp1} KO mice were treated with CL316,243 for seven days to induce beige adipocyte biogenesis. Subsequently, the mice were acclimated to thermoneutrality (30 ˚C) under a high-fat diet for 8 weeks. (**D**) Body weight of control (*Atg12*$^{flox/flox}$) and *Atg12*^{Ucp1} KO mice under a high-fat diet. Body weight was measured twice a week. * P <0.05, ** P <0.01. n = 8 – 10 per genotype. The graph in the inset shows body weight gain of control and *Atg12*^{Ucp1} KO mice. Significance was determined by two-way repeated-measures ANOVA followed by Fisher's LSD test. Data are expressed as means ± s.e.m. (**E**) Body composition of control (*Atg12*$^{flox/flox}$) and *Atg12*^{Ucp1} KO mice from (D) at the end of 8 weeks of high-fat diet. * P <0.05 by two-tailed Student's *t*-test. Data are expressed as means ± s.e.m. (**F**) Tissue weight of inguinal WAT, epididymal WAT, and liver from control (*Atg12*$^{flox/flox}$) and *Atg12*^{Ucp1} KO mice from (D) after 9 weeks of high fat diet. * P <0.05, ** P <0.01. Data are expressed as means ± s.e.m. (**G**) Liver triglyceride levels in control (*Atg12*$^{flox/flox}$) and *Atg12*^{Ucp1} KO mice after 9

weeks of high fat diet. *** P <0.001. Data are expressed as means ± s.e.m.(**H**) After 8 weeks of high-fat diet, control (*Atg12*$^{flox/flox}$) and *Atg12*^{Ucp1} KO mice were fasted for 12 hours and injected with 1.5g kg^{-1} glucose. Whole-body glucose was measured at 15, 30, 60, 90, 120, and 150 min. * P <0.05, n = 6 - 8 per genotype. Significance was determined by two-way repeated-measures ANOVA followed by Fisher's LSD test. Data are expressed as means ± s.e.m. (**I**) After 8.5 weeks of high fat diet diet, control (*Atg12*$^{flox/flox}$) and *Atg12*^{Ucp1} KO mice were fasted for 3 hours and injected with 0.75 U kg^{-1} insulin. Whole-body glucose was measured at 15, 30, 45, 60, 75, and 90 min. * P <0.05, ** P <0.001, *** P <0.0001, n = 7-8 per genotype. Significance was determined by two-way repeated-measures ANOVA followed by Fisher's LSD test. Data are expressed as means ± s.e.m.

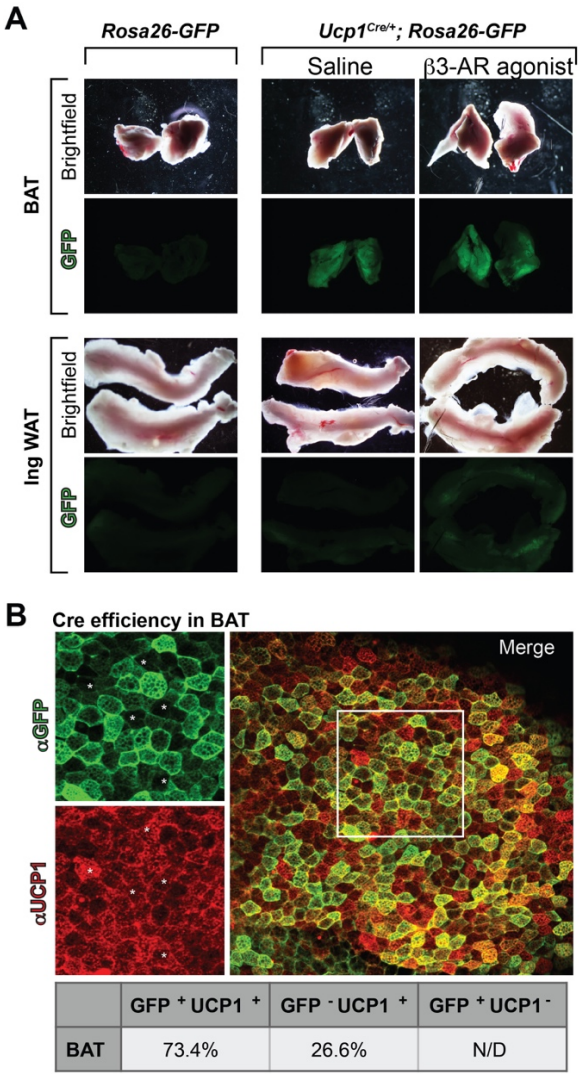

	GFP + UCP1 +	GFP - UCP1 +	GFP + UCP1 -
BAT	73.4%	26.6%	N/D

Supplementary Figure 1. The experimental system to monitor brown and beige adipocytes *in vivo.* (**A**) Endogenous GFP expression in the interscapular BAT and inguinal WAT of control (*Rosa26-GFP)* and *Ucp1*$^{Cre/+}$*;Rosa26-GFP* reporter mice following treatment with the ß3-AR agonist CL316,243 at 1mg kg^{-1} for seven consecutive days under thermoneutrality (30˚C). Mice were bred and maintained under thermoneutrality. Tissue analysis was carried out immediately after ß3-AR agonist withdrawal (day 0). Note that GFP positive adipocytes were detected in the interscapular BAT in the presence or absence of ß3-AR agonist. In contrast, in the inguinal WAT beige adipocytes emerge only after chronic treatment with ß3-AR agonist. *n* = 3-4. (**B**) *Cre* efficiency was determined in the interscapular BAT of *Ucp1*$^{Cre/+}$*;Rosa26-GFP* reporter mice by counting the number of UCP1^{+} cells that did not express GFP. Cre efficiently labeled approximately 73% of UCP1-expressing cells. Note that GFP^{+} cell that did not express UCP1 were not observed (N/D, not detected). *n* = 551. White asterisks are labeling UCP1^{+} GFP^{-} cells.

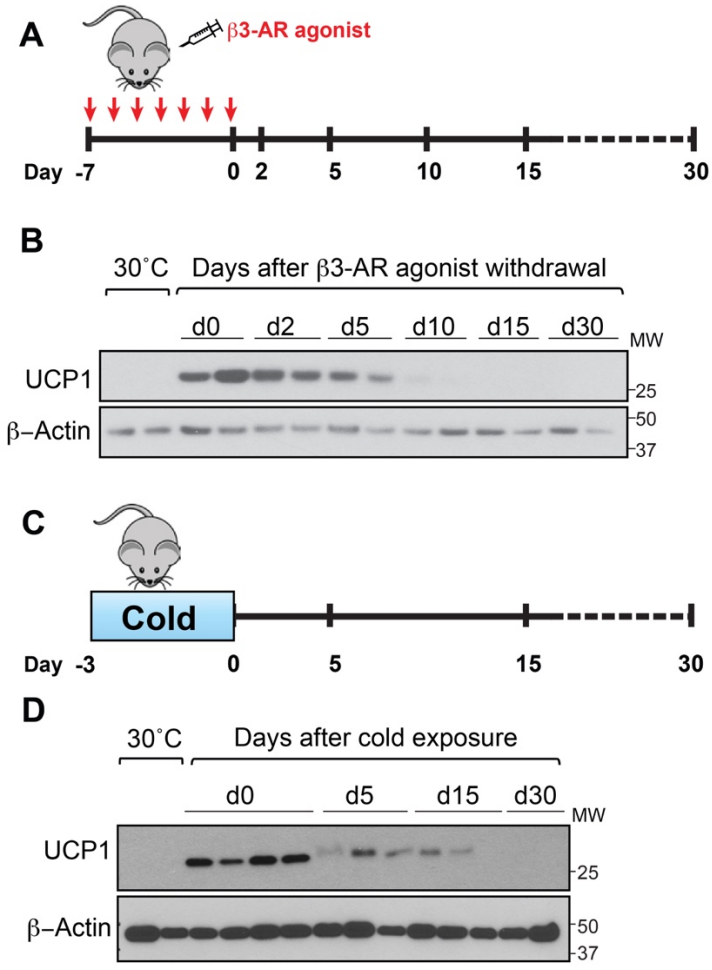

Supplementary Figure 2. Time-dependent decline in endogenous UCP1 expression in the inguinal WAT after withdrawal of external cues. (**A**) Schematic illustration of experiments. Wild-type mice were treated with the ß3-AR agonist CL316,243 at 1mg kg^{-1} for seven consecutive days. Inguinal WAT depots were harvested for molecular analyses at indicated time points after withdrawing ß3-AR agonist. (**B**) Immunoblotting for UCP1 in the inguinal WAT of mice under thermoneutrality (30˚C) before ß3-AR agonist treatment at indicated time points after withdrawing ß3-AR agonist. ß-actin was used as a loading control. (**C**) Schematic illustration of experiments. Wild-type mice were exposed to cold (6˚C) for three consecutive days. Inguinal WAT depots were harvested for molecular analysis at indicated time-points after acclimation to ambient temperature. (**D**) Immunoblotting for UCP1 in the inguinal WAT of mice under thermoneutrality (30˚C) at indicated time points after acclimation to ambient temperature. ß-actin was used as a loading control. Note that the time-dependent decline in UCP1 expression after acclimation to ambient temperature was similar to the decline found after ß3-AR agonist withdrawal in (B).

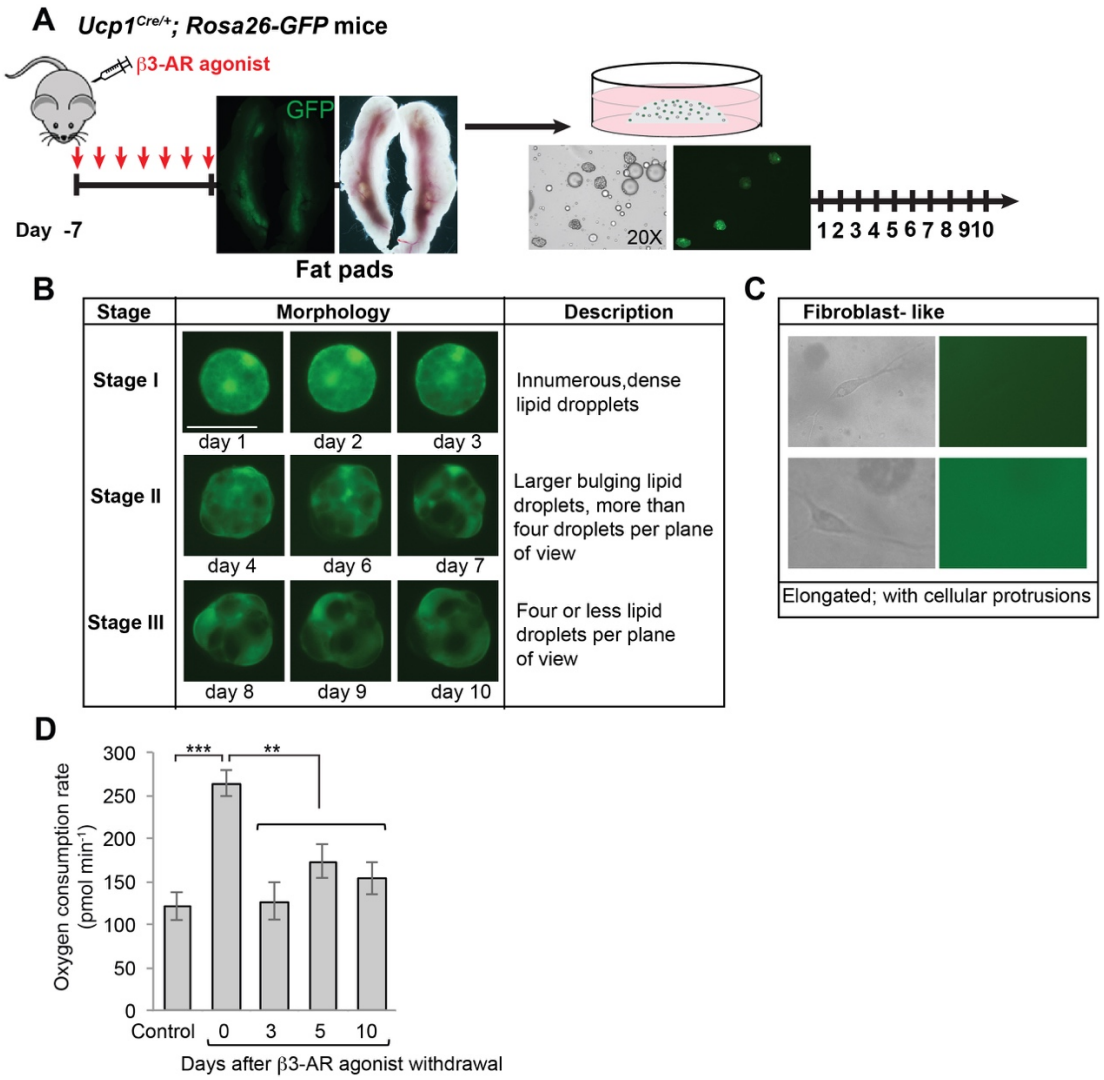

Supplementary Figure 3. Ex vivo system to track morphological and functional changes of beige adipocytes. (**A**) Schematic illustration to monitor individual beige adipocytes *ex vivo* in response to chronic treatment with ß3-AR agonist CL316,243 at 1mg kg^{-1} for seven days. Inguinal WAT depots from *Ucp1*$^{Cre/+}$*;Rosa26-GFP* mice were isolated immediately after chronic treatment with ß3-AR agonist, digested to single cells, embedded in Collagen I gel, and maintained in a live cell culture for ten consecutive days. Culture medium did not contain any stimuli, such as ß3-AR agonist, that control beige adipocyte differentiation. (**B**) Morphological changes occurring between day 1-10 of culture were categorized into three stages (Stage I, Stage II, Stage III) based on lipid content *per* plane view. (**C**) Examples of fibroblast-like cells present amongst GFP-positive adipocytes. Note that GFP-positive fibroblast-like cells were not observed at any time point of the culture. (**D**) Basal oxygen consumption rate of the *ex vivo* cultured inguinal WAT from wild-type mice at indicated days after ß3-AR agonist withdrawal. Inguinal WAT depots from wild-type animals under thermoneutrality were used as a control. ** P <0.001, *** P <0.0001, by two-tailed Student's t-test, n = 3 - 6 technical replicates. Data are expressed as means ± s.e.m.

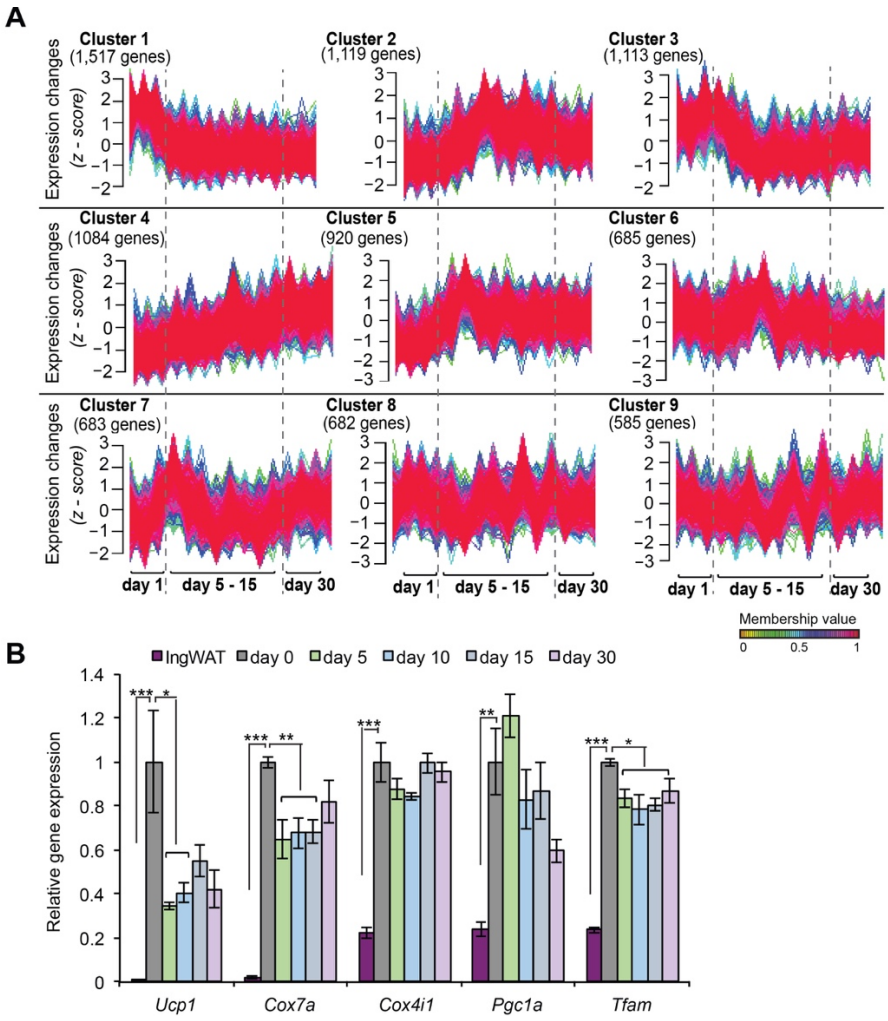

Supplementary Figure 4. Gene expression profile of beige adipocytes and BAT following β3-AR agonist withdrawal. (**A**) The Fuzzy C-Means (FCM) clustering was performed to identify gene clusters that exhibited similar expression profiles. The *z*-transformed profiles of beige adipocytes during the beige-to-white transition (day 0–30) underwent the FCM clustering. Color represents the likelihood of a gene belonging to each gene cluster, red (most likely)- blue- yellow (least likely). The identified 9 clusters were numbered from most populated to least populated by gene sets. Cluster I, containing 1517 genes, exhibited the most frequent gene expression profile. Y-axis represents expression changes in the expression level (*z*-scored FPKM) of each gene. The genes for Cluster I are listed in Supplementary Table1. (**B**) Gene expression profiles of brown/beige-enriched mitochondrial genes (*Ucp1*, *Cox7a* and *Cox4i1*) and mitochondrial biogenesis genes (*Pgc1a* and *Tfam*) in the interscapular BAT depots at indicated time points after ß3-AR agonist withdrawal. As a reference, expression levels of each gene in inguinal WAT are shown. * P <0.05, ** P <0.01, *** P <0.001 by two-tailed Student's *t*-test. n = 3. Data are expressed as means ± s.e.m.

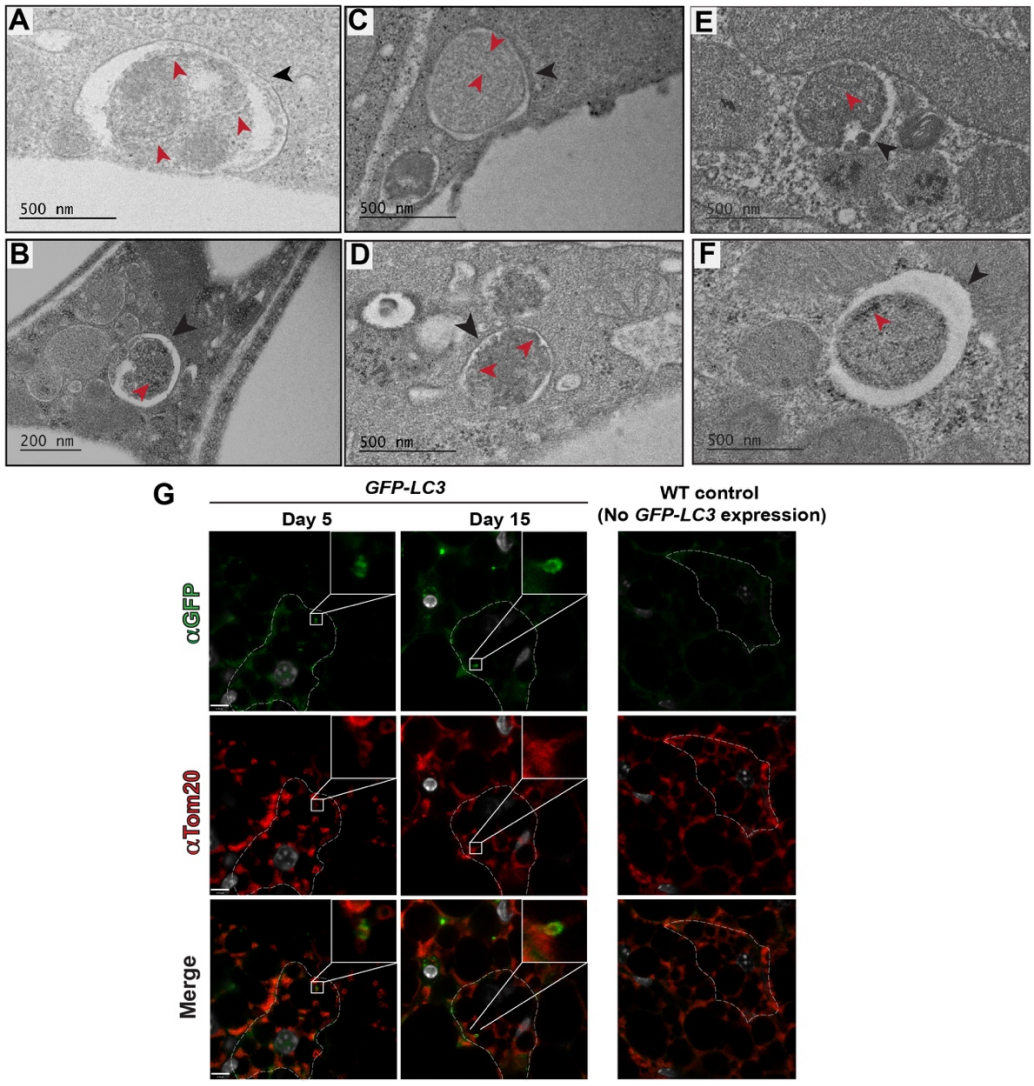

Supplementary Figure 5. Morphological evidence of mitophagy in beige adipocytes following β3-AR agonist withdrawal. (**A - F**) Electron microscopy (EM) images were obtained in beige adipocytes during the transition phase. (**A and B**) Adipocytes at day 5 following ß3-AR agonist withdrawal. (**C and D**) Adipocytes at day 10. (**E and F**) Adipocytes at day 15. Black arrowheads indicate the autophagic vesicles containing mitochondrial remnants, as identified by remaining cristae (red arrowheads). (**G**) Cross section through confocal stacks of beige adipocytes from *GFP-LC3* mice during the beige-to-white adipocyte transition (Left, day 5 following ß3-AR agonist withdrawal; Right, day 15). Beige adipocytes from wild-type mice (no GFP-LC3 expression) were included as negative control to confirm the specificity of GFP staining. Mitochondria and LC3 were visualized by immunohistochemistry for Tom20 (red) and GFP (green), respectively. The image in inset shows co-localization of GFP and Tom20. Nuclei are labeled with Hoechst (grey). Scale bar, 6 μm.

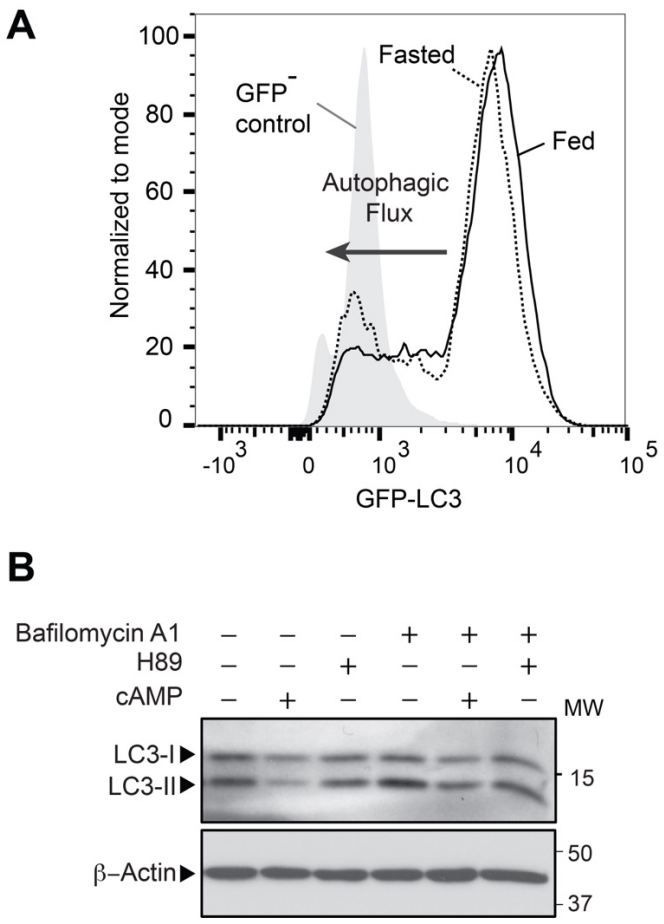

Supplementary Figure 6. Measuring autophagic flux in beige adipocytes.

(**A**) Twenty-four hours of fasting led to a decrease in GFP-LC3 fluorescence, indicating an increase in autophagic flux. Wild-type animal was used as control for GFP fluorescence. X-axis represents GFP-LC3 fluorescence intensity and Y-axis represents the number of adipocytes normalized to mode. Analysis was done using FlowJo software. (**B**) Immunoblotting for LC3 in primary beige adipocytes following treatments with Bafilomycin A1, cAMP (forskolin), and H89. Differentiated beige adipocytes were treated with forskolin at a dose of 10 μM in the presence and absence of Bafilomycin A1 (50 nM) for 2 hours. The PKA inhibitor H89 at a dose of 10 μM was added 1 hr prior to forskolin treatment.

A

De Novo Motif	Known Motif	TF	*P* - value
		FOXO3 (MA0157.2)	1 x 10^{-2}

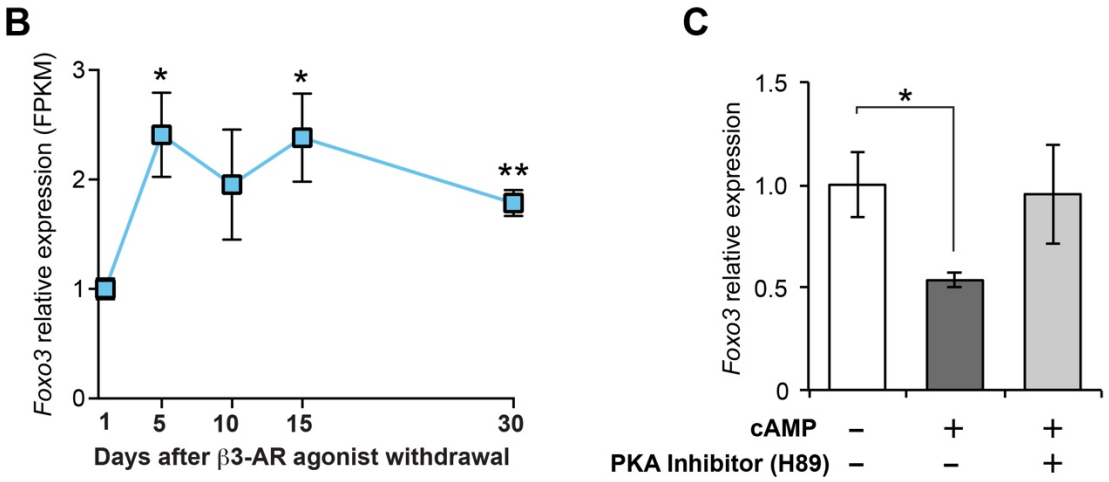

Supplementary Figure 7. Regulation of *Foxo3* expression in beige adipocytes.

(A) The HOMER-based motif analysis of lysosome genes in Figure 5A (**B**) Relative expression of *Foxo3* during the beige-to-white adipocyte transition. * P <0.05, ** P <0.01, by two-tailed Student's *t*-test. n = 3. Data are expressed as means ± s.e.m. (**C**) mRNA expression of *Foxo3* in response to cAMP in the presence or absence of the PKA inhibitor H89. Differentiated beige adipocytes were treated with forskolin (cAMP) at a dose of 10 μM for 4hr in the presence or absence of H89. The PKA inhibitor H89 at a dose of 10 μM was added 1 hr prior to forskolin treatment. * P <0.05 by two-tailed Student's *t*-test. n = 3. Data are expressed as means ± s.e.m.

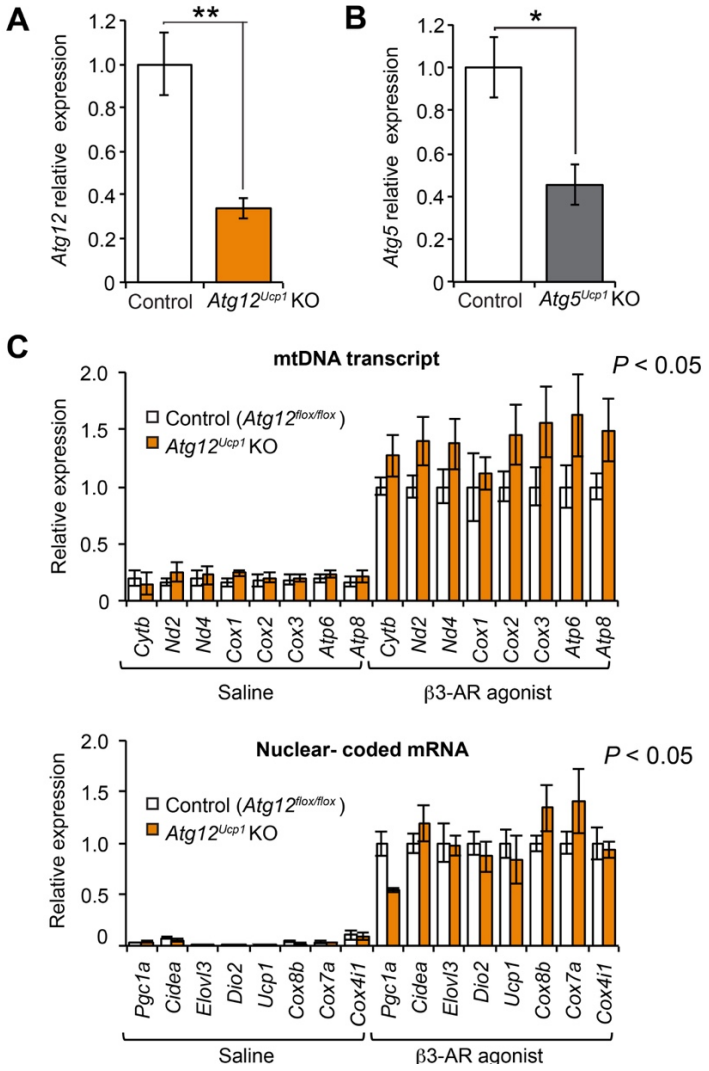

Supplementary Figure 8. Molecular characterization of the inguinal WAT depots in *Atg12*^{Ucp1} KO mice and *Atg5*^{Ucp1} KO mice. (**A**) *Atg12* mRNA levels in beige adipocytes from control and *Atg12*^{Ucp1}KO mice. Beige adipocytes were isolated by FACS from control (*Ucp1*$^{Cre/+}$*; Rosa26-GFP)* and *Atg12*^{Ucp1}KO (*Ucp1*$^{Cre/+;}$*Atg12*$^{flox/flox}$*;Rosa26-RFP)* mice following 5 days of cold exposure. mRNA expression of *Atg12* was measured by qPCR. ** *P* <0.01 by two-tailed Student's *t*-test. *n* = 3-4. Data are expressed as means ± s.e.m. (**B**) *Atg5* mRNA levels in beige adipocytes from control and *Atg5*^{Ucp1}KO mice. Beige adipocytes were isolated by FACS from control (*Ucp1*$^{Cre/+}$*; Rosa26-GFP)* and *Atg5*^{Ucp1}KO (*Ucp1*$^{Cre/+;}$*Atg5*$^{flox/flox}$*;Rosa26-RFP)* mice following 5 days of cold exposure. mRNA expression of *Atg5* was measured by qPCR. * *P* <0.05 by two-tailed Student's *t*-test. *n* = 3. Data are expressed as means ± s.e.m. (**C**) Mitochondrial DNA (mtDNA) transcripts (upper panel, as indicated) and mRNA transcript of nuclear-coded beige fat-enriched genes (lower panel, as indicated) were quantified in the inguinal WAT depots of control (*Atg12*$^{flox/flox}$) and *Atg12*^{Ucp1} KO mice chronically treated with saline or ß3-AR agonist for seven consecutive days. *n* = 4. Data are expressed as means ± s.e.m. Expression of all the indicated genes was significantly increased in the Inguinal WAT of ß3-AR agonist treated mice, as compared to saline-treated mice (*P* < 0.05).

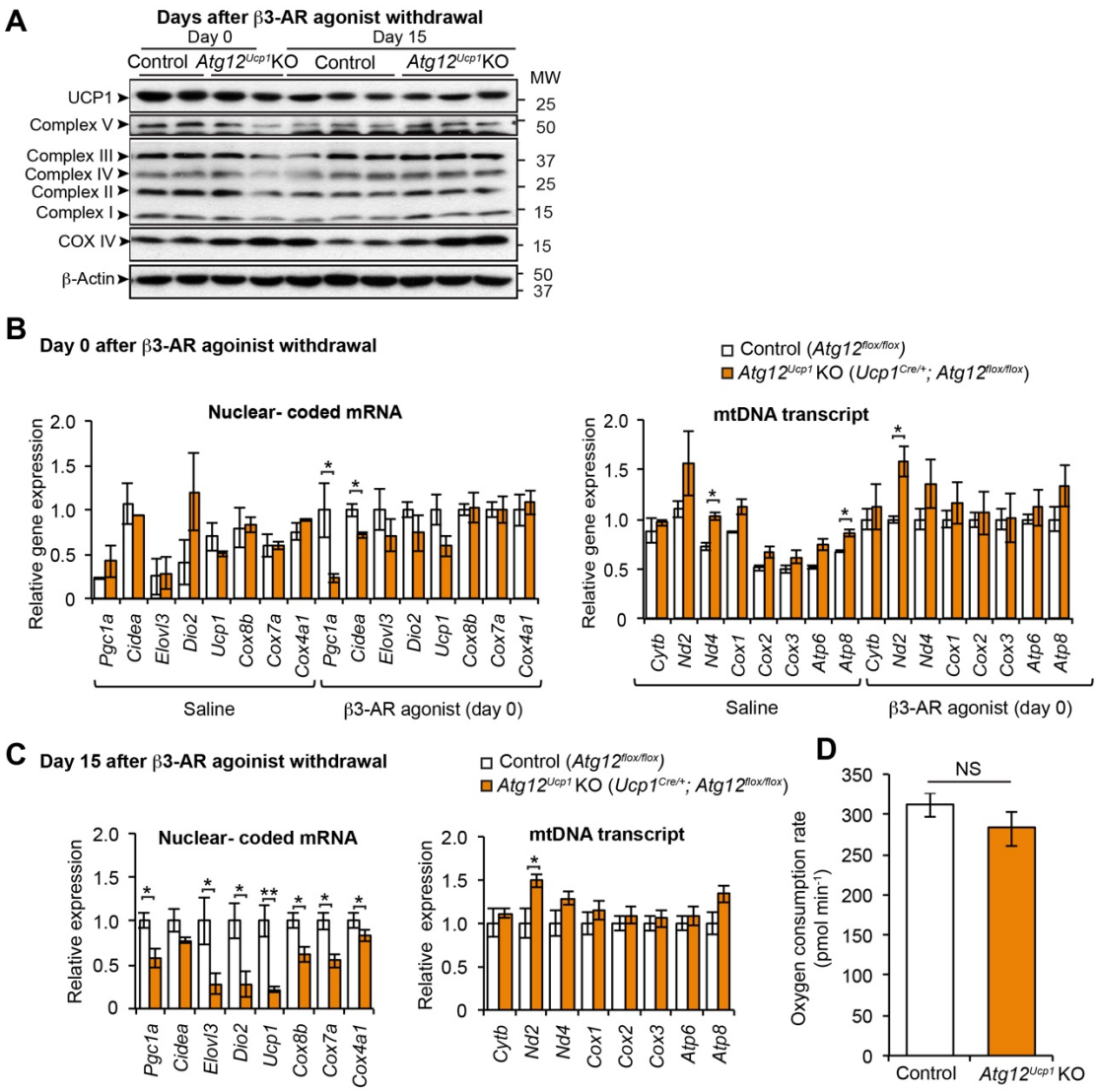

Supplementary Figure 9. Phenotype of the interscapuar BAT depots in *Atg12*^{Ucp1} KO mice. (**A**) Immunoblotting for UCP1 and mitochondrial complexes (as indicated) in the interscapular BAT of control (*Atg12*$^{flox/flox}$) and *Atg12*^{Ucp1} KO (*Ucp1*$^{Cre/+;}$*Atg12*$^{flox/flox}$) mice at day 0 and day 15 following ß3-AR agonist withdrawal. (**B**) mRNA transcript of nuclear-coded BAT-markers and mitochondrial DNA (mtDNA) transcripts were quantified in the BAT depots of control (*Atg12*$^{flox/flox}$) and *Atg12*^{Ucp1} KO (*Ucp1*$^{Cre/+;}$*Atg12*$^{flox/flox}$) mice that were chronically treated with saline or ß3-AR agonist for seven consecutive days (day 0, right after the end of seven-day ß3-AR agonist treatment). n = 4. Data are expressed as means ± s.e.m. (**C**) mRNA transcript of nuclear-coded BAT-markers and mitochondrial DNA (mtDNA) transcripts were quantified in the BAT depots of control (*Atg12*$^{flox/flox}$) and *Atg12*^{Ucp1} KO (*Ucp1*$^{Cre/+;}$*Atg12*$^{flox/flox}$) mice 15 days after ß3-AR agonist treatment. (**D**) Oxygen consumption rate (OCR) in the interscapular BAT depots of control (*Atg12*$^{flox/flox}$) and *Atg12*^{Ucp1} KO mice. OCR was measured using the Seahorse XFe Extracellular Flux Analyzer and the data were shown per 1 mg of tissue. Data are expressed as means ± s.e.m.

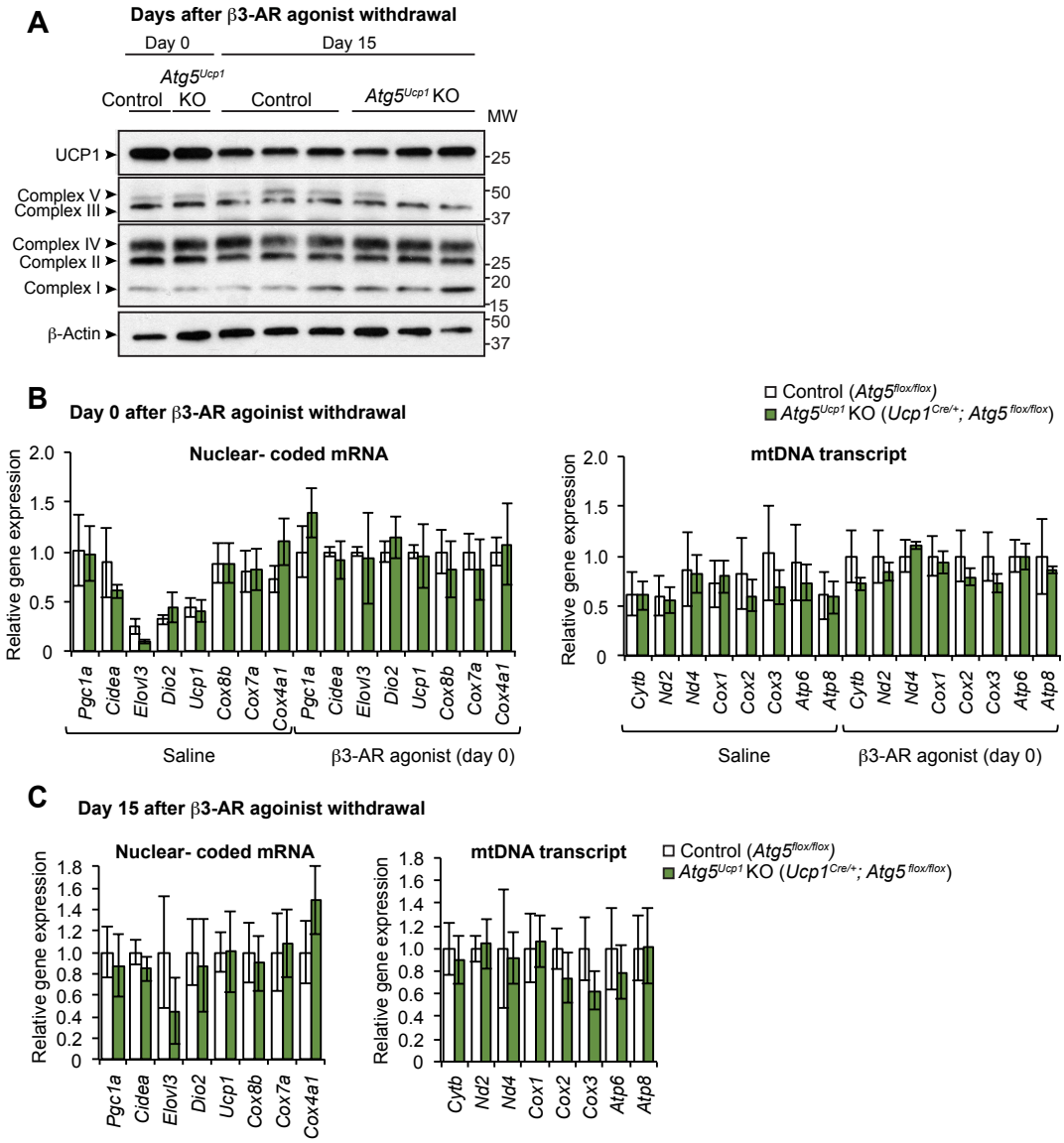

Supplementary Figure 10. Phenotype of the interscapuar BAT depots in *Atg5^{Ucp1}* KO mice. (**A**) Immunoblotting for UCP1 and mitochondrial complexes (as indicated) in the interscapular BAT of control (*Atg5$^{flox/flox}$*) and *Atg5^{Ucp1}* KO (*Ucp1$^{Cre/+;}$Atg5$^{flox/flox}$*) mice at day 0 and day 15 following ß3-AR agonist withdrawal. ß-actin was used as a loading control. Molecular weight (MW) is shown on the right. (**B**) mRNA transcript of nuclear-coded BAT-markers and mitochondrial DNA (mtDNA) transcripts were quantified in the BAT depots of control (*Atg5$^{flox/flox}$*) and *Atg5^{Ucp1}* KO (*Ucp1$^{Cre/+;}$Atg5$^{flox/flox}$*) mice that were chronically treated with saline or ß3-AR agonist for seven consecutive days (day 0, right after the end of seven-day ß3-AR agonist treatment). n = 5. Data are expressed as means ± s.e.m. (**C**) mRNA transcript of nuclear-coded BAT-markers and mitochondrial DNA (mtDNA) transcripts were quantified in the BAT depots of control (*Atg5$^{flox/flox}$*) and *Atg5^{Ucp1}* KO (*Ucp1$^{Cre/+;}$Atg5$^{flox/flox}$*) mice 15 days after ß3-AR agonist treatment.

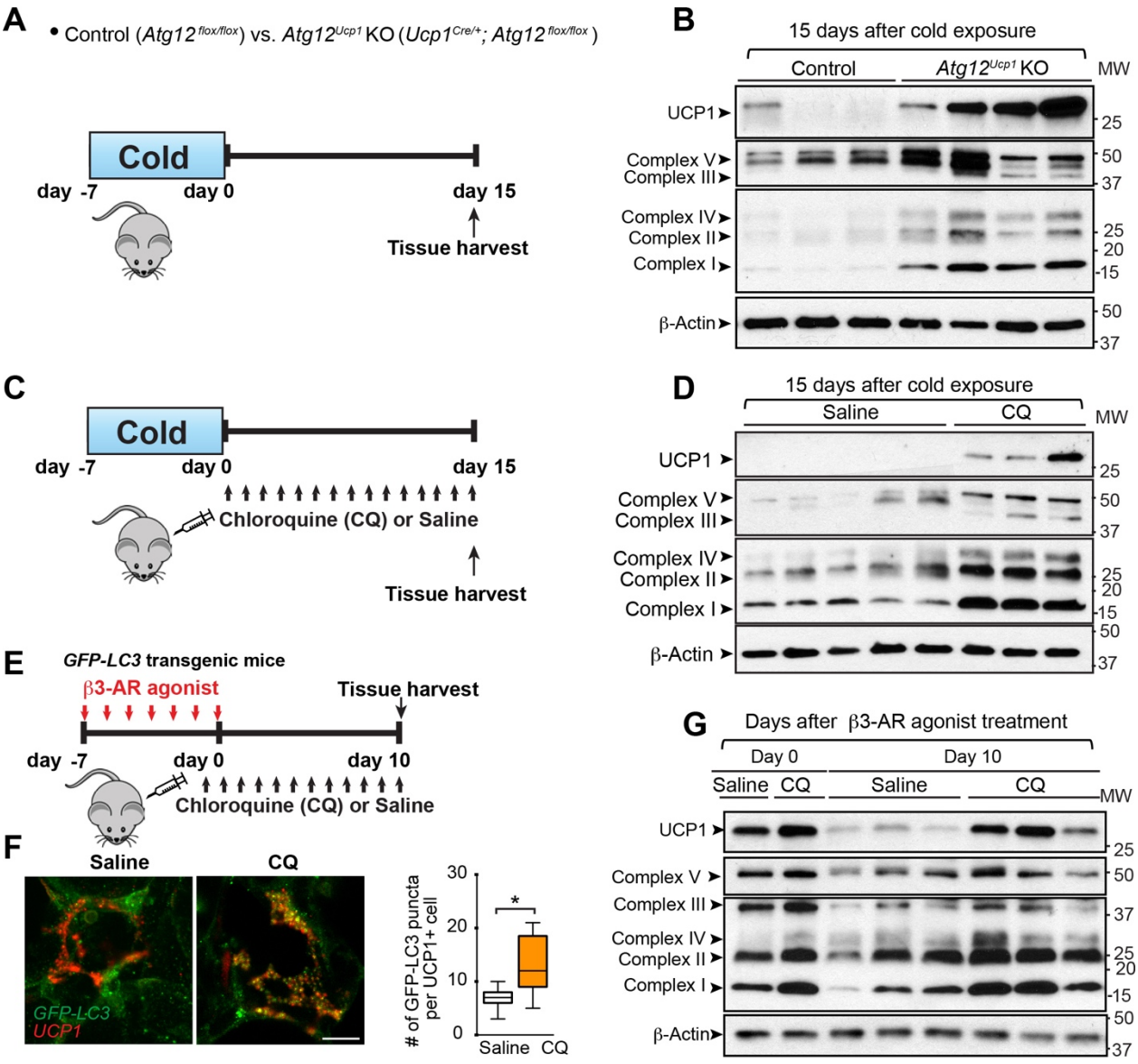

Supplementary Figure 11. Genetic and pharmacological inhibition of autophagy promotes beige adipocyte maintenance after withdrawal of external cues. (**A**) Schematic of the experiment in (B). Control (*Atg12*$^{flox/flox}$) and *Atg12*^{Ucp1} KO mice were housed at 6˚C for 5 days and subsequently kept at room temperature for 15 days. Inguinal WAT depots were harvested for molecular analysis. (**B**) Immunoblotting for UCP1 and mitochondrial complexes (as indicated) in the Inguinal WAT of control (*Atg12*$^{flox/flox}$) and *Atg12*^{Ucp1} KO (*Ucp1*$^{Cre/+;}$*Atg12*$^{flox/flox}$) mice at day 0 and day 15 after cold exposure. ß-actin was used as a loading control. Molecular weight (MW) is shown on the right. (**C**) Schematic of the experiment in (D). Wild-type mice were housed at 6˚C for 7 days and

subsequently kept under thermoneutrality (30˚C) for 15 days. During the re-warming period, the mice were treated with chloroquine at a dose of 60 mg kg^{-1} or saline. Inguinal WAT depots were harvested for molecular analysis. (**D**) Immunoblotting for UCP1 and mitochondrial complexes (as indicated) in the inguinal WAT depots of mice that were treated with saline or chloroquine during re-warming after cold exposure. *ß*-actin was used as a loading control. Molecular weight (MW) is shown on the right. (**E**) Schematic of the experiments in (F) and (G). *GFP-LC3* mice were treated with ß3-AR agonist for 7 days. Subsequently, the mice were treated with chloroquine (CQ) at a dose of 60 mg kg^{-1} or saline daily for 10 days following *ß*3-AR agonist withdrawal. Inguinal WAT depots were harvested for molecular analysis. (**F**) Confocal images of beige adipocytes from *GFP-LC3* mice after saline or chloroquine (CQ) treatment, as illustrated in (E). UCP1+ beige adipocytes and LC3 were visualized by immunohistochemistry for UCP1 (red) and GFP (green), respectively. (**G**) Immunoblotting for UCP1 and mitochondrial complexes (as indicated) in the Inguinal WAT of *LC3-GFP* mice treated with saline or chloroquine (CQ) daily for 10 days following *ß*3-AR agonist withdrawal. *ß*-actin was used as a loading control. Molecular weight (MW) is shown on the right.

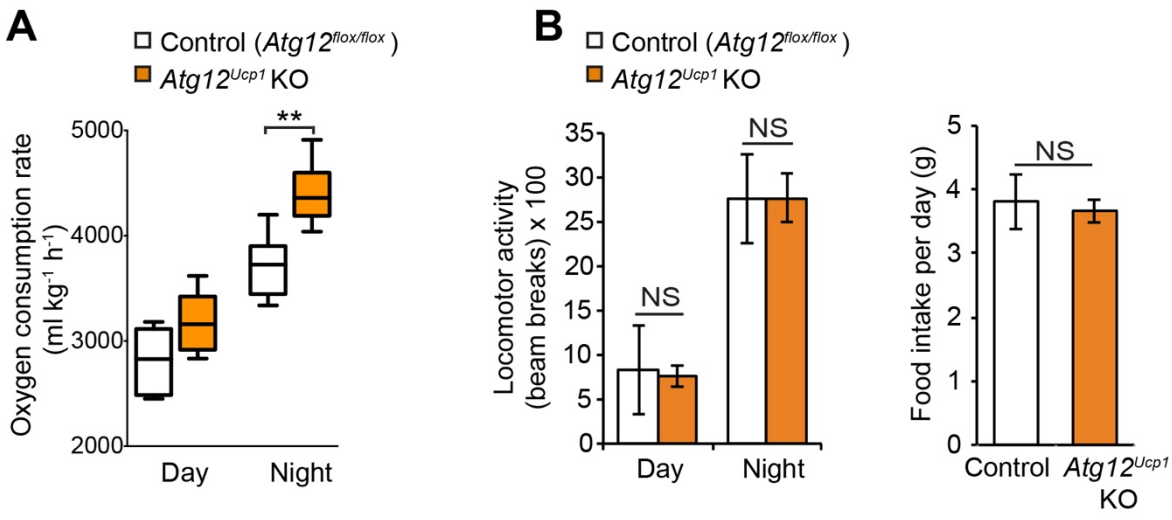

Supplementary Figure 12. Metabolic phenotype of *Atg12*^{Ucp1} KO mice.

(**A**) Quantification of whole-body oxygen consumption rate (VO2) of control (*Atg12*$^{flox/flox}$) and *Atg12*^{Ucp1} KO (*Ucp1*$^{Cre/+;}$*Atg12*$^{flox/flox}$) mice between 17-18 days after ß3-AR agonist withdrawal. VO_2 was measured using CLAMS during day and night time. Data are normalized to body weight and expressed as means ± s.e.m. ** *P* <0.01 by two-tailed Student's t-test. n = 6 per genotype. (**B**) Left, locomotor activity (beam breaks) in control (*Atg12*$^{flox/flox}$) and *Atg12*^{Ucp1} KO (*Ucp1*$^{Cre/+;}$*Atg12*$^{flox/flox}$) mice measured using CLAMS under a regular diet. n = 6. N.S., not significant. Right, food intake was measured in control and *Atg12*^{Ucp1} KO mice under a high-fat diet for 2.5 weeks. N.S., not significant. n = 6-7.

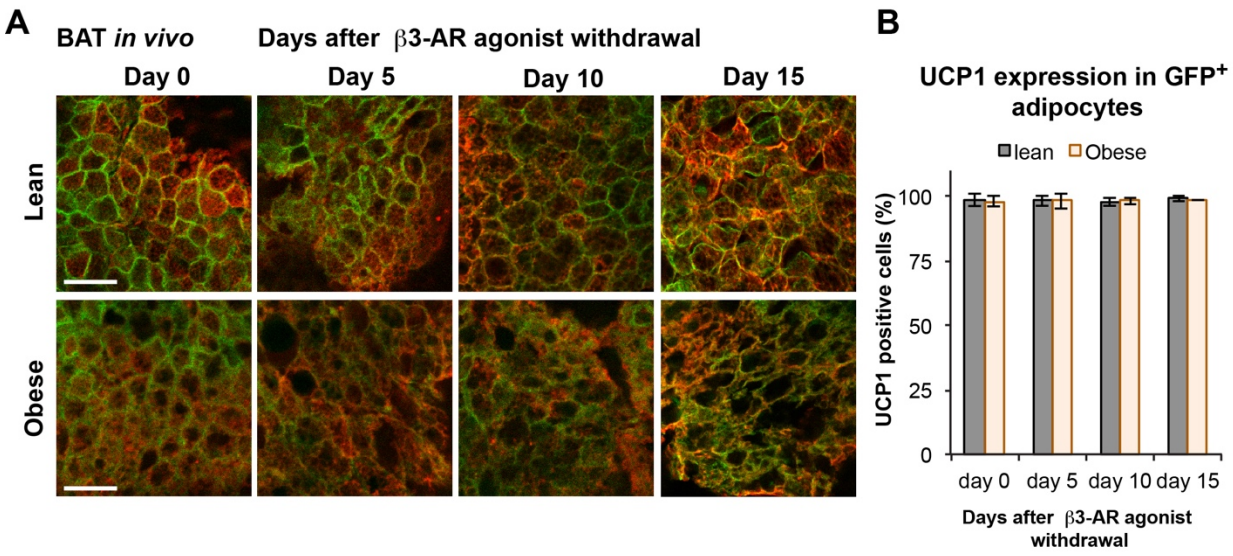

Supplementary Figure 13. Morphological analysis of classical brown adipocytes under obesity. (**A**) Confocal images of fixed interscapular BAT sections from *Ucp1*$^{Cre/+;}$*mT/mG* reporter mice under a regular diet (top panel, lean) and a high-fat diet (bottom panel, obese) for 12 – 16 weeks. Cellular membrane of brown adipocytes was visualized by membrane-targeted GFP (mGFP, Green). Endogenous UCP1 was mimmunostained (Red). Scale bar, 57μm. (**B**) Quantification of mGFP-positive adipocytes in lean and obese mice that express endogenous UCP1 in (A). n = 100 cells or more per group.

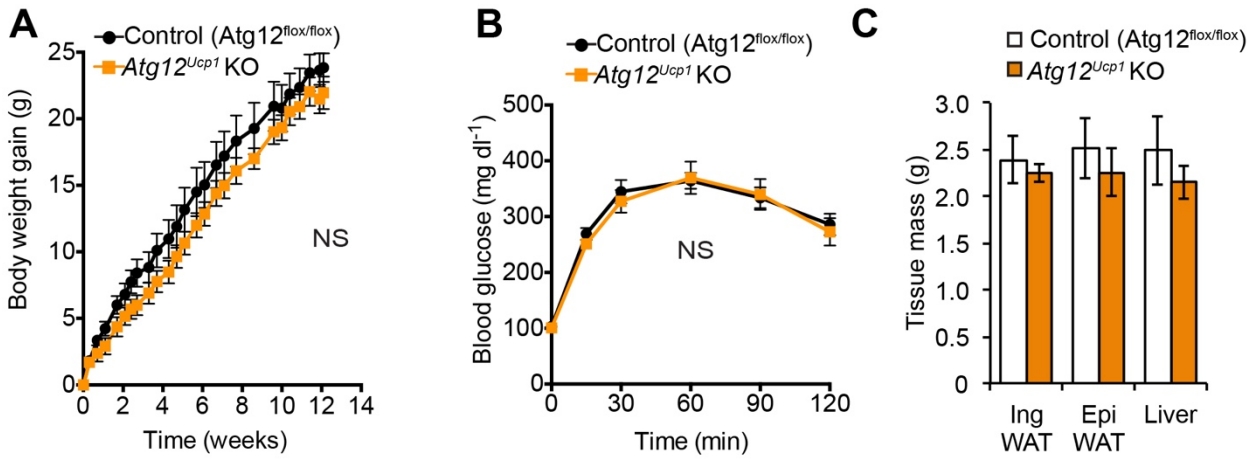

Supplementary Figure 14. Metabolic characterization of *Atg12*^{Ucp1} KO mice in the absence of β3-AR agonist treatment. (**A**) Body weight gain of control (*Atg12*$^{flox/flox}$) and *Atg12*^{Ucp1} KO mice under a high-fat diet without ß3-AR agonist treatment. Control and *Atg12*^{Ucp1} KO mice were fed a high-fat diet for 12 weeks. Body weight was measured twice a week. *n* = 6-7 per genotype. N.S., not significant. Data are expressed as means ± s.e.m. (**B**) After 12 weeks of high-fat diet, control and *Atg12*^{Ucp1} KO mice from (A) were fasted for 12 hours and injected with 1.5g kg^{-1} glucose. Whole-body glucose was measured at 15, 30, 60, 90, and 120 min. N.S., not significant. Data are expressed as means ± s.e.m. (**C**) Tissue weight of inguinal WAT, epididymal WAT, and liver from control and *Atg12*^{Ucp1} KO mice from (A). N.S., not significant. Data are expressed as means ± s.e.m

Table S1: Cluster 1 gene list and associated membership values

Gene ID	Value	Gene ID	Value	Gene ID	Value	Gene ID	Value	Gene ID	Value
Letmd1	0.999998	2310061I04	0.99993	Atp6v0a2	0.99979	Pafah2	0.99935	Sdhb	0.998799
Letm1	0.999993	Ndufb6	0.99993	Eci2	0.99979	Lclat1	0.99935	Fxc1	0.998791
Uqcrfs1	0.999992	Poldip2	0.99993	Rbck1	0.99978	Def8	0.99934	Rnf5	0.998782
Slc25a39	0.999991	Cox5b	0.99992	Sdhc	0.99978	Mrpl28	0.99933	Mfn2	0.998781
Reep6	0.999988	Car14	0.99992	Tnfrsf23	0.99978	Mpdu1	0.99931	Timm13	0.998771
Sla2	0.999985	Timm8b	0.99992	Ephx2	0.99978	Scarb2	0.99931	Gm6644	0.998765
Tmem147	0.999982	Rtn4ip1	0.99992	Sod2	0.99977	Slc52a2	0.99926	Cox7b	0.998748
Ciapin1	0.999982	Cox5a	0.99992	Tmem14c	0.99976	Hist1h1d	0.99925	Echs1	0.998739
Agpat3	0.999982	Ak1	0.99992	Mreg	0.99976	Abhd11	0.99925	Chchd3	0.998721
Cox10	0.999981	Yif1b	0.99992	Coasy	0.99974	Fbxw5	0.99924	Esrra	0.998703
2310042D1	0.999980	Fastk	0.99991	2610029I01	0.99973	Acadm	0.99923	Cenpa	0.998698
Mrpl37	0.999977	Cox17	0.99991	Cgrrf1	0.99971	Mrpl4	0.99922	Mtmr2	0.998687
Mlf2	0.999976	Lipt1	0.99991	Pnp	0.99971	Ndufa6	0.99922	Cox6b1	0.998667
Nmb	0.999975	Pgap2	0.99991	Prdx3	0.99971	1810014F1	0.99921	Ptcd3	0.998666
Ndufa8	0.999975	Mrps2	0.99991	Ndufs3	0.99971	Coq3	0.99921	Dph3	0.998661
D17Wsu92	0.999974	Mycbp	0.99990	Alas1	0.99970	Rnf10	0.99920	Ndufa3	0.998633
Cenpo	0.999972	Cpt1b	0.99990	Pigy	0.99970	Tsfm	0.99919	Rabif	0.998620
Crat	0.999972	Zadh2	0.99990	Ndufa5	0.99970	Coq6	0.99918	Ptrh2	0.998616
Lipa	0.999971	Mrps23	0.99990	Gfm1	0.99969	Clptm1	0.99917	Atp5a1	0.998614
Tbrg4	0.999970	Acsl5	0.99990	Gnao1	0.99968	Acsf2	0.99916	Agpat5	0.998597
2310061C1	0.999969	Ndufc1	0.99989	Prdx6	0.99968	Stxbp2	0.99916	Mrpl51	0.998591
Fam195a	0.999968	Poln	0.99989	Apoc2	0.99968	Mrpl35	0.99914	Pdzd9	0.998575
Crip2	0.999967	Hacl1	0.99988	Cisd1	0.99967	Comtd1	0.99914	Slc22a2	0.998545
Ppif	0.999966	Chchd2	0.99988	Cox7c	0.99967	Pisd	0.999130	BC004004	0.998526
Pla2g2e	0.999966	Pomgnt1	0.99988	Ndrg2	0.99966	Foxred1	0.999128	Uqcrq	0.998509
Car4	0.999965	Minos1	0.99988	Bola3	0.99965	Cox6b2	0.999122	Polrmt	0.998493
Hist1h1c	0.999965	1700021F0	0.99988	Cox8b	0.99965	Chrna2	0.999121	Tuba8	0.998485
Epb4.1l4b	0.999963	Pfkp	0.99987	Ifi27l1	0.99965	Atp5k	0.999114	Tmem110	0.998459
Cox7a1	0.999963	Arhgdig	0.99987	Fam82b	0.99965	Fbxo8	0.999109	Aph1a	0.998440
Mdh2	0.999962	Gnas	0.99987	Oplah	0.99965	Eci1	0.999108	Rai12	0.998426
Acot2	0.999957	Got1	0.99987	Cdc34	0.99960	Phb	0.999107	Macf1	0.998407
Atp6v0e	0.999955	Atp5j2	0.99986	Atp1b1	0.99960	Ndufs8	0.999092	Slc11a2	0.998388
Cat	0.999954	Mrps36	0.99986	Tfrc	0.99955	Ctsz	0.999085	Bcl3	0.998373
Dlst	0.999953	Smpdl3a	0.99986	Gm10012	0.99955	Ict1	0.999074	Hist2h3c2	0.998370
Pde4a	0.999951	C1qbp	0.99986	2300009A0	0.99954	Ndufb8	0.999072	Mtmr1	0.998356
Cpt2	0.999951	Cyc1	0.99985	Ccdc56	0.99954	Mrpl10	0.999070	Ogdh	0.998353
0610012G0	0.999947	Isca2	0.99985	Ndufa11	0.99953	Uqcrc2	0.999067	Tysnd1	0.998352
Khdrbs3	0.999946	Retsat	0.99985	2310039H0	0.99952	Cyhr1	0.999043	Ptger1	0.998349
Acaa1b	0.999944	Mrpl43	0.99985	Sdhd	0.99951	Des	0.999037	Tmem69	0.998345
Lamp1	0.999944	Amacr	0.99984	Acot8	0.99951	Atox1	0.999036	Ppcs	0.998335
Atp6v0b	0.999942	Sdr39u1	0.99984	Rpl39l	0.99948	Atp5d	0.999025	Nsun4	0.998331
Mars2	0.999942	1500032L2	0.99984	Ap1b1	0.99948	Traf4	0.999025	Rrm1	0.998318
Pop5	0.999942	Phb2	0.99984	Hist1h2be	0.99947	Pgm2	0.999018	Ctdnep1	0.998317
Cisd3	0.999940	Mrpl12	0.99983	Cyb5b	0.99947	Abcb8	0.999004	Dctn5	0.998315
Taco1	0.999939	Pgam1	0.99983	Slc25a33	0.99947	Atp5o	0.998990	Iscu	0.998290
Mrpl34	0.999939	Cs	0.99983	Mgll	0.99943	Mrps33	0.998928	Atp5sl	0.998268
Ndufv2	0.999939	Rbpms2	0.99982	Ralb	0.99942	Cox7a2l	0.998917	Gatad2a	0.998229
Oxa1l	0.999938	Mlycd	0.99982	Tpi1	0.99941	Ptpla	0.998915	Psmb5	0.998218
2010107E0	0.999938	Mrs2	0.99981	Hadha	0.99940	0610009O2	0.998902	Igsf21	0.998210
Mtch2	0.999938	S100b	0.99981	Mrps18b	0.99940	Hist2h3c1	0.998885	Pdxk	0.998192
Alpl	0.999937	Rap1gap	0.99981	Dhrs11	0.99939	Slc25a11	0.998865	Gars	0.998184
42622	0.999936	Slc25a20	0.99981	Pcyt2	0.99939	Grpel1	0.998860	Slmo2	0.998121
Adcy3	0.999934	Rhot2	0.99981	Ndufc2	0.99938	Hpdl	0.998851	Mrpl39	0.998110
Ndufv3	0.999933	Dnaja3	0.99980	Ecsit	0.99937	Grn	0.998843	Cyp2u1	0.998095
Txn2	0.999933	Ppdpf	0.99980	Fam108c	0.99937	Hist1h4h	0.998837	Gm561	0.998077
Hadh	0.999932	Cyp4b1	0.999791	Rundc3a	0.99936	Lpcat3	0.998815	Bsg	0.998077
Polrmt	0.991889	Dusp15	0.999789	Coq5	0.99935	Ndufb5	0.998808	Ndufb4	0.998064

Table S1: Cluster 1 gene list and associated membership values

Gene ID	Value [0,1]	Gene ID	Value [0,1]	Gene ID	Value [0,1]	Gene ID	Value [0,1]	Gene ID	Value [0,1]
Ndufs4	0.998029	Fabp3	0.996628	Endog	0.994713	Uqcr10	0.991615	Igfbp5	0.986295
Coq9	0.998011	Zfp961	0.996582	Mmaa	0.994683	Mrpl20	0.991351	Stard5	0.985945
Akr1b8	0.998003	2210016F1	0.996556	Ndufb7	0.994655	Fez2	0.991219	Nudt19	0.985784
Ankrd9	0.997985	Etfdh	0.996555	Ndufs7	0.994591	Mtx2	0.991136	2810002N0	0.985680
Tmem63b	0.997952	1110008J03	0.996456	Fam82a2	0.994560	Csrp2	0.991129	2310044G1	0.985625
Mtx1	0.997921	S1pr5	0.996455	2610507B1	0.994550	Dpy19l1	0.991080	Hist1h4i	0.985588
Dyrk1b	0.997899	Map2k2	0.996455	Pex19	0.994533	Eif1ad	0.991058	AV051173	0.985410
Fars2	0.997875	Gm16062	0.996431	Lrp10	0.994500	Nt5m	0.990878	Abcb6	0.985387
Atp1a1	0.997864	Prelid1	0.996411	Vdac1	0.994424	Gapdh	0.990799	Tmed5	0.985264
Stoml2	0.997861	C330006A1	0.996396	Pacsin2	0.994419	Tmem85	0.990717	Tmem55b	0.985119
2310030N0	0.997806	Myo18a	0.996391	9630033F2	0.994369	Sirt5	0.990704	Atp6v1d	0.985043
Ucp1	0.997786	Atpaf2	0.996372	Fgfr1op2	0.994337	Hist1h1e	0.990688	Abhd1	0.985019
Setd8	0.997726	Tomm5	0.996364	Car13	0.994311	Galt	0.990518	Gpd1	0.984678
Ndufs6	0.997704	Prkaca	0.996300	Rn45s	0.994165	Immt	0.990410	Mrpl46	0.984646
Mcat	0.997697	Tesk1	0.996248	1110058L19	0.994104	Cad	0.990326	Ptges2	0.984624
Ptdss2	0.997684	Akr1b10	0.996179	1110008P1	0.994102	2010106G0	0.990288	2810405K0	0.984386
Timm44	0.997679	Mrpl44	0.996178	Tcn2	0.994068	Usmg5	0.990277	Alkbh7	0.984222
Sco1	0.997646	Gfm2	0.996161	Pex10	0.994012	Ldhb	0.990076	Tpst2	0.984082
Timm10	0.997641	Dnajc19	0.996149	Chd3	0.993970	Atp5h	0.990065	Nqo2	0.984020
Lsmd1	0.997544	Pam16	0.996137	Ak3	0.993940	Glrx5	0.990004	Abcg2	0.983901
Fam132a	0.997496	B230208H1	0.996116	Bri3bp	0.993860	Atp5g2	0.989807	Psph	0.983887
Orai3	0.997471	Ifngr2	0.996033	Mrps18a	0.993859	Ensa	0.989796	Ctsd	0.983797
Rnf185	0.997460	Mrpl42	0.996015	Slc25a5	0.993850	Dock8	0.989360	9530008L1	0.983713
Gde1	0.997456	Cyp2b10	0.996008	Pla2g7	0.993803	Kctd12	0.989255	Aars2	0.983569
Fdx1	0.997453	Disp1	0.995991	1300001I01	0.993773	Pgk1	0.989217	Cib1	0.983478
Plin5	0.997444	Nsun3	0.995987	Cox7a2	0.993759	Fam36a	0.989192	Tmsb10	0.983457
Polr1d	0.997348	C030006K1	0.995925	Atp6v0c-ps	0.993734	Mtg1	0.989136	F2r	0.983421
Gpam	0.997340	Ndufb2	0.995868	Apoc1	0.993675	Aes	0.988724	Ppp2r5c	0.983413
Afg3l1	0.997318	Mrps27	0.995832	Trmu	0.993602	Grlf1	0.988622	Mecr	0.983404
Gipc1	0.997311	Ddt	0.995808	Tmem186	0.993495	Ndufa4	0.988374	Xpnpep3	0.983376
Gng2	0.997287	Slc35a4	0.995780	Usp10	0.993373	Mrps24	0.988345	Plcd1	0.983348
Gtf2h5	0.997257	A230051G1	0.995743	Uqcr11	0.993350	Wee1	0.988263	1110057K0	0.983297
Dnajc16	0.997233	Lgmn	0.995735	Ankrd13a	0.993258	Tmem189	0.988235	Fam86	0.983287
Rps6ka1	0.997213	Nr2f6	0.995681	Camsap3	0.993236	Nudt1	0.988203	Pmpca	0.983278
1110001J03	0.997155	Cuta	0.995672	Eif4e2	0.993135	9430016H0	0.988170	Pgp	0.983269
Tbl3	0.997144	Fam26f	0.995667	Gss	0.993085	Tufm	0.988143	Bcs1l	0.983198
Itfg3	0.997105	Hk1	0.995466	Acer3	0.993039	Mrpl36	0.988088	Dock5	0.983172
Decr1	0.997071	Chchd10	0.995383	1810013D1	0.992979	Commd3	0.988066	Adam12	0.982974
Hoxa4	0.997066	Gsk3a	0.995353	Galc	0.992875	As3mt	0.987978	AI462493	0.982941
Gypc	0.997048	Cds1	0.995317	Pmm2	0.992818	Ppm1l	0.987973	Psmg2	0.982841
Snrnp25	0.997036	Shmt1	0.995317	Ndufab1	0.992807	Creg1	0.987674	Mmp19	0.982769
Mrps21	0.997019	Ide	0.995309	Them4	0.992692	Eral1	0.987595	Rps11	0.982673
Pigq	0.997008	1110008F13	0.995277	Mrps5	0.992634	Cox11	0.987592	Mtif2	0.982646
Prkag1	0.996978	Uqcrc1	0.995268	Mrps7	0.992551	Hspa12b	0.987528	Pim1	0.982601
Tmem93	0.996977	Ociad2	0.995265	Lsm4	0.992372	Srxn1	0.987358	Tmlhe	0.982532
Mrps30	0.996951	Aldh3a2	0.995256	Rps27l	0.992328	Hspe1	0.987236	Acadl	0.982157
Higd1a	0.996899	Gatad1	0.995194	Tmem37	0.992307	Mark3	0.987222	Atp2a3	0.981971
Cox15	0.996898	Sdhaf1	0.995192	Mul1	0.992273	Afg3l2	0.987091	Ei24	0.981728
Fastkd5	0.996849	Tmem41a	0.995102	Tbc1d8	0.992267	Romo1	0.987074	Atp2a2	0.981663
Cox4i1	0.996840	Rab21	0.995077	Smpd1	0.992151	Atxn2	0.987045	Hsd17b4	0.981632
Brp44	0.996775	Sec14l1	0.995054	Plin3	0.991916	Gmnn	0.986963	Gm15471	0.981564
Otop1	0.996736	Ap1m1	0.995037	Fmo1	0.991829	Isca1	0.986928	Eif5a	0.981302
Dclre1b	0.996735	Ufsp2	0.995024	Hsdl2	0.991778	Arpc5l	0.986899	Car2	0.981132
Mrps16	0.996712	Uba1	0.995004	Psme1	0.991750	1700096K1	0.986758	Gns	0.980954
3110001D0	0.996670	Sidt2	0.994961	2400001E0	0.991748	Tmem9b	0.986714	Hist1h2bc	0.980780
Cops3	0.996667	Mrpl53	0.994844	Ech1	0.991704	Abcb10	0.986492	1300010F0	0.980757
Hibadh	0.996654	2410015M2	0.994822	Mrps12	0.991673	Mmachc	0.986387	Mrrf	0.980724

Table S1: Cluster 1 gene list and associated membership values

Gene ID	Value [0,1]	Gene ID	Value [0,1]	Gene ID	Value [0,1]	Gene ID	Value [0,1]	Gene ID	Value [0,1]
Txnrd2	0.980676	Tmem79	0.973628	Gng5	0.963936	Mtfr1	0.951471	Fdps	0.936795
Aco2	0.980370	Dnajc11	0.973557	Pigo	0.963894	Mrpl45	0.951338	Acad9	0.936666
Nat15	0.980368	Nfyc	0.972907	Elac2	0.963891	Nol3	0.951173	Abhd15	0.935962
Gpi1	0.980360	Acadvl	0.972848	Nhp2	0.963869	4921531C2	0.950824	Preb	0.935781
Asb8	0.980326	Uqcrb	0.972805	Hspa9	0.963454	Plxnd1	0.950759	Fabp5	0.935592
Keap1	0.980090	Gys2	0.972753	Psmb7	0.963354	Apeh	0.950258	Pwwp2b	0.934808
Gm15408	0.980061	Atp6v1e1	0.972163	Zfp385c	0.962791	Ccdc72	0.950115	Tmem198b	0.933909
Tmem53	0.980034	Ptcd2	0.971580	Hmg20b	0.962681	Apex2	0.949905	Tmem38b	0.933387
Yars2	0.979834	Gadd45gip	0.971504	Chid1	0.962543	Ptp4a3	0.949199	1700018L0	0.932986
Fastkd3	0.979739	Acox1	0.971333	1810063B0	0.962507	Fam162a	0.948634	1700008J0	0.932565
Dhrs1	0.979729	Cycs	0.971325	Timm17a	0.961898	Fam118b	0.948528	Hsd17b12	0.932257
Jagn1	0.979697	Senp3	0.971290	Mrpl30	0.961682	Traf3	0.948371	Mapkap1	0.932219
Trak1	0.979575	Ptcd1	0.971272	Dagla	0.961370	Wdr83	0.948237	Bet1l	0.932185
Ppic	0.979521	Ndufa9	0.971041	Itpr1	0.961296	Ttc32	0.947887	Aig1	0.931600
Tmbim4	0.979509	Pecr	0.970723	Hdhd3	0.961125	Tusc3	0.947671	AI846148	0.931545
Zdhhc13	0.979362	Sec14l4	0.970702	Pvrl2	0.960951	Iars	0.947416	Acot13	0.931499
Mcrs1	0.979308	Herc3	0.970319	Tmem8	0.960645	Nacc1	0.947134	4930453N2	0.931291
Ap3s1	0.979212	Rsad1	0.970260	Ppp1r3d	0.960461	Hmbs	0.946879	Fbxo44	0.931232
Rexo2	0.979079	Epas1	0.970101	Mrpl54	0.960457	Rsad2	0.946394	Cct3	0.930679
C030044B1	0.978999	Lmcd1	0.969902	Vac14	0.960304	Psmg3	0.946007	Suclg1	0.929639
Tmem177	0.978748	Osbpl2	0.969643	Tmem208	0.959935	Cdc14a	0.945804	Ldlrap1	0.929637
Bnip1	0.978437	Acy3	0.969611	Tmem88	0.959833	Ccnd1	0.945567	Usp8	0.929330
Cox6a1	0.978250	4930471M2	0.969447	Slc25a34	0.959809	Mrp63	0.945429	Rtn3	0.928454
Tsc22d1	0.978156	Plxna1	0.968893	Ddah1	0.959621	Dlat	0.945336	Opa3	0.928050
Vps33a	0.977916	Ndn	0.968887	Exosc4	0.958978	Slc25a42	0.945087	Pwp2	0.927890
Plbd1	0.977913	Cd1d1	0.968713	Mavs	0.958879	Pxmp4	0.944656	Higd2a	0.927837
Atp5f1	0.977798	Epor	0.968551	Prdx5	0.958719	9030619P0	0.944460	Aldh9a1	0.927737
Rcor2	0.977574	Ndst1	0.968375	Prcp	0.958433	Tha1	0.944302	D330012F2	0.927681
Il2rg	0.976936	Arpp19	0.968316	X99384	0.958409	Pop7	0.944141	Adra1a	0.927162
Lsm11	0.976930	Dpy30	0.968022	Dcaf12	0.958355	Wsb2	0.944116	N6amt2	0.926724
Sike1	0.976923	Sepsecs	0.968005	1810035L1	0.958059	Spryd4	0.944093	Rpl7l1	0.926562
Dhrs4	0.976794	4833439L1	0.967947	Cbr1	0.957921	Sgcb	0.943858	Ces1d	0.925899
Tusc1	0.976538	2310008H0	0.967919	Avpi1	0.957854	Zfp706	0.943788	Usp2	0.925578
Mrps10	0.976507	Ndufb9	0.967469	G630090E	0.957610	Ttc39b	0.943545	Apobr	0.925018
Kras	0.976413	Sh3bgrl	0.967415	Il1r1	0.957379	Fam108b	0.943307	Gpn2	0.924676
Slc25a22	0.975996	Mrpl19	0.967391	Mtif3	0.957234	Tmem183a	0.943158	Sars2	0.924525
Lsm2	0.975931	Txndc11	0.967343	8430427H1	0.957079	4921524J1	0.943091	Mcart1	0.924285
Ccdc51	0.975765	Apoo	0.967111	Orai1	0.956900	Pebp1	0.942863	Acaa2	0.923830
Hyal1	0.975236	Rfk	0.967041	Lrpprc	0.956880	Qrich1	0.942670	Raph1	0.923635
Fdxacb1	0.975000	42434	0.966715	Rab12	0.956732	Klhdc10	0.942649	Fdx1l	0.923483
Sepx1	0.974893	Xrcc3	0.966673	Ccdc28b	0.956357	Bckdk	0.941807	Tpcn1	0.923335
Hagh	0.974790	Med16	0.966286	Alkbh3	0.955940	Map2k4	0.941792	Myo5b	0.922599
Sssca1	0.974756	Trappc1	0.966021	Yaf2	0.955389	Garnl3	0.940877	Rcc1	0.922292
Myo19	0.974734	Ssr2	0.965944	Srl	0.955364	Mettl11a	0.940570	Arxes1	0.921792
Elovl3	0.974705	Col12a1	0.965800	Uqcc	0.954633	Rmnd1	0.940060	Apln	0.921741
Mrps11	0.974668	Rab3a	0.965659	Ndufb11	0.954291	Pcbd2	0.939918	Acsf3	0.921614
Emcn	0.974543	Mrpl3	0.965624	Asna1	0.954057	Phlpp1	0.939761	Slc25a44	0.921406
Tuba4a	0.974528	Mmgt1	0.965347	Nav2	0.953962	Sirt3	0.938330	Map2k6	0.921365
Brd3	0.974497	Trp53inp2	0.964905	Gpaa1	0.952985	Mprip	0.937945	Pofut2	0.921188
Dag1	0.974380	Manf	0.964775	Iars2	0.952723	Stap2	0.937879	Triap1	0.920918
Csnk2b	0.974351	Inpp5e	0.964729	Abcd3	0.952703	Arf1	0.937684	1110002L0	0.920458
Oxnad1	0.974276	Nhej1	0.964671	Kdm5c	0.952682	S100a13	0.937410	Pycrl	0.920374
Gpr137	0.974263	Dusp22	0.964638	Dus1l	0.952650	5031439G0	0.937340	Oxsm	0.920053
Stradb	0.974235	Vcam1	0.964219	Lmf1	0.952426	Mtm1	0.937115	A530050N0	0.919948
Ube2l3	0.974148	Agpat1	0.964144	Cdh13	0.952264	Tbl1xr1	0.937072	Sar1b	0.919857
Fam54b	0.973985	Nit2	0.964079	Aldh3b2	0.951841	Adssl1	0.937013	Fh1	0.919660
Lace1	0.973976	Myl6b	0.964017	Abhd6	0.951506	Gyk	0.936844	Ran	0.918958

Table S1: Cluster 1 gene list and associated membership values

Gene ID	Value [0,1]	Gene ID	Value [0,1]	Gene ID	Value [0,1]	Gene ID	Value [0,1]	Gene ID	Value [0,1]
Pcca	0.918658	Tspan31	0.901449	Clpp	0.878438	Dnmt3a	0.853182	Edf1	0.822535
Ptk2b	0.918569	6430706D2	0.900182	St6gal1	0.877827	Acacb	0.852976	Psme2	0.821186
Nr1h3	0.918433	A430005L1	0.900089	Urod	0.877567	Ubqln4	0.852284	Gmpr	0.820843
Ankrd28	0.918385	Ttc7	0.899869	Snrpf	0.877508	Dynll1	0.851524	Mapre3	0.819932
Aifm1	0.918181	Ppp2r2a	0.899741	Gatc	0.877368	Ticam1	0.851207	Ets1	0.819041
Prkcsh	0.916572	Shroom4	0.899657	H1f0	0.877015	Ado	0.850827	Gimap4	0.818942
Gm14403	0.915707	Ndufs2	0.899568	Tmem135	0.876926	Spred1	0.850717	Spsb1	0.818384
Hspd1	0.915542	2310069B0	0.899134	Aurkaip1	0.876522	Gm14057	0.850628	Hus1	0.817365
Pgam5	0.915329	Mrpl38	0.898875	Dgat2	0.875721	Mff	0.850436	Zcchc3	0.817315
Cox16	0.915222	Mpp6	0.898774	Macrod2	0.875338	Pdk2	0.849942	Txnrd1	0.816253
Sema4a	0.914964	Pllp	0.898755	D4Ertd22e	0.874988	Xpnpep1	0.849344	Tmem70	0.815980
Vars2	0.914757	Esrrg	0.898436	Mab21l2	0.874739	Diablo	0.848978	Wipi2	0.815413
Cib2	0.914685	Hpgd	0.898327	Mapk14	0.874536	Pex5	0.848692	Eaf1	0.815331
Slc7a8	0.914663	Xrcc6bp1	0.898287	Tmem222	0.874444	Phf5a	0.846483	2810432L1	0.814564
Med1	0.913528	Dad1	0.897909	Nus1	0.874409	Tax1bp3	0.846167	Ldha	0.814241
Ethe1	0.912837	Adck3	0.897706	Smtnl2	0.873996	Vkorc1l1	0.845149	Trmt2b	0.813714
Akt1	0.911849	Sfxn5	0.897487	Dennd5a	0.873819	Gm5069	0.84506	1700052K1	0.812991
Hif1a	0.911352	Pgls	0.897021	Bcl2l1	0.873633	Chchd1	0.843808	Prkar2a	0.812103
Rab3ip	0.910908	Ube2a	0.896523	N4bp2	0.873204	2700089E2	0.843058	Adap2	0.811802
Mtor	0.910279	Gsto1	0.896456	Thoc6	0.872945	1190007I07	0.842748	Mid1ip1	0.811360
Mlx	0.909891	Tubb4b	0.896223	1500001M2	0.872605	Serpinf1	0.842589	1810012P1	0.809981
Llgl2	0.909722	Sco2	0.896156	Bbip1	0.872569	Wdfy2	0.842475	Coq7	0.809162
Nrm	0.909380	Polr2i	0.895045	Mrps22	0.872560	Sec61g	0.842377	Ltbr	0.808756
Adam17	0.909315	Pole4	0.894873	Pik3c2a	0.871783	Nadk	0.841368	Limd1	0.808350
Lrrfip1	0.908957	Timm50	0.894704	Fam108a	0.871205	Mrpl27	0.83849	Qdpr	0.808073
Ypel2	0.908835	Btbd6	0.894479	2900064A1	0.870693	Gramd3	0.837971	Mrpl32	0.807851
Fxn	0.908806	Tmem150a	0.894398	Atp5l	0.870667	Cnst	0.837394	Slc22a5	0.807384
Fbxl6	0.908263	Cidea	0.893437	Uqcrh	0.870206	BC003965	0.83712	Rad23a	0.806907
Smcr7	0.908140	Lrrc20	0.893371	Lrrc57	0.869958	Fam173b	0.837019	Mrpl14	0.806586
Gm10094	0.907729	C1rl	0.892412	Dck	0.868803	Acot1	0.836728	Alg14	0.806468
Mid2	0.907686	Capza1	0.891299	Glrx3	0.868512	Haus3	0.836155	Kdr	0.806152
Mrpl41	0.907612	Pdss1	0.890674	Aldoa	0.868057	Deb1	0.835733	Zfp710	0.805850
Eif3l	0.907550	Trak2	0.890548	Rap2a	0.866374	D8Ertd738e	0.834745	D2Wsu81e	0.805132
4931428F0	0.907409	Arhgap26	0.888711	Ralgapb	0.866297	Adal	0.834408	Pkm2	0.804493
Gng11	0.907356	Dhrsx	0.888701	4930506M0	0.865387	Zfp52	0.833594	Trappc2l	0.803028
Hadhb	0.907119	Nptn	0.888472	Ube2d3	0.864999	Ehd1	0.833039	Rasl2-9-ps	0.802714
Rwdd2b	0.906852	H2-Ke2	0.888383	Idh3a	0.863432	Sh3bp5l	0.832982	Mpv17l2	0.802310
Syngr1	0.906836	Atf5	0.888345	Fbp2	0.863343	Narfl	0.832918	Ghitm	0.801591
Etfb	0.906127	1700012D0	0.887379	Snx22	0.86334	Ghdc	0.832741	Gna13	0.801300
Cpt1a	0.906027	Psmb3	0.887278	Pstk	0.86324	4930455C2	0.832241	Qk	0.799643
Ube2f	0.904962	Prkab1	0.885868	P2rx5	0.86304	Sorl1	0.832221	Dhcr24	0.798743
Frrs1	0.904892	Cpn2	0.885553	Itga6	0.86197	Pcbp1	0.832095	Ccdc107	0.798303
Memo1	0.904732	Rnf7	0.885436	Acyp2	0.86183	Psmb2	0.831492	Mdm2	0.798148
1110007C0	0.904647	Sgpl1	0.885022	Yars	0.86178	Fem1a	0.831129	Mterfd2	0.798109
Gt(ROSA)2	0.904572	Cln8	0.884046	Ubac2	0.86155	Ifi30	0.831074	1700123O2	0.797988
1110002B0	0.904344	Ube3c	0.883987	Nutf2	0.86132	Ippk	0.830596	Tspan15	0.797941
Ccdc122	0.904334	Shb	0.883518	Atp5e	0.85991	Narf	0.830459	2410002I01	0.797887
2410003K1	0.904307	B430212C0	0.883289	Marcks	0.85963	Tfr2	0.830229	Pfkl	0.797527
Ubiad1	0.904177	Flad1	0.883253	Cstb	0.85926	Ccnyl1	0.829638	Smcr7l	0.795767
Tm4sf1	0.904001	Ptpmt1	0.883101	Pitpna	0.85924	Gm6484	0.827541	Gm2382	0.794640
Rcl1	0.903597	Mrps34	0.883027	Wars	0.85581	Ppp4r1	0.826989	Nop10	0.793886
Uhmk1	0.903544	Med8	0.881469	Rnls	0.85557	Pdf	0.82625	Slc35d1	0.791447
Sft2d1	0.903293	Cln3	0.880299	Dcaf10	0.85492	Ndufa12	0.825399	Hipk1	0.791341
Fam171a1	0.902530	Banf1	0.880231	Agxt2l2	0.85486	Slc25a15	0.824429	Ndfip2	0.790598
Dera	0.902470	2310003C2	0.880162	1700066M	0.85444	Serinc5	0.824374	Anapc7	0.789883
Tsku	0.902012	Nedd8	0.880020	Nipsnap3b	0.85396	Ppp1r3b	0.823809	Mrpl40	0.789835
Pfkm	0.901662	5730437N0	0.879975	Lamp2	0.85359	Asns	0.822629	Psap	0.787643

Table S1: Cluster 1 gene list and associated membership values

Gene ID	Value [0,1]	Gene ID	Value [0,1]	Gene ID	Value [0,1]	Gene ID	Value [0,1]	Gene ID	Value [0,1]
Cops7a	0.787550	Emg1	0.745594	Arl5a	0.695294	Mrpl9	0.654977	Kpnb1	0.604447
Ece2	0.786824	Abhd12	0.745514	Nid2	0.693924	Prdm10	0.652486	Tspan13	0.604343
Jmjd7	0.786655	Sdha	0.744945	Aprt	0.693752	Phka1	0.652348	Acbd6	0.603326
Pdcd4	0.786426	Tmem126a	0.743852	Usp20	0.692750	Snrpe	0.651928	Fnbp1l	0.603318
Glul	0.786181	Nt5dc1	0.743673	Aspg	0.692663	Mfsd9	0.650972	Chmp1a	0.601309
Dynll2	0.785655	Pak1ip1	0.743432	Tmem33	0.692355	Crlf3	0.649224	Ppa2	0.601095
Nme1	0.785461	Ppp1r14b	0.743377	Hddc2	0.691727	Naprt1	0.647818	Ccdc32	0.600458
Rhoc	0.785443	Rcan3	0.741071	Wars2	0.691038	Harbi1	0.646542	Purb	0.600273
2900010M2	0.782146	Mettl17	0.738389	St6galnac6	0.690822	Cdca7l	0.64597	Magt1	0.600226
Adam19	0.781637	Mdh1	0.737963	Arl8b	0.690668	Tecpr1	0.644931	Paqr9	0.600009
Sdccag3	0.779541	1810046J1	0.737871	Psme3	0.690001	Chchd7	0.644842	Fam120a	0.599796
Speg	0.779204	Cd200	0.737352	Slc35b1	0.689329	Tfb2m	0.644394	Jazf1	0.599641
Tbc1d22a	0.778506	Ifrd2	0.736884	Slc30a9	0.689094	Uxt	0.644229	Tinag	0.599027
Adap1	0.778322	Rhoa	0.736734	Urgcp	0.688841	Psmc4	0.643653	Pip4k2c	0.598628
Timm8a1	0.777702	Ttc25	0.736349	Ppp1cc	0.688541	Sfmbt1	0.642628	2010315B0	0.597760
Cope	0.776152	Rmnd5b	0.736228	E2f2	0.687369	Cox6c	0.641124	Acad8	0.597355
Cox18	0.774096	Kbtbd4	0.732672	Aup1	0.686968	2310003F1	0.641108	Smyd2	0.597285
Tmem97	0.773607	Gpr160	0.731710	Imp3	0.686771	Fkbp4	0.640466	Rnmtl1	0.596789
Coro1b	0.772389	Ndufv1	0.731471	Suclg2	0.686531	Trabd	0.638584	Fam176b	0.596631
Tbc1d20	0.771911	Sap30	0.731323	Grb2	0.685891	Erlec1	0.638085	Ak2	0.596390
Add3	0.770735	Pgd	0.731308	Prpf4	0.685381	Lpin2	0.636758	Otud6b	0.595275
Slc38a2	0.770156	Mtap	0.729973	Fbxo9	0.685169	Cideb	0.635189	Nolc1	0.592200
Foxn3	0.769684	Chkb	0.729322	Zfp770	0.684872	Fam158a	0.634575	Cdc42se2	0.592051
Chek2	0.768985	Ash2l	0.729276	9030224M1	0.683779	Oaz1-ps	0.632296	Hsd17b7	0.591147
Dynlt1b	0.768594	Tmem60	0.729012	Rilp	0.682882	Abcb7	0.631188	AI317395	0.590130
Gm12070	0.768275	Coq10b	0.728378	Stk40	0.681157	Wdr8	0.630876	Fibp	0.590118
Atp6v1a	0.767134	Lss	0.728016	Samm50	0.679390	Prdx2	0.630868	Rhod	0.588205
Lpl	0.766940	Hlf	0.723801	Tmem65	0.678780	Tfdp1	0.630253	Pex14	0.586722
St5	0.765706	Prep	0.722129	Rab22a	0.677073	Elp4	0.630225	Mkks	0.585936
Pde7b	0.765482	Aplnr	0.721662	Cd38	0.676089	Naa30	0.630034	Srpr	0.584938
Hfe	0.764811	Tbc1d25	0.720845	Aktip	0.675418	Gabarapl2	0.629997	B330016D1	0.584433
Mrps17	0.763766	Ppp1r3c	0.718409	Mfap3l	0.675004	Slc2a4	0.629928	Csrnp2	0.583042
H13	0.762264	Mrpl13	0.717476	Megf9	0.673654	Ppp6r1	0.627522	Map2k5	0.581898
Csnk2a1	0.758551	Mrto4	0.716260	Fv1	0.673307	Mrps28	0.627161	Nanp	0.581645
Wdr73	0.758363	Tagln2	0.714813	St3gal5	0.671777	Icam2	0.625787	Cab39	0.579227
Sytl4	0.757992	Atad3a	0.714582	Cks2	0.671503	Cux1	0.624417	Fam105b	0.579058
Sh3bp5	0.756508	Tpcn2	0.714153	Plekha8	0.670197	Echdc3	0.620502	Ctbp1	0.578257
Vps13c	0.754884	Slc31a1	0.713474	Dap3	0.669901	Elof1	0.620044	Rpl36al	0.578196
2810025M1	0.752742	Mgrn1	0.713324	Tomm40	0.66922	Ckb	0.618638	Surf4	0.577201
Agk	0.752402	Snrpd3	0.712801	Btbd1	0.66826	Ttl	0.618589	2310009A0	0.575907
Tirap	0.751155	Tomm22	0.712658	Fam175a	0.66735	Gpd2	0.617905	Snx15	0.575633
Clstn3	0.749957	Ndufb3	0.712634	Supv3l1	0.66626	Sh2b2	0.617706	Akr1c13	0.575225
A730020M(	0.749775	Impa2	0.712445	Msra	0.66429	Spata2	0.617322	Cldn12	0.574352
Uba52	0.749633	Cd34	0.711719	Usp12	0.66404	Ruvbl2	0.61683	Stk16	0.573127
Tceb1	0.749447	1700037H0	0.711500	Ndufa13	0.66398	Bmi1	0.616489	4833442J1	0.570953
Fam116a	0.749193	Derl1	0.711461	Cbx4	0.66316	AI987944	0.616477	Dnajc25	0.570770
Cxcl12	0.748415	B3gat3	0.710655	Zdhhc5	0.66248	Ninj1	0.61551	Zfp54	0.568199
Tgfb1	0.747910	Pde4d	0.708953	Mob1b	0.66205	Polh	0.614049	Tmem5	0.567071
Mrps35	0.747892	Clec16a	0.707893	Fahd1	0.66038	Ddo	0.612869	Hras1	0.566957
Itpkb	0.747784	Gprc5b	0.704245	Grpel2	0.66014	Kri1	0.612716	Hemk1	0.565272
Ube2j2	0.747757	AK010878	0.700802	Myeov2	0.66006	Fut8	0.612074	3110002H1	0.564819
Stx6	0.746998	Fgl1	0.700448	Slc43a2	0.65984	Nudt14	0.611038	Timm9	0.564777
Lcmt2	0.746933	Lamtor2	0.698521	Adamts9	0.65903	Ddx47	0.60861	Gcnt2	0.564033
Rtel1	0.746785	Tmem66	0.697725	Cpped1	0.65879	Lyrm5	0.607985	Gtpbp8	0.562430
Mrpl17	0.746455	1110002N2	0.697677	Homer1	0.65850	Sh3bgrl2	0.606522	Csnk1g3	0.561299
Ankrd40	0.746374	Lhfp	0.696239	Ccbl2	0.65757	Lman2	0.605779	Psme4	0.561008
Golph3	0.746292	Ube3b	0.695817	Tmem167	0.65547	Yif1a	0.604576	Coq10a	0.560785

Table S1: Cluster 1 gene list and associated membership values

Gene ID	Value	Gene ID	Value	Gene ID	Value	Gene ID	Value	Gene ID	Value
Cdc45	0.560190	1810049H1	0.52603						
Dnajc28	0.559664	Cdk17	0.52603						
2810422J0	0.558343	Slc9a3r1	0.52573						
4930470H1	0.557862	Thyn1	0.52480						
2410017P0	0.556503	Ccbl1	0.52377						
Agl	0.556037	Slc39a10	0.52158						
Scyl1	0.555818	Cfl2	0.51928						
Ap4b1	0.555657	Ap1s1	0.51898						
Entpd5	0.555467	Mafb	0.51882						
Wdr41	0.555424	Fn3k	0.51757						
Mrps26	0.554561	Rnft1	0.51751						
Gprin3	0.552455	Ubac1	0.51729						
Ap4e1	0.551610	Prkaa2	0.51654						
BC028528	0.551182	Fam168b	0.51549						
Commd1	0.550872	Rce1	0.51469						
Imp4	0.550630	Jtb	0.51454						
Aldh5a1	0.550518	Uggt2	0.51401						
Timm23	0.550482	Alg3	0.51327						
Atp13a1	0.549681	Slc36a1	0.51234						
Cyyr1	0.549594	Rab7	0.51115						
Tmem38a	0.549431	Nmt2	0.51037						
E130309D(	0.549118	Zfyve21	0.50997						
Tkt	0.549002	Nutf2-ps1	0.50935						
Egln1	0.548834	Arpc3	0.50750						
Atp6v1b2	0.548818	Atg4d	0.50605						
Fancf	0.548459	Ndufa2	0.50554						
Nek9	0.548363	Odc1	0.50524						
Nadsyn1	0.547677	Tm6sf1	0.50452						
Ccng1	0.547364	Arfgef2	0.50306						
Mall	0.546633	Ociad1	0.50214						
Parp16	0.545477	Mrpl33	0.50184						
Nol9	0.545041	Nprl3	0.50128						
Alad	0.543683	Dus4l	0.50078						
Fzd8	0.543288								
Tex264	0.543012								
Pcyt1a	0.542836								
Rasgrp3	0.541139								
Sertad3	0.540792								
Dcaf4	0.540239								
Glrx	0.539927								
Ppm1f	0.537946								
Sh3gl1	0.536396								
Ddx39	0.536253								
Pla2g12a	0.535834								
Ccdc109a	0.535792								
Fam175b	0.535326								
Snupn	0.535233								
Tubg1	0.535197								
Ogfod2	0.533456								
Dip2a	0.533316								
Pde4b	0.531192								
Hif1an	0.530865								
Tnfrsf22	0.530769								
Ugp2	0.529619								
Mical2	0.529331								
Tpp2	0.529003								
Atp1b3	0.528066								
Ino80c	0.527644								

Supplementary Table 2. qRT-PCR primers

Gene Name	Forward (5' to 3')	Reverse (5' to 3')
Ahnak	ACACTGTTGGCTTGAAGTTGC	CTGGGCCATCATGCAGATTGT
Atg12	TGTGAATCAGTCCTTTGCCCC	TGCAGGACCAGTTTACCATCAC
Atg4c	GCATCCGGATTTGCAAGGGC	CTCCAGCTGTCACGGAGTCA
Atg5	ATGCGGTTGAGGCTCACTTTA	GGTTGATGGCCCAAAACTGG
Atp6	TGGCATTAGCAGTCCGGCTT	ATGGTAGCTGTTGGTGGGCT
Atp8	TTCCCACTGGCACCTTCACC	TGTTGGGGTAATGAATGAGGCAA
Bnip3	TCCTGGGTAGAACTGCACTTC	GCTGGGCATCCAACAGTATTT
Bnip3l	TGTCTCACTTAGTCGAGCCGC	TGGGTAGCTCCACCCAGGAA
Cidea	ATCACAACTGGCCTGGTTACG	TACTACCCGGTGTCCATTTCT
Cln3	CCCTCGGTTGGATAGTCGGA	GCCTGGTTCCACATGGCTC
Cox1	TAGCCCATGCAGGAGCATCA	TGGCTGGGGGTTTCATGTTGA
Cox2	ACCTGGTGAACTACGACTGCT	CCTAGGGAGGGGACTGCTCA
Cox3	CTTCACCATCCTCCAAGCTTCA	AGTCCATGGAATCCAGTAGCCAT
Cox4i1	GCCTGATTGGCAAGAGAGCC	CAAGGGGTAGTCACGCCGAT
Cox7a	CAGCGTCATGGTCAGTCTGT	AGAAAACCGTGTGGCAGAGA
Cox8b	GAACCATGAAGCCAACGACT	GCGAAGTTCACAGTGGTTCC
Ctns	ATGAGGAGGAATTGGCTGCTT	ACGTTGGTTGAACTGCCATTTT
Ctsa	CAGCCCTCTTTCCGGCAATA	TTTGGGTCGTTCTGCGACTC
Ctsc	TGCCACATCTGAGGAACAAA	CACCAGGACTCCTCTGCATT
Ctsc	TGCCACATCTGAGGAACAAA	CACCAGGACTCCTCTGCATT
Ctsd	GCTTCCGGTCTTTGACAACCT	CACCAAGCATTAGTTCTCCTCC
Cytb	CCTTCATGTCGGACGAGGCTT	TGCTGTGGCTATGACTGCGAA
Dio2	CAGTGTGGTGCACGTCTCCAATC	TGAACCAAAGTTGACCACCAG
Elovl3	TCCGCGTTCTCATGTAGGTCT	GGACCTGATGCAACCCTATGA
Foxo3	AACGGCTCACTTTGTCCCAGA	ACAGGTTGTGCCGGATGGAG
Gm2a	ACTGCTCCTCAGAAGGTGGA	CTTCCTTGAAGGGACAGTGG
Hexb	CTCTTTCGGGACTTTCACCA	CCATGGCATCCAGAGTTTTT
Mcoln1	CTGACCCCCAATCCTGGGTAT	GGCCCGGAACTTGTCACAT
Mitf	AAGTCGGGGAGGAGTTTCACG	GGAGCTTAACGGAGGCTTGGA
Naga	AGAGAACGTGCAGAGGGGTA	TGGACAGCACACTCTTCCAG
Nd2	GCCTGGAATTCAGCCTACTAGC	GGCTGTTGCTTGTGTGACGA
Nd4	CGCCTACTCCTCAGTTAGCCA	TGATGTGAGGCCATGTGCGA
Pgc1a	AGCCGTGACCACTGACAACGAG	GCTGCATGGTTCTGAGTGCTAAG
Sqstm1	ATGTGGAACATGGAGGGAAGA	GGAGTTCACCTGTAGATGGGT
Tfam	CCTTCGATTTTCCACAGAACA	GCTCACAGCTTCTTTGTATGCTT
Ucp1	CACCTTCCCGCTGGACACT	CCCTAGGACACCTTTATACCTAATGG
Ulk2	AGCTTCAGCATGAAAACATCGT	CGATTGGCATAAGACAACAGGA
Uvrag	GACTTTGGAATAATGCCGGATCG	CAGCCCATCCAGGTAGACTTT
Wipi1	GCGCTCCGAGGGGAAGTTAT	CCCTTCTGACTTCCACGGCA

Chapter 3: Conclusions and future directions

Summary

Our study reveals an important role for autophagy in degrading mitochondria during beige adipocyte conversion to white following withdrawal of external cue. Inhibition of autophagy leads retention of beige adipocytes and prevents from diet-induced obesity.

Our data strongly suggests that selective mitophagy takes place during beige-to-white adipocyte conversion. During conversion, we observe colocalization of mitochondria-localized protein TOM20 with GFP-LC3; analyzed in conjunction with mitochondria-autophagosome structures observed by electron microscopy, as well as changes mitochondrial content. Future studies should address selective mitochondrial degradation using more direct tools, such as mt-Keima transgenic mouse system (Sun et al., 2015).

Beige adipocyte development has been implicated in disease state such as obesity. It is likely that dysregulation of the beige adipocyte maintenance contributes to the development of obesity: diet-induced obesity increases the rate of beige adipocyte conversion to white adipocytes following β3-AR agonist withdrawal. Genetic deletion of *Atg12* or *Atg5* specifically in UCP1+ adipocytes, i.e., mature brown and beige adipocytes, substantially prolongs the retention of beige adipocytes in vivo. The maintained beige fat is thermogenically active, thereby suppressing diet-induced obesity and obesity-induced insulin resistance. Increased autophagy in adipose tissues of obese subjects (Jansen et al., 2012; Kovsan et al., 2011; Nuñez et al., 2013; Ost et al., 2010) could contribute to the accelerated beige-to-white adipocyte conversion.

We further introduce a new model of physiological regulation of autophagy through β3 adrenergic receptor signaling, which explores cross-talk between mTOR and PKA signaling pathways. mTOR signaling pathway is a key regulator of autophagy in response to nutritional cues (Laplante and Sabatini, 2009) (**Figure 1**). β3-AR signaling pathway has been recently implicated in regulating mTORC1 (Liu et al., 2016), a protein complex of mTOR signaling pathway responsible for autophagy. Our group further showed that PKA, a key mediator of β3-AR signaling, represses autophagy in beige adipocytes. Activation of PKA represses *Mitf*, a member of the MiT/TFE family of transcription factors regulating lysosome biogenesis, and its downstream lysosome and autophagy targets. Treatment with PKA inhibitor relieved repression of *Mitf* and autophagy/lysosome components, confirming that PKA is responsible for inhibiting autophagy in beige adipocytes. Additionally, regulation of *Mitf* and associated autophagy genes by PKA was observed even under a starvation conditions, indicating that PKA-mediated repression of autophagy is independent of nutritional signals. Of note, mTORC1 is known to inhibit transcription of autophagy and lysosome target genes by phosphorylating TFEB, another member of the MiT/TFE family, and blocking its translocation to the nucleus (Martina et al., 2012; Roczniak-Ferguson et al., 2012; Settembre et al., 2012). Thus, it is conceivable that PKA-mTORC1 signaling axis simultaneously regulates beige adipocyte development and autophagy through MiT/TFE transcription factors.

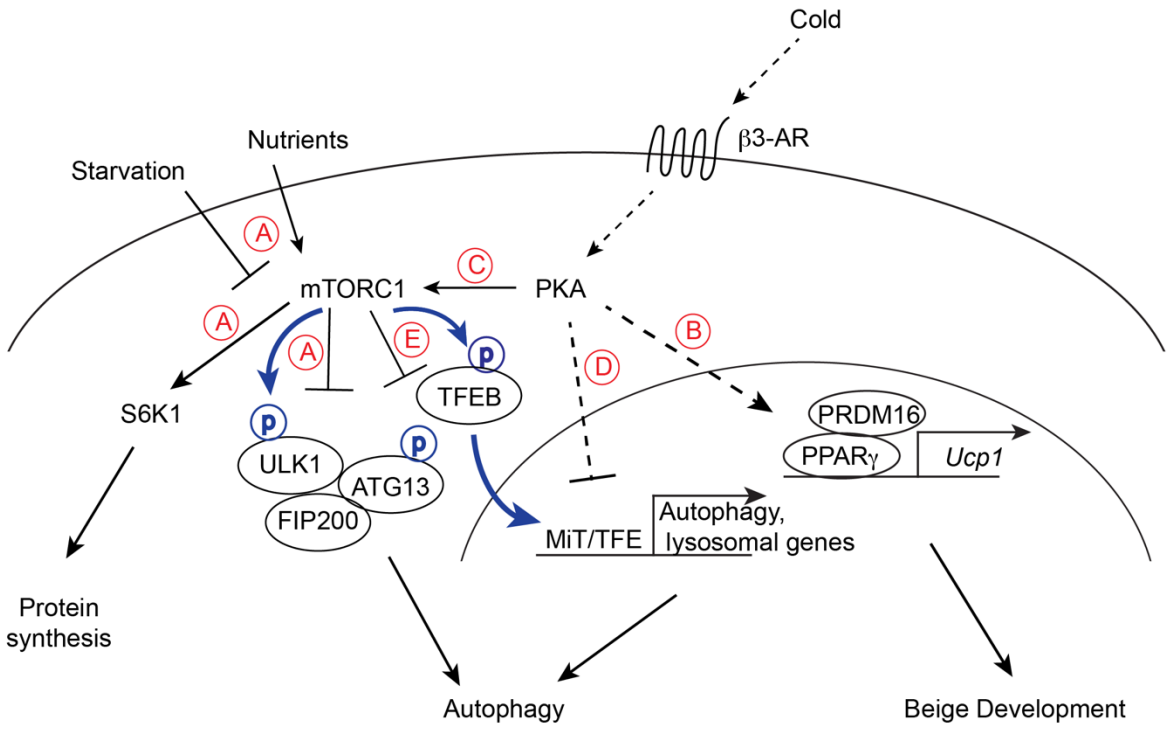

Figure 1. Cross-talk between mTOR and β3-AR signaling pathways in beige adipocytes. (A) Under nutrient-rich conditions**,** mTORC1 is activated and phosphorylates ULK1 and ATG13 to repress the ULK1 complex and block autophagy. In response to starvation mTORC1 inhibited, inducing autophagy. **(B, C)** Activation of PKA in response to β3-AR stimulation induces transcription of brown/beige adipocyte program and promotes mTORC1 activity to inhibit autophagy partly through the regulation of MiT/TFE family of transcription factors. **(D)** PKA activation suppresses the expression of MiT/TFE family and its lysosomal and autophagy targets. **(E)** mTORC1 regulates lysosomal and autophagy gene expression by the nuclear-cytoplasmic shuttling of TFEB (an MiT/TFE family member). Active mTORC1 phosphorylates TFEB and blocks its translocation to the nucleus, preventing transcription of lysosomal and autophagy targets.

Future directions

Our recent study found that mitochondria is dynamically regulated by autophagy during the direct conversion from beige adipocytes to white adipocytes; however, the underlying mechanisms guiding the selectivity of mitochondrial clearance remain unexplored. Here we discuss two compatible possibilities for the selective degradation of mitochondria during the beige-to-white adipocyte conversion.

First possibility is that the mitochondrial degradation is regulated by the brown/beige fat-specific mitochondrial protein UCP1. During beige adipocyte conversion to white following β3-AR withdrawal or re-acclimation to room temperature after cold, loss of UCP1 protein correlated with the loss of mitochondrial respiratory chain complexes. Autophagy accounts for the loss of mitochondrial content during beige adipocyte transition; inhibition of autophagy maintains expression of mtDNA transcripts and mitochondrial respiratory chain complexes. It is possible that mitochondrial removal via autophagy in transitioning beige adipocytes depends on UCP1 protein that acts as an upstream regulator of mitophagy during beige adipocyte transition. To support the hypothesis, *Ucp1* overexpression in white adipocytes induces mitochondrial contents, as assessed by *Cox*4 mRNA, increased mitochondrial cristae density, and increased mitochondrial cytochromes content, whereas cold-acclimated UCP1 null mice have reduced levels of mitochondrial respiratory chain complexes (Rossmeisl et al., 2002; Shabalina et al., 2013). Second possibility of the selective mitophagy during the beige-to-white adipocyte conversion is PINK1/Parkin mediated autopahgy. Beige adipocyte transition is accompanied by a loss of selective adapter proteins p62 and NBR1, both of which are important for of ubiquitin-dependent recognition of the autophagic cargo. p62

and NBR1 contain the ubiquitin binding domain for recognizing cargo targeted for degradation as well as the LC3 binding domain for recruiting LC3 to the cargo. Pink1/Parkin mediated mitophagy is dependent on these adapter proteins and thus is a possible candidate for the mechanism of selective mitophagy during beige transition.

Another intriguing observation is that autophagy mediated degradation of mitochondria in beige adipocytes controls the cellular maintenance of adipocytes. The role of the nucleus in regulating mitochondrial mass and function has been examined extensively in the past; however, the above result indicates that mitochondria, in turn, immensely influence cellular maintenance. What is the molecular signaling that mediates mitochondria-to-nucleus communication? It is conceivable that mitochondrial clearance regulates cellular maintenance and function through altering nuclear gene expression by limiting metabolite availability. For instance, mitochondrial metabolites, such as including those resulting from dysregulation of TCA cycle intermediates, such as α-ketoglutarate (α-KG), succinate, and fumarate, are known to regulate chromatin modifying enzymes, such as Jumonji demethylases that control the adipocyte differentiation program (Inagaki et al., 2016). In fact, we observed that UCP1+ cell-specific inhibition of mitopahgy by Atg12 deletion causes a reduction in nuclear-coded brown fat-selective genes (unpublished data). Additionally, mitochondrial stress in C. *elegans* activates another type of mitochondrial quality control, unfolded mitochondrial protein response (UPR^{mt}), which alters the chromatin structure causing persistent changes in gene expression (Tian et al., 2016). Further studies are needed to uncover the molecular mechanisms and biological roles of the mitochondria-nuclear communication in adipocytes.

Chapter 4: Materials and methods

Animals. All animal experiments were performed under the guidelines established by the UCSF Institutional Animal Care and Use Committee. Unless otherwise specified, all mice used for the experiments are 8-12 weeks old males on C57BL/6 background. *Ucp1*$^{Cre/+}$ mice (Kong et al., 2014) and *Adiponectin*$^{Cre/+}$ mice (Eguchi et al., 2011) were kindly provided by Dr. Evan Rosen in Beth Israel Deaconess Medical Center and Harvard Medical School. *GFP-LC3* mice (Mizushima et al., 2004) and *Atg5*$^{flox/flox}$ mice (Hara et al., 2006) were kindly provided by Dr. Noboru Mizushima at the University of Tokyo, graduate school and faculty of medicine. *Atg12*$^{flox/flox}$ mice were recently described (Malhotra et al., 2015). To visualize brown and beige adipocytes *in vivo*, *Ucp1*$^{Cre/+}$ mice were crossed with Rosa26-GFP or mT/mG mice that were obtained from the Jackson Laboratory. To induce beige adipocyte biogenesis, the ß3-AR agonist CL316,243 (Sigma, C5976) was administered intraperitoneally to male mice at a dose of 1mg kg^{-1} for seven consecutive days. To assess the basal amount of GFP-positive cells present in adipose tissues prior to ß3-AR agonist treatment, mice were bred and treated with ß3-AR agonist at thermoneutrality (30 ˚C). For cold exposure experiments, animals were single-caged and exposed to 6 ˚C for five to seven days. For starvation experiments, mice were deprived of food for 24 hours while maintaining access to water. To examine whether the beige-to-white adipocyte transition is altered under obesity, *Ucp1*$^{Cre/+}$*; mT/mG* reporter mice were fed under a regular diet or high-fat diet for 12 - 16 weeks. For pharmacological inhibition of autophagy, the anti-malarial chloroquine (Sigma, C6628) was administered daily by

intraperitoneal injection at 60 mg kg^{-1} for up to 15 days following ß3-AR agonist withdrawal.

***Ex vivo* monitoring of beige and brown adipocytes.** Mature adipocytes from the inguinal WAT and interscapular BAT depots of CL316,243-treated *Ucp1$^{Cre/+}$;Rosa26-GFP* mice were isolated by fractionation, embedded in collagen gel containing 2.5 mg ml^{-1} Collagen I (BD354236), 1 µg ml^{-1} Fibronectin (Millipore, FC010), and 0.1% BSA. The cell-containing gel was allowed to solidify at 37˚C for 30 min and cultured in DMEM supplemented with 10% FBS. Culture medium did not contain any stimuli, such as ß3-AR agonist, that control beige adipocyte differentiation. Individual live GFP^+ adipocytes were traced daily for ten consecutive days using the In Cell Analyzer 2000 to define and re-image the position of interest over time. Images were processed using In Cell Developer Toolbox V1.8 (GE Healthcare Life Sciences) and Volocity 6.1.1 software (Improvision).

Cell culture. Beige adipocyte differentiation was induced in primary preadipocytes from inguinal WAT by treating with DMEM/F12 medium containing 10% FBS, 0.5 mM isobutylmethylxanthine, 125 nM indomethacin, 2 µg ml^{-1} dexamethasone, 850 nM insulin, and 1 nM T3, and 0.5 µM Rosiglitazone. Two days after induction, cells were switched to the maintenance medium containing 10% FBS, 850 nM insulin, 1 nM T3, and 0.5 µM Rosiglitazone for 7 days. Cells were then pretreated with 10 µM H89 (Cayman chemical) for 1 hour followed by 4 hour treatment with 10 µM Forskolin. Bafilomycin A1 at a dose of 50 nM was used for the assessment of autophagy flux in beige adipocytes.

To induce a fasted condition in culture, differentiated beige adipocytes were cultured in amino acid-free, glucose-free RPMI-1640 (US Biological, Inc., R9010-02) supplemented with 10% dialyzed FBS (Sigma, F0392) for 8 hours.

Immunofluorescence microscopy. For whole-mount immunofluorescence, interscapular BAT and inguinal WAT depots were harvested, chopped into 3-5mm pieces, fixed in 4% paraformaldehyde overnight at 4˚C, blocked in PBS containing 5% goat serum, 1% BSA, and 0.5% Tween20, and immunostained for UCP1 (1:200, abcam, ab10983) and GFP (1:300, Aves Labs, GFP-1020). All fluorescence-conjugated secondary antibodies were purchased from Invitrogen (1:500 dilution). Subsequently, the tissues were serially dehydrated, cleared with Methyl Salicylate and imaged using the inverted Leica TCS SP5 confocal microscope. To assess GFP-LC3 puncta, the inguinal WAT depots from *GFP-LC3* mice were fixed in 4% paraformaldehyde overnight, cryopreserved in 30% sucrose in PBS at 4˚C overnight, embedded in OCT, and cryo-sectioned at 18 μm. Wild-type mice were used as a control to confirm the specificity of GFP signal. Slides were blocked in PBS containing 5% goat serum, 0.2% BSA, and 0.1% Tween20, stained overnight for GFP and Tom20 (1:100, SCBT, sc-11415) at 4 ˚C. The slides were stained with secondary antibodies for one hour at room temperature, and mounted in Vectashield (Vector Labs). Imaging was done using the aforementioned confocal microscope. To assess adipocyte morphology and UCP1 expression under in obese or lean mice, tissues were fixed in 4% paraformaldehyde for 30min at room temperature (RT), cryopreserved in 30% sucrose in PBS at 4˚C overnight, embedded in OCT, and cryosectioned at 100 μm. Slides were post-fixed with 4% paraformaldehyde for

15 min (RT), blocked in PBS containing 5% goat serum, 0.2% BSA, and 0.1% Tween20, stained overnight for UCP1 (1:200). mGFP and UCP1 expression were visualized by confocal microscopy.

Optical clearing of adipose tissues. BAT and inguinal WAT depots were cut into 3-5mm pieces, immediately fixed in 4% PFA overnight at 4˚C, washed with PBS, dehydrated using serial ethanol washes, and then incubated in methyl salicylate (Sigma) for 30 min. Brightfield images were obtained using Olympus MVX10 stereomicroscope. All imaging analysis was carried out using Volocity 6.1.1 (Improvision) acquisition software.

Flow Cytometry. To isolate GFP-positive adipocytes, inguinal WAT depots from *Ucp1*$^{Cre/+}$*;Rosa26-GFP* or Adiponectin$^{Cre/+}$*;Rosa26-GFP* mice were digested to single cells using Collagenase D (1.5 U ml^{-1}) and Dispase II (2.5 U ml^{-1}).). Adipocytes were first gated based on size and granularity. Dead cells were removed based on Sytox Blue (1:400) staining. GFP-positive cells were gated based on GFP-negative control cells from wild-type mice not expressing GFP. The same sorting strategy was used to isolate RFP-positive adipocytes from *Ucp1*$^{Cre/+;}$*Atg12*$^{flox/flox}$*;Rosa26-LSL-RFP* and *Ucp1*$^{Cre/+;}$*Atg5*$^{flox/flox}$*;Rosa26-LSL-RFP* mice. Preadipocytes (Lin^{-}/CD29^{+}/CD34^{+}/Sca1^{+}) were isolated from the stromal vascular fraction of wild-type mice using the following antibodies: Sca-1-PB (1:800, Biolegend 108120), CD45-PE (1:200, eBioscience, 12-0451-82), CD31-PE (1:300, bdbiosciences, 553373), CD11b-PE-Cy7 (1:3000 eBiescience), CD29-Alexa700 (1:400 Biolegend, 102218), CD34-FITC (1:25,

eBioscience, 11-0341-85), Ter119-PE (1:200, Biolegend, 116207), Sytox Red (1:1000) in 4% BSA in PBS. All the cells were isolated into Trizol LS using FACS Aria II (Becton Dickinson) equipped with 130 μm nozzle diameter for adipocytes or 100 μm for preadipocytes. To monitor autophagic flux in *GFP-LC3* mice *in vivo*, adipocyte fractions were analyzed for GFP using FACS LSR II (Becton Dickinson), as described previously (Warr et al., 2013). As a positive control for autophagic flux quantification, the GFP-LC3 signal was monitored in the inguinal WAT of *GFP-LC3* mice. The mice were under a fed state or fasted state for 24 hours to induce autophagy (Supplementary Fig. 6A) (Mizushima et al., 2004). FlowJo software was used for data analysis.

Metabolic studies. To assess whole-body energy expenditures, 10-week-old *Atg12*$^{Ucp1\ KO}$ mice (*Ucp1*$^{Cre/+}$;*Atg12*$^{flox/flox}$) and body-weight-matched littermate control mice (*Atg12* $^{flox/flox}$) were treated with β3-AR agonist for 7 days and maintained at thermoneutrality during β3-AR agonist withdrawal. Whole-body energy expenditure was measured at room temperature between 17 and 18 days after β3-AR agonist withdrawal using a Comprehensive Lab Animal Monitoring System (CLAMS, Columbus Instruments). Locomotor activity was simultaneously monitored by the CLAMS. For diet-induced obesity study, 9-week-old *Atg12*$^{Ucp1\ KO}$ and control (*Atg12* $^{flox/flox}$) male mice were fed a high-fat diet (HFD) (60% kcal%, D12492, Research Diet Inc.). One week prior to cold acclimation at 6 ˚C, mice were fed with HFD. Following seven- day cold exposure, mice were transferred to thermoneutrality (30 ˚C) for 8 weeks. Body weight was measured twice per week. Glucose tolerance test experiments were performed at 8 weeks or 12 weeks of high-fat diet, as indicated. After an overnight fast, the mice were injected intraperitoneally

with 1.5 g kg^{-1} glucose. Insulin tolerance test was performed after 8.5 weeks of high-fat diet. After a 3 hour fast, mice were injected intraperitoneally with 0.75 U kg^{-1} Insulin (Novolin). Blood samples were collected at indicated time points and amounts of glucose were measured using blood glucose test strips (FreeStyle Lite).

RNA-sequencing. Total RNA was extracted from FACS-isolated GFP-positive adipocytes or preadipocytes using the RNeasy Micro Kit (Qiagen). RNA quality (RIN: RNA Integrity Number) was determined by Bioanalyzer (Agilent Technologies) and samples with RIN of >7.0 were subjected to RNA-sequencing. Libraries were constructed from minimum of 22 ng of total RNA as previously described (Shinoda et al., 2015). High-throughput sequencing was performed using a HiSeq 2500 instrument (Illumina) at the UCSF Institute for Human Genetics core facility. Quality control check on the raw sequence data was done by FastQC (The Babraham Bioinformatics). Raw sequences were mapped using TopHat version 2.0.8 against the mouse (version: mm10) genome. The mapped sequences were converted to FPKM (fragments per kilobase of exon per million fragments mapped) by running Cuffdiff 2.1.1 (Trapnell et al., 2013) to determine gene expression. Reproducibility of the RNA-sequencing data was confirmed by sequencing the identical RNA-samples (R^2 = 0.983). The data were deposited in ArrayExpress (http://www.ebi.ac.uk/arrayexpress/) under accession numbers E-MTAB-3978. RNA-sequencing dataset of the inguinal WAT from mice kept under ambinent temperature and 4˚C cold for 5 days has been described previously (Shinoda et al., 2015) and analyzed by pseudoalignment-based quantification program kallisto (Bray et al., 2016).

Multivariate Statistics. Clustering of genes was performed as follows: the FPKM profiles of genes at several time points (day 0 - 30 of ß3-AR agonist withdrawal) were *z*-transformed, as such, the mean for each gene was zero and standard deviation was one. The Fuzzy C-Means (FCM) clustering analysis was described elsewhere (Olsen et al., 2006). Subsequently, the *z*-transformed expression profiles were clustered based on the FCM clustering algorithm implemented in Mfuzz toolbox (Futschik and Carlisle, 2005). The top 10,000 highly expressed genes were used for the clustering. The FCM parameters were c = 9 and m = 1.15, respectively. For principal component analysis (PCA), preadipocytes ($Lin^-/CD29^+/CD34^+/Sca1^+$) and white adipocytes (*Adiponectin* $^{Cre/+}$;*Rosa26-GFP*) were first mapped onto two-dimensional (PC1 and PC2) space, based on the expression of 10,138 genes that showed differences between the two groups by 2-fold or more. Subsequently, the transcriptome of GFP-positive adipocytes at each time point (day 0-30) was mapped on the same PC plot, based on the expression levels of 10,138 genes. Similar PC plots were reproducibly found when different number of genes (2,000, 1,000, or 500) were applied. Above statistical analyses were performed using the JMP software version 11 (SAS Institute) or Multi Experiment Viewer (MeV) (Saeed et al., 2003). Gene Ontology (GO) enrichment analysis was performed in DAVID (Huang et al., 2008) using the biological process and cellular component terms. Transcription factor binding motif analysis was performed by Hypergeometric Optimization of Motif EnRichment analysis (HOMER) (Heinz et al., 2010).

Transmission electron microscopy. Adipose tissues were fixed in PBS, containing 2.0% electron microscopy grade glutaraldehyde and 2.5% formaldehyde, and immediately minced to 1 mm cubes. The adipose tissue samples were processed at the Diabetes Center (UCSF) electron microscopy core facility for standard transmission electron microscopy processing and imaging using JEOL 1400 transmission electron microscope.

Mitochondrial respiration assays. Oxygen consumption rate (OCR) in the inguinal WAT and interscapular BAT was measured using the Seahorse XFe Extracellular Flux Analyzer. The adipose tissues (1.5 mg) were placed into XF24 Islet Capture Microplates (Seahorse Bioscience) and pre-incubated for one hour with assay media in the presence or absence of 5 μM isoproterenol (Sigma I6504-500MG) to induce cAMP-dependent respiration. For *ex vivo* culture experiments, inguinal WAT depots were isolated from wild-type mice treated with 7-day β3-AR agonist and maintained in DMEM (10-017-CV) supplemented with 10% FBS for 3, 5, and 10 days after β3-AR agonist withdrawal. The XF assay medium was supplemented with 1 mM sodium pyruvate, 2 mM GlutaMAX™-I, and 25 mM glucose. Tissues were subjected to the mitochondrial stress test by adding 10 μM oligomycin (Cell Signaling; 9996), followed by 20 μM carbonyl cyanide 4-(trifluoromethoxy) phenylhydrazone (FCCP) (Sigma, C2920-10MG) and 20 μM antimycin (Sigma, A8674-50MG). The timing of measurements was carried out as detailed elsewhere (Dunham-Snary et al., 2014).

RNA Preparation and Quantitative PCR. Total RNA was extracted from inguinal WAT depots using Trizol followed by the RNeasy mini-kit (Qiagen). Gene expression analysis of adipose tissues was carried out as detailed elsewhere (Sharp et al., 2012). The primer sequences are listed in **Supplementary Table 2.**

Immunoblotting. Protein lysates from adipose tissues was extracted using Qiagen TissueLyzer LT and RIPA buffer containing 50 mM Tris, pH 7.5, 150 mM NaCl, 1% Triton-X, 10% glycerol, and cOmplete protease inhibitors (Roche). For monitoring autophagy, the adipocyte fraction from inguinal WAT depots was isolated and applied for immunoblotting. The following antibodies were used in immunoblotting; UCP1 (1:1000, abcam, ab10983), MitoProfile® total OXPHOS rodent antibody cocktail (1:1000, abcam, ab110413), β–actin (1:10,000, Sigma, A3854), ATG12 (1:1000, Cell Signaling, 4180S), ATG5 (1:1000, Cell Signaling, 12994S), NBR1 (1:1000, Novus Bio, NBP1-71703), p62/SQSTM1 (1:1000, Novus Bio, H00008878-M01), LC3 (1:1000, Cell Signaling, 12741S), and COX IV (1:000, Cell Signaling, 4850).

Statistical analyses. Unpaired Student's *t*-test was applied to determine the statistical difference, except for the following analyses: unpaired two-tailed Mann-Whitney U test was applied to compare LC3 puncta at different stages of beige-to-white transition; two-way repeated-measures ANOVA followed by Fisher's LSD test were applied to determine the statistical difference in body weight gain. *P* values below 0.05 were considered significant throughout the study.

Allen, G.F.G., Toth, R., James, J., and Ganley, I.G. (2013). Loss of iron triggers PINK1/Parkin-independent mitophagy. EMBO Rep. *14*, 1127–1135.

Altshuler-Keylin, S., Shinoda, K., Hasegawa, Y., Ikeda, K., Hong, H., Kang, Q., Yang, Y., Perera, R.M., Debnath, J., and Kajimura, S. (2016). Beige Adipocyte Maintenance Is Regulated by Autophagy-Induced Mitochondrial Clearance. Cell Metab. *24*, 402–419.

Atit, R., Sgaier, S.K., Mohamed, O.A., Taketo, M.M., Dufort, D., Joyner, A.L., Niswander, L., and Conlon, R.A. (2006). Beta-catenin activation is necessary and sufficient to specify the dorsal dermal fate in the mouse. Dev Biol *296*, 164–176.

Baerga, R., Zhang, Y., Chen, P.-H., Goldman, S., and Jin, S.V. (2009). Targeted deletion of autophagy-related 5(atg5) impairs adipogenesis in a cellular model and in mice. Autophagy *5*, 1118–1130.

Barbatelli, G., Murano, I., Madsen, L., Hao, Q., Jimenez, M., Kristiansen, K., Giacobino, J.P., De Matteis, R., and Cinti, S. (2010). The emergence of cold-induced brown adipocytes in mouse white fat depots is determined predominantly by white to brown adipocyte transdifferentiation. Am. J. Physiol. Endocrinol. Metab. *298*, E1244–E1253.

Bi, P., Shan, T., Liu, W., Yue, F., Yang, X., Liang, X.-R., Wang, J., Li, J., Carlesso, N., Liu, X., et al. (2014). Inhibition of Notch signaling promotes browning of white adipose tissue and ameliorates obesity. Nature Medicine *20*, 911–918.

Bowman, C.J., Ayer, D.E., and Dynlacht, B.D. (2014). Foxk proteins repress the initiation of starvation-induced atrophy and autophagy programs. Nat Cell Biol *16*, 1202–1214.

Bray, N.L., Pimentel, H., Melsted, P., and Pachter, L. (2016). Near-optimal probabilistic RNA-seq quantification. Nat. Biotechnol. *34*, 525–527.

Cairó, M., Villarroya, J., Cereijo, R., Campderrós, L., Giralt, M., and Villarroya, F. (2016). Thermogenic activation represses autophagy in brown adipose tissue. Int J Obes Relat Metab Disord *40*, 1591–1599.

Cederberg, A., Grønning, L.M., Ahrén, B., Taskén, K., Carlsson, P., and Enerback, S. (2001). FOXC2 is a winged helix gene that counteracts obesity, hypertriglyceridemia, and diet-induced insulin resistance. Cell *106*, 563–573.

Chauhan, S., Goodwin, J.G., Chauhan, S., Manyam, G., Wang, J., Kamat, A.M., and Boyd, D.D. (2013). ZKSCAN3 Is a Master Transcriptional Repressor of Autophagy. Molecular Cell *50*, 16–28.

Cinti, S. (1999). The adipose organ (Editrice Kurtis, Milano, Italy).

Collins, S. (2011). β-Adrenoceptor Signaling Networks in Adipocytes for Recruiting Stored Fat and Energy Expenditure. Front Endocrinol (Lausanne) *2*, 102.

Cypess, A.M., Lehman, S., Williams, G., Tal, I., Rodman, D., Goldfine, A.B., Kuo, F.C., Palmer, E.L., Tseng, Y.-H., Doria, A., et al. (2009). Identification and importance of brown adipose tissue in adult humans. N Engl J Med *360*, 1509–1517.

Cypess, A.M., White, A.P., Vernochet, C., Schulz, T.J., Xue, R., Sass, C.A., Huang, T.L., Roberts-Toler, C., Weiner, L.S., Sze, C., et al. (2013). Anatomical localization, gene expression profiling and functional characterization of adult human neck brown fat. Nature Medicine *19*, 635–639.

Ebato, C., Uchida, T., Arakawa, M., Komatsu, M., Ueno, T., Komiya, K., Azuma, K., Hirose, T., Tanaka, K., Kominami, E., et al. (2008). Autophagy is important in islet homeostasis and compensatory increase of beta cell mass in response to high-fat diet. Cell Metab. *8*, 325–332.

Eguchi, J., Wang, X., Yu, S., Kershaw, E.E., Chiu, P.C., Dushay, J., Estall, J.L., Klein, U., Maratos-Flier, E., and Rosen, E.D. (2011). Transcriptional Control of Adipose Lipid Handling by IRF4. Cell Metab. *13*, 249–259.

Eskelinen, E.-L., Reggiori, F., Baba, M., Kovács, A.L., and Seglen, P.O. (2011). Seeing is believing: The impact of electron microscopy on autophagy research. Autophagy *7*, 935–956.

Ezaki, J., Matsumoto, N., Takeda-Ezaki, M., Komatsu, M., Takahashi, K., Hiraoka, Y., Taka, H., Fujimura, T., Takehana, K., Yoshida, M., et al. (2011). Liver autophagy contributes to the maintenance of blood glucose and amino acid levels. Autophagy *7*, 727–736.

Fedorenko, A., Lishko, P.V., and Kirichok, Y. (2012). Mechanism of Fatty-Acid-Dependent UCP1 Uncoupling in Brown Fat Mitochondria. Cell *151*, 400–413.

Feldmann, H.M., Golozoubova, V., Cannon, B., and Nedergaard, J. (2009). UCP1 ablation induces obesity and abolishes diet-induced thermogenesis in mice exempt from thermal stress by living at thermoneutrality. Cell Metab. *9*, 203–209.

Frontini, A., and Cinti, S. (2010). Distribution and development of brown adipocytes in the murine and human adipose organ. Cell Metab. *11*, 253–256.

Futschik, M.E., and Carlisle, B. (2005). Noise-robust soft clustering of gene expression time-course data. J Bioinform Comput Biol *3*, 965–988.

Gospodarska, E., Nowialis, P., and Kozak, L.P. (2015). Mitochondrial turnover: A phenotype distinguishing brown adipocytes from interscapular brown adipose tissue and white adipose tissue. Journal of Biological Chemistry.

Guerra, C.C., Koza, R.A.R., Yamashita, H.H., Walsh, K.K., and Kozak, L.P.L. (1998). Emergence of brown adipocytes in white fat in mice is under genetic control. Effects on body weight and adiposity. J Clin Invest *102*, 412–420.

Hanna, R.A., Quinsay, M.N., Orogo, A.M., Giang, K., Rikka, S., and Gustafsson, A.B. (2012). Microtubule-associated Protein 1 Light Chain 3 (LC3) Interacts with Bnip3 Protein to Selectively Remove Endoplasmic Reticulum and Mitochondria via Autophagy. Journal of Biological Chemistry *287*, 19094–19104.

Hara, T., Nakamura, K., Matsui, M., Yamamoto, A., Nakahara, Y., Suzuki-Migishima, R., Yokoyama, M., Mishima, K., Saito, I., Okano, H., et al. (2006). Suppression of basal autophagy in neural cells causes neurodegenerative disease in mice. Nature *441*, 885–889.

Heinz, S., Benner, C., Spann, N., Bertolino, E., Lin, Y.C., Laslo, P., Cheng, J.X., Murre, C., Singh, H., and Glass, C.K. (2010). Simple combinations of lineage-determining transcription factors prime cis-regulatory elements required for macrophage and B cell identities. Molecular Cell *38*, 576–589.

Heo, J.-M., Ordureau, A., Paulo, J.A., Rinehart, J., and Harper, J.W. (2015). The PINK1-PARKIN Mitochondrial Ubiquitylation Pathway Drives a Program of OPTN/NDP52 Recruitment and TBK1 Activation to Promote Mitophagy. Molecular Cell *60*, 7–20.

Hernandez, G., Thornton, C., Stotland, A., Lui, D., Sin, J., Ramil, J., Magee, N., Andres, A., Quarato, G., Carreira, R.S., et al. (2013). MitoTimer: a novel tool for monitoring mitochondrial turnover. Autophagy *9*, 1852–1861.

Hernández-Gea, V., Ghiassi-Nejad, Z., Rozenfeld, R., Gordon, R., Fiel, M.I., Yue, Z., Czaja, M.J., and Friedman, S.L. (2012). Autophagy releases lipid that promotes fibrogenesis by activated hepatic stellate cells in mice and in human tissues. Gastroenterology *142*, 938–946.

Himms-Hagen, J., Melnyk, A., Zingaretti, M.C., Ceresi, E., Barbatelli, G., and Cinti, S. (2000). Multilocular fat cells in WAT of CL-316243-treated rats derive directly from white adipocytes. AJP: Cell Physiology *279*, C670–C681.

Hoshino, A., Ariyoshi, M., Okawa, Y., Kaimoto, S., Uchihashi, M., Fukai, K., Iwai-Kanai, E., Ikeda, K., Ueyama, T., Ogata, T., et al. (2014). Inhibition of p53 preserves Parkin-mediated mitophagy and pancreatic β-cell function in diabetes. Proceedings of the National Academy of Sciences *111*, 3116–3121.

Huang, D.W., Sherman, B.T., and Lempicki, R.A. (2008). Systematic and integrative analysis of large gene lists using DAVID bioinformatics resources. Nat Protoc *4*, 44–57.

Inagaki, T., Sakai, J., and Kajimura, S. (2016). Transcriptional and epigenetic control of brown and beige adipose cell fate and function. Nat. Rev. Mol. Cell Biol. *17*, 480–495.

Jaber, N., Dou, Z., Chen, J.-S., Catanzaro, J., Jiang, Y.-P., Ballou, L.M., Selinger, E., Ouyang, X., Lin, R.Z., Zhang, J., et al. (2012). Class III PI3K Vps34 plays an essential role in autophagy and in heart and liver function. Proceedings of the National Academy of Sciences *109*, 2003–2008.

Jansen, H.J., van Essen, P., Koenen, T., Joosten, L.A.B., Netea, M.G., Tack, C.J., and Stienstra, R. (2012). Autophagy activity is up-regulated in adipose tissue of obese individuals and modulates proinflammatory cytokine expression. Endocrinology *153*, 5866–5874.

Jung, H.S., Chung, K.W., Kim, J.W., Kim, J., Komatsu, M., Tanaka, K., Nguyen, Y.H., Kang, T.M., Yoon, K.-H., Kim, J.-W., et al. (2008). Loss of autophagy diminishes pancreatic beta cell mass and function with resultant hyperglycemia. Cell Metab. *8*, 318–324.

Kajimura, S., and Saito, M. (2013). A New Era in Brown Adipose Tissue Biology: Molecular Control of Brown Fat Development and Energy Homeostasis. Annu. Rev. Physiol. *76*, 131104113515001.

Kajimura, S., Seale, P., Tomaru, T., Erdjument-Bromage, H., Cooper, M.P., Ruas, J.L., Chin, S., Tempst, P., Lazar, M.A., and Spiegelman, B.M. (2008). Regulation of the brown and white fat gene programs through a PRDM16/CtBP transcriptional complex. Genes Dev. *22*, 1397–1409.

Kajimura, S., Spiegelman, B.M., and Seale, P. (2015). Brown and Beige Fat: Physiological Roles beyond Heat Generation. Cell Metab. *22*, 546–559.

Katayama, H., Kogure, T., Mizushima, N., Yoshimori, T., and Miyawaki, A. (2011). A sensitive and quantitative technique for detecting autophagic events based on lysosomal delivery. Chem. Biol. *18*, 1042–1052.

Kaushik, S., and Cuervo, A.M. (2016). AMPK-dependent phosphorylation of lipid droplet protein PLIN2 triggers its degradation by CMA. Autophagy *12*, 432–438.

Kaushik, S., Rodriguez-Navarro, J.A., Arias, E., Kiffin, R., Sahu, S., Schwartz, G.J., Cuervo, A.M., and Singh, R. (2011). Autophagy in hypothalamic AgRP neurons regulates food intake and energy balance. Cell Metab. *14*, 173–183.

Kelly, D.P., and Scarpulla, R.C. (2004). Transcriptional regulatory circuits controlling mitochondrial biogenesis and function. Genes Dev. *18*, 357–368.

Kim, K.H., Jeong, Y.T., Oh, H., Kim, S.H., Cho, J.M., Kim, Y.-N., Kim, S.S., Kim, D.H., Hur, K.Y., Kim, H.K., et al. (2013). Autophagy deficiency leads to protection from obesity and insulin resistance by inducing Fgf21 as a mitokine. Nature Medicine *19*, 83–92.

Kim, K.-Y., Stevens, M.V., Akter, M.H., Rusk, S.E., Huang, R.J., Cohen, A., Noguchi, A., Springer, D., Bocharov, A.V., Eggerman, T.L., et al. (2011). Parkin is a lipid-responsive regulator of fat uptake in mice and mutant human cells. J. Clin. Invest. *121*, 3701–3712.

Kimmey, J.M., Huynh, J.P., Weiss, L.A., Park, S., Kambal, A., Debnath, J., Virgin, H.W., and Stallings, C.L. (2015). Unique role for ATG5 in neutrophil-mediated immunopathology during M. tuberculosis infection. Nature *528*, 565–569.

Kimura, S., Noda, T., and Yoshimori, T. (2007). Dissection of the autophagosome maturation process by a novel reporter protein, tandem fluorescent-tagged LC3. Autophagy *3*, 452–460.

Kirkin, V., Lamark, T., Sou, Y.-S., Bjørkøy, G., Nunn, J.L., Bruun, J.-A., Shvets, E., McEwan, D.G., Clausen, T.H., Wild, P., et al. (2009). A role for NBR1 in autophagosomal degradation of ubiquitinated substrates. Molecular Cell *33*, 505–516.

Klionsky, D.J., Abdalla, F.C., Abeliovich, H., Abraham, R.T., Acevedo-Arozena, A., Adeli, K., Agholme, L., Agnello, M., Agostinis, P., Aguirre-Ghiso, J.A., et al. (2012). Guidelines for the use and interpretation of assays for monitoring autophagy. *8*, 445–544.

Klionsky, D.J., Abdelmohsen, K., Abe, A., Abedin, M.J., Abeliovich, H., Acevedo-Arozena, A., Adachi, H., Adams, C.M., Adams, P.D., Adeli, K., et al. (2016). Guidelines for the use and interpretation of assays for monitoring autophagy (3rd edition). Autophagy *12*, 1–222.

Komatsu, M., Kurokawa, H., Waguri, S., Taguchi, K., Kobayashi, A., Ichimura, Y., Sou, Y.-S., Ueno, I., Sakamoto, A., Tong, K.I., et al. The selective autophagy substrate p62 activates the stress responsive transcription factor Nrf2 through inactivation of Keap1. Nat Cell Biol *12*, 213–223.

Kong, X., Banks, A., Liu, T., Kazak, L., Rao, R.R., Cohen, P., Wang, X., Yu, S., Lo, J.C., Tseng, Y.-H., et al. (2014). IRF4 Is a Key Thermogenic Transcriptional Partner of PGC-1α. Cell *158*, 69–83.

Kosacka, J., Kern, M., Klöting, N., Paeschke, S., Rudich, A., Haim, Y., Gericke, M., Serke, H., Stumvoll, M., Bechmann, I., et al. (2015). Autophagy in adipose tissue of patients with obesity and type 2 diabetes. Mol. Cell. Endocrinol. *409*, 21–32.

Kovsan, J., Blüher, M., Tarnovscki, T., Klöting, N., Kirshtein, B., Madar, L., Shai, I., Golan, R., Harman-Boehm, I., Schön, M.R., et al. (2011). Altered autophagy in human adipose tissues in obesity. J. Clin. Endocrinol. Metab. *96*, E268–E277.

Kuma, A., Hatano, M., Matsui, M., Yamamoto, A., Nakaya, H., Yoshimori, T., Ohsumi, Y., Tokuhisa, T., and Mizushima, N. (2004). The role of autophagy during the early neonatal starvation period. Nature *432*, 1032–1036.

Laker, R.C., Xu, P., Ryall, K.A., Sujkowski, A., Kenwood, B.M., Chain, K.H., Zhang, M., Royal, M.A., Hoehn, K.L., Driscoll, M., et al. (2014). A Novel MitoTimer Reporter Gene for Mitochondrial Content, Structure, Stress, and Damage in Vivo. J. Biol. Chem. *289*, 12005–12015.

Lamb, C.A., Yoshimori, T., and Tooze, S.A. (2013). The autophagosome: origins unknown, biogenesis complex. Nat. Rev. Mol. Cell Biol. *14*, 759–774.

Laplante, M., and Sabatini, D.M. (2009). mTOR signaling at a glance. J. Cell. Sci. *122*,

3589–3594.

Lazarou, M., Sliter, D.A., Kane, L.A., Sarraf, S.A., Wang, C., Burman, J.L., Sideris, D.P., Fogel, A.I., and Youle, R.J. (2015). The ubiquitin kinase PINK1 recruits autophagy receptors to induce mitophagy. Nature *524*, 309–314.

Lee, I.H. (2012). Atg7 modulates p53 activity to regulate cell cycle and survival during metabolic stress (vol 336, pg 225, 2012). Science *337*, 911–911.

Lee, J.M., Wagner, M., Xiao, R., Kim, K.H., Feng, D., Lazar, M.A., and Moore, D.D. (2014a). Nutrient-sensing nuclear receptors coordinate autophagy. Nature *516*, 112–115.

Lee, P., Werner, C.D., Kebebew, E., and Celi, F.S. (2013a). Functional thermogenic beige adipogenesis is inducible in human neck fat. Int J Obes Relat Metab Disord *38*, 170–176.

Lee, P., Smith, S., Linderman, J., Courville, A.B., Brychta, R.J., Dieckmann, W., Werner, C.D., Chen, K.Y., and Celi, F.S. (2014b). Temperature-acclimated brown adipose tissue modulates insulin sensitivity in humans. Diabetes.

Lee, Y.-H., Mottillo, E.P., and Granneman, J.G. (2013b). Adipose tissue plasticity from WAT to BAT and in between. Biochim. Biophys. Acta.

Lee, Y.-H., Petkova, A.P., Konkar, A.A., and Granneman, J.G. (2015). Cellular origins of cold-induced brown adipocytes in adult mice. Faseb J *29*, 286–299.

Lee, Y.-H., Petkova, A.P., Mottillo, E.P., and Granneman, J.G. (2012). In vivo identification of bipotential adipocyte progenitors recruited by β3-adrenoceptor activation and high-fat feeding. Cell Metab. *15*, 480–491.

Lidell, M.E., Betz, M.J., Dahlqvist Leinhard, O., Heglind, M., Elander, L., Slawik, M., Mussack, T., Nilsson, D., Romu, T., Nuutila, P., et al. (2013). Evidence for two types of brown adipose tissue in humans. Nature Medicine *19*, 631–634.

Liu, D., Bordicchia, M., Zhang, C., Fang, H., Wei, W., Li, J.-L., Guilherme, A., Guntur, K., Czech, M.P., and Collins, S. (2016). Activation of mTORC1 is essential for β-adrenergic stimulation of adipose browning. J. Clin. Invest. *126*, 1704–1716.

Liu, L., Feng, D., Chen, G., Chen, M., Zheng, Q., Song, P., Ma, Q., Zhu, C., Wang, R., Qi, W., et al. (2012). Mitochondrial outer-membrane protein FUNDC1 mediates hypoxia-induced mitophagy in mammalian cells. Nat Cell Biol *14*, 177–185.

Malhotra, R., Warne, J.P., Salas, E., Xu, A.W., and Debnath, J. (2015). Loss of Atg12, but not Atg5, in pro-opiomelanocortin neurons exacerbates diet-induced obesity. Autophagy *11*, 145–154.

Martina, J.A., Chen, Y., Gucek, M., and Puertollano, R. (2012). MTORC1 functions as a

transcriptional regulator of autophagy by preventing nuclear transport of TFEB. Autophagy *8*, 903–914.

Martinez-Lopez, N., Athonvarangkul, D., Sahu, S., Coletto, L., Zong, H., Bastie, C.C., Pessin, J.E., Schwartz, G.J., and Singh, R. (2013). Autophagy in Myf5+ progenitors regulates energy and glucose homeostasis through control of brown fat and skeletal muscle development. EMBO Rep. *14*, 795.

Martinez-Lopez, N., Garcia-Macia, M., Sahu, S., Athonvarangkul, D., Liebling, E., Merlo, P., Cecconi, F., Schwartz, G.J., and Singh, R. (2015). Autophagy in the CNS and Periphery Coordinate Lipophagy and Lipolysis in the Brown Adipose Tissue and Liver. Cell Metab.

Martinez-Vicente, M., Talloczy, Z., Wong, E., Tang, G., Koga, H., Kaushik, S., de Vries, R., Arias, E., Harris, S., Sulzer, D., et al. (2010). Cargo recognition failure is responsible for inefficient autophagy in Huntington's disease. Nat Neurosci *13*, 567–576.

Mizushima, N. (2009). Methods for monitoring autophagy using GFP-LC3 transgenic mice. Meth. Enzymol. *452*, 13–23.

Mizushima, N., and Komatsu, M. (2011). Autophagy: Renovation of Cells and Tissues. Cell *147*, 728–741.

Mizushima, N., Yamamoto, A., Matsui, M., Yoshimori, T., and Ohsumi, Y. (2004). In vivo analysis of autophagy in response to nutrient starvation using transgenic mice expressing a fluorescent autophagosome marker. Molecular Biology of the Cell *15*, 1101–1111.

Mortensen, M., Ferguson, D.J.P., Edelmann, M., Kessler, B., Morten, K.J., Komatsu, M., and Simon, A.K. (2010). Loss of autophagy in erythroid cells leads to defective removal of mitochondria and severe anemia in vivo. Proceedings of the National Academy of Sciences *107*, 832–837.

Moscat, J., Diaz-Meco, M.T., and Wooten, M.W. (2007). Signal integration and diversification through the p62 scaffold protein. Trends Biochem. Sci. *32*, 95–100.

Mullican, S.E., Tomaru, T., Gaddis, C.A., Peed, L.C., Sundaram, A., and Lazar, M.A. (2013). A Novel Adipose-Specific Gene Deletion Model Demonstrates Potential Pitfalls of Existing Methods. Mol Endocrinol *27*, 127–134.

Murakawa, T., Yamaguchi, O., Hashimoto, A., Hikoso, S., Takeda, T., Oka, T., Yasui, H., Ueda, H., Akazawa, Y., Nakayama, H., et al. (2015). Bcl-2-like protein 13 is a mammalian Atg32 homologue that mediates mitophagy and mitochondrial fragmentation. Nat Commun *6*, 7527.

Müller, T.D., Lee, S.J., Jastroch, M., Kabra, D., Stemmer, K., Aichler, M., Abplanalp, B., Ananthakrishnan, G., Bhardwaj, N., Collins, S., et al. (2013). p62 links β-adrenergic input to mitochondrial function and thermogenesis. J. Clin. Invest. *123*, 469–478.

Narendra, D.P., Jin, S.M., Tanaka, A., Suen, D.-F., Gautier, C.A., Shen, J., Cookson, M.R., and Youle, R.J. (2010). PINK1 is selectively stabilized on impaired mitochondria to activate Parkin. PLoS Biol *8*, e1000298–e1000298.

Nezich, C.L., Wang, C., Fogel, A.I., and Youle, R.J. (2015). MiT/TFE transcription factors are activated during mitophagy downstream of Parkin and Atg5. J. Cell Biol. *210*, 435–450.

Novak, I., Kirkin, V., McEwan, D.G., Zhang, J., Wild, P., Rozenknop, A., Rogov, V., Löhr, F., Popovic, D., Occhipinti, A., et al. (2010). Nix is a selective autophagy receptor for mitochondrial clearance. EMBO Rep. *11*, 45–51.

Nuñez, C.E., Rodrigues, V.S., Gomes, F.S., Moura, R.F. de, Victorio, S.C., Bombassaro, B., Chaim, E.A., Pareja, J.C., Geloneze, B., Velloso, L.A., et al. (2013). Defective regulation of adipose tissue autophagy in obesity. Int J Obes Relat Metab Disord *37*, 1473–1480.

Olsen, J.V., Blagoev, B., Gnad, F., Macek, B., Kumar, C., Mortensen, P., and Mann, M. (2006). Global, in vivo, and site-specific phosphorylation dynamics in signaling networks. Cell *127*, 635–648.

Orava, J., Nuutila, P., Noponen, T., Parkkola, R., Viljanen, T., Enerbäck, S., Rissanen, A., Pietiläinen, K.H., and Virtanen, K.A. (2013). Blunted metabolic responses to cold and insulin stimulation in brown adipose tissue of obese humans - Orava - 2013 - Obesity - Wiley Online Library. Obesity (Silver Spring) *21*, 2279–2287.

Ost, A., Svensson, K., Ruishalme, I., Brännmark, C., Franck, N., Krook, H., Sandström, P., Kjolhede, P., and Strålfors, P. (2010). Attenuated mTOR signaling and enhanced autophagy in adipocytes from obese patients with type 2 diabetes. Mol. Med. *16*, 235–246.

Palmieri, M., Impey, S., Kang, H., di Ronza, A., Pelz, C., Sardiello, M., and Ballabio, A. (2011). Characterization of the CLEAR network reveals an integrated control of cellular clearance pathways. Hum Mol Genet *20*, 3852–3866.

Perera, R.M., Stoykova, S., Nicolay, B.N., Ross, K.N., Fitamant, J., Boukhali, M., Lengrand, J., Deshpande, V., Selig, M.K., Ferrone, C.R., et al. (2015). Transcriptional control of autophagy-lysosome function drives pancreatic cancer metabolism. Nature *524*, 361–365.

Petrovic, N., Walden, T.B., Shabalina, I.G., Timmons, J.A., Cannon, B., and Nedergaard, J. (2010). Chronic peroxisome proliferator-activated receptor gamma (PPARgamma) activation of epididymally derived white adipocyte cultures reveals a population of thermogenically competent, UCP1-containing adipocytes molecularly distinct from classic brown adipocytes. J. Biol. Chem. *285*, 7153–7164.

Politi, Y., Gal, L., Kalifa, Y., Ravid, L., Elazar, Z., and Arama, E. (2014). Paternal mitochondrial destruction after fertilization is mediated by a common endocytic and

autophagic pathway in Drosophila. Dev. Cell *29*, 305–320.

Quan, W., Hur, K.Y., Lim, Y., Oh, S.H., Lee, J.-C., Kim, K.H., Kim, G.H., Kim, S.-W., Kim, H.L., Lee, M.-K., et al. (2012). Autophagy deficiency in beta cells leads to compromised unfolded protein response and progression from obesity to diabetes in mice. Diabetologia *55*, 392–403.

Rawi, Al, S., Louvet-Vallee, S., Djeddi, A., Sachse, M., Culetto, E., Hajjar, C., Boyd, L., Legouis, R., and Galy, V. (2011). Postfertilization Autophagy of Sperm Organelles Prevents Paternal Mitochondrial DNA Transmission. Science *334*, 1144–1147.

Roczniak-Ferguson, A., Petit, C.S., Froehlich, F., Qian, S., Ky, J., Angarola, B., Walther, T.C., and Ferguson, S.M. (2012). The transcription factor TFEB links mTORC1 signaling to transcriptional control of lysosome homeostasis. Sci Signal *5*, ra42.

Rodeheffer, M.S., Birsoy, K., and Friedman, J.M. (2008). Identification of white adipocyte progenitor cells in vivo. Cell *135*, 240–249.

Rodriguez, A., Durán, A., Selloum, M., Champy, M.-F., Diez-Guerra, F.J., Flores, J.M., Serrano, M., Auwerx, J., Diaz-Meco, M.T., and Moscat, J. (2006). Mature-onset obesity and insulin resistance in mice deficient in the signaling adapter p62. Cell Metab. *3*, 211–222.

Romanelli, E., Sorbara, C.D., Nikić, I., Dagkalis, A., Misgeld, T., and Kerschensteiner, M. (2013). Cellular, subcellular and functional in vivo labeling of the spinal cord using vital dyes. Nat Protoc *8*, 481–490.

Rosenwald, M., Perdikari, A., Rülicke, T., and Wolfrum, C. (2013). Bi-directional interconversion of brite and white adipocytes. Nat Cell Biol *15*, 659–667.

Rossmeisl, M., Barbatelli, G., Flachs, P., Brauner, P., Zingaretti, M.C., Marelli, M., Janovská, P., Horáková, M., Syrový, I., Cinti, S., et al. (2002). Expression of the uncoupling protein 1 from the aP2 gene promoter stimulates mitochondrial biogenesis in unilocular adipocytes in vivo. Eur. J. Biochem. *269*, 19–28.

Saeed, A.I., Sharov, V., White, J., Li, J., Liang, W., Bhagabati, N., Braisted, J., Klapa, M., Currier, T., Thiagarajan, M., et al. (2003). TM4: a free, open-source system for microarray data management and analysis. BioTechniques *34*, 374–378.

Saito, M., Okamatsu-Ogura, Y., Matsushita, M., Watanabe, K., Yoneshiro, T., Nio-Kobayashi, J., Iwanaga, T., Miyagawa, M., Kameya, T., Nakada, K., et al. (2009). High incidence of metabolically active brown adipose tissue in healthy adult humans: effects of cold exposure and adiposity. Diabetes *58*, 1526–1531.

Samad, F., Yamamoto, K., Pandey, M., and Loskutoff, D.J. (1997). Elevated expression of transforming growth factor-beta in adipose tissue from obese mice. Mol. Med. *3*, 37–48.

Sanchez-Gurmaches, J., Hung, C.-M., Sparks, C.A., Tang, Y., Li, H., and Guertin, D.A. (2012). PTEN loss in the Myf5 lineage redistributes body fat and reveals subsets of white adipocytes that arise from Myf5 precursors. Cell Metab. *16*, 348–362.

Sardiello, M., Palmieri, M., di Ronza, A., Medina, D.L., Valenza, M., Gennarino, V.A., Di Malta, C., Donaudy, F., Embrione, V., Polishchuk, R.S., et al. (2009). A Gene Network Regulating Lysosomal Biogenesis and Function. Science *325*, 473–477.

Sarraf, S.A., Raman, M., Guarani-Pereira, V., Sowa, M.E., Huttlin, E.L., Gygi, S.P., and Harper, J.W. (2013). Landscape of the PARKIN-dependent ubiquitylome in response to mitochondrial depolarization. Nature *496*, 372–376.

Sato, M., and Sato, K. (2011). Degradation of paternal mitochondria by fertilization-triggered autophagy in C. elegans embryos. Science *334*, 1141–1144.

Schulz, T.J., Huang, T.L., Tran, T.T., Zhang, H., Townsend, K.L., Shadrach, J.L., Cerletti, M., McDougall, L.E., Giorgadze, N., Tchkonia, T., et al. (2011). Identification of inducible brown adipocyte progenitors residing in skeletal muscle and white fat. Pnas *108*, 143–148.

Seale, P., Bjork, B., Yang, W., Kajimura, S., Chin, S., Kuang, S., Scimè, A., Devarakonda, S., Conroe, H.M., Erdjument-Bromage, H., et al. (2008). PRDM16 controls a brown fat/skeletal muscle switch. Nature *454*, 961–967.

Seale, P., Conroe, H.M., Estall, J., Kajimura, S., Frontini, A., Ishibashi, J., Cohen, P., Cinti, S., and Spiegelman, B.M. (2011). Prdm16 determines the thermogenic program of subcutaneous white adipose tissue in mice. J. Clin. Invest. *121*, 96–105.

Sellayah, D., and Sikder, D. (2014). Orexin Restores Aging-Related Brown Adipose Tissue Dysfunction in Male Mice. Endocrinology *155*, 485–501.

Seok, S., Fu, T., Choi, S.-E., Li, Y., Zhu, R., Kumar, S., Sun, X., Yoon, G., Kang, Y., Zhong, W., et al. (2014). Transcriptional regulation of autophagy by an FXR-CREB axis. Nature *516*, 108–111.

Settembre, C., Di Malta, C., Polito, V.A., Arencibia, M.G., Vetrini, F., Erdin, S., Erdin, S.U., Huynh, T., Medina, D., Colella, P., et al. (2011). TFEB Links Autophagy to Lysosomal Biogenesis. Science *332*, 1429–1433.

Settembre, C., De Cegli, R., Mansueto, G., Saha, P.K., Vetrini, F., Visvikis, O., Huynh, T., Carissimo, A., Palmer, D., Klisch, T.J., et al. (2013). TFEB controls cellular lipid metabolism through a starvation-induced autoregulatory loop. Nat Cell Biol *15*, 647–658.

Settembre, C., Zoncu, R., Medina, D.L., Vetrini, F., Erdin, S., Erdin, S., Huynh, T., Ferron, M., Karsenty, G., Vellard, M.C., et al. (2012). A lysosome-to-nucleus signalling mechanism senses and regulates the lysosome via mTOR and TFEB. Embo J *31*, 1095–1108.

Shabalina, I.G., Petrovic, N., de Jong, J.M.A., Kalinovich, A.V., Cannon, B., and Nedergaard, J. (2013). UCP1 in brite/beige adipose tissue mitochondria is functionally thermogenic. Cell Reports *5*, 1196–1203.

Sharp, L.Z., Shinoda, K., Ohno, H., Scheel, D.W., Tomoda, E., Ruiz, L., Hu, H., Wang, L., Pavlova, Z., Gilsanz, V., et al. (2012). Human BAT Possesses Molecular Signatures That Resemble Beige/Brite Cells. PLoS ONE *7*, –e49452.

Shibata, M., Yoshimura, K., Furuya, N., Koike, M., Ueno, T., Komatsu, M., Arai, H., Tanaka, K., Kominami, E., and Uchiyama, Y. (2009). The MAP1-LC3 conjugation system is involved in lipid droplet formation. Biochem. Biophys. Res. Commun. *382*, 419–423.

Shinoda, K., Luijten, I.H.N., Hasegawa, Y., Hong, H., Sonne, S.B., Kim, M., Xue, R., Chondronikola, M., Cypess, A.M., Tseng, Y.-H., et al. (2015). Genetic and functional characterization of clonally derived adult human brown adipocytes. Nature Medicine *21*, 389–394.

Shvets, E., Fass, E., and Elazar, Z. (2008). Utilizing flow cytometry to monitor autophagy in living mammalian cells. Autophagy *4*, 621–628.

Sidossis, L., and Kajimura, S. (2015). Brown and beige fat in humans: thermogenic adipocytes that control energy and glucose homeostasis. J Clin Invest *125*, 478–486.

Singh, R., Kaushik, S., Wang, Y., Xiang, Y., Novak, I., Komatsu, M., Tanaka, K., Cuervo, A.M., and Czaja, M.J. (2009a). Autophagy regulates lipid metabolism. Nature *458*, 1131–1135.

Singh, R., Xiang, Y., Wang, Y., Baikati, K., Cuervo, A.M., Luu, Y.K., Tang, Y., Pessin, J.E., Schwartz, G.J., and Czaja, M.J. (2009b). Autophagy regulates adipose mass and differentiation in mice. J. Clin. Invest. *119*, 3329–3339.

Song, W.-H., Yi, Y.-J., Sutovsky, M., Meyers, S., and Sutovsky, P. (2016). Autophagy and ubiquitin-proteasome system contribute to sperm mitophagy after mammalian fertilization. Proceedings of the National Academy of Sciences *113*, E5261–E5270.

Stotland, A., and Gottlieb, R.A. (2016). alpha-MHC MitoTimer mouse: In vivo mitochondrial turnover model reveals remarkable mitochondrial heterogeneity in the heart. J Mol Cell Cardiol *90*, 53–58.

Subramani, S., and Malhotra, V. (2013). Non-autophagic roles of autophagy-related proteins. EMBO Rep. *14*, 143–151.

Sun, N., Yun, J., Liu, J., Malide, D., Liu, C., Rovira, I.I., Holmström, K.M., Fergusson, M.M., Yoo, Y.H., Combs, C.A., et al. (2015). Measuring In Vivo Mitophagy. Molecular Cell *60*, 685–696.

Sutovsky, P., Moreno, R.D., Ramalho-Santos, J., Dominko, T., Simerly, C., and

Schatten, G. (2000). Ubiquitinated sperm mitochondria, selective proteolysis, and the regulation of mitochondrial inheritance in mammalian embryos. Biol. Reprod. *63*, 582–590.

Terskikh, A., Fradkov, A., Ermakova, G., Zaraisky, A., Tan, P., Kajava, A.V., Zhao, X., Lukyanov, S., Matz, M., Kim, S., et al. (2000). “Fluorescent timer”: protein that changes color with time. Science *290*, 1585–1588.

Thompson, W.E., Ramalho-Santos, J., and Sutovsky, P. (2003). Ubiquitination of prohibitin in mammalian sperm mitochondria: possible roles in the regulation of mitochondrial inheritance and sperm quality control. Biol. Reprod. *69*, 254–260.

Tian, Y., Garcia, G., Bian, Q., Steffen, K.K., Joe, L., Wolff, S., Meyer, B.J., and Dillin, A. (2016). Mitochondrial Stress Induces Chromatin Reorganization to Promote Longevity and UPRmt. Cell *165*, 1197–1208.

van der Lans, A.A.J.J., Hoeks, J., Brans, B., Vijgen, G.H.E.J., Visser, M.G.W., Vosselman, M.J., Hansen, J., Jörgensen, J.A., Wu, J., Mottaghy, F.M., et al. (2013). Cold acclimation recruits human brown fat and increases nonshivering thermogenesis. J. Clin. Invest. *123*, 3395–3403.

van Marken Lichtenbelt, W.D., Vanhommerig, J.W., Smulders, N.M., Drossaerts, J.M.A.F.L., Kemerink, G.J., Bouvy, N.D., Schrauwen, P., and Teule, G.J.J. (2009). Cold-activated brown adipose tissue in healthy men. N Engl J Med *360*, 1500–1508.

Vernochet, C., Peres, S.B., Davis, K.E., McDonald, M.E., Qiang, L., Wang, H., Scherer, P.E., and Farmer, S.R. (2009). C/EBPalpha and the corepressors CtBP1 and CtBP2 regulate repression of select visceral white adipose genes during induction of the brown phenotype in white adipocytes by peroxisome proliferator-activated receptor gamma agonists. Molecular and Cellular Biology *29*, 4714–4728.

Wang, Q.A., Tao, C., Gupta, R.K., and Scherer, P.E. (2013). Tracking adipogenesis during white adipose tissue development, expansion and regeneration. Nature Medicine *19*, 1338–1344.

Wang, W., Kissig, M., Rajakumari, S., Huang, L., Lim, H.-W., Won, K.-J., and Seale, P. (2014). Ebf2 is a selective marker of brown and beige adipogenic precursor cells. Pnas *111*, 14466–14471.

Warr, M.R., Binnewies, M., Flach, J., Reynaud, D., Garg, T., Malhotra, R., Debnath, J., and Passegué, E. (2013). FOXO3A directs a protective autophagy program in haematopoietic stem cells. Nature *494*, 323–327.

Wu, J., Boström, P., Sparks, L.M., Ye, L., Choi, J.H., Giang, A.-H., Khandekar, M., Virtanen, K.A., Nuutila, P., Schaart, G., et al. (2012). Beige adipocytes are a distinct type of thermogenic fat cell in mouse and human. Cell *150*, 366–376.

Xue, B.B., Rim, J.-S.J., Hogan, J.C.J., Coulter, A.A.A., Koza, R.A.R., and Kozak, L.P.L.

(2007). Genetic variability affects the development of brown adipocytes in white fat but not in interscapular brown fat. J Lipid Res *48*, 41–51.

Yadav, H., Quijano, C., Kamaraju, A.K., Gavrilova, O., Malek, R., Chen, W., Zerfas, P., Zhigang, D., Wright, E.C., Stuelten, C., et al. (2011). Protection from obesity and diabetes by blockade of TGF-β/Smad3 signaling. Cell Metab. *14*, 67–79.

Yang, L., Li, P., Fu, S., Calay, E.S., and Hotamisligil, G.S. (2010). Defective Hepatic Autophagy in Obesity Promotes ER Stress and Causes Insulin Resistance. Cell Metab. *11*, 467–478.

Ye, R., Wang, Q.A., Tao, C., Vishvanath, L., Shao, M., McDonald, J.G., Gupta, R.K., and Scherer, P.E. (2015). Impact of tamoxifen on adipocyte lineage tracing: Inducer of adipogenesis and prolonged nuclear translocation of Cre recombinase. Mol Metab *4*, 771–778.

Yoneshiro, T., Aita, S., Matsushita, M., Kayahara, T., Kameya, T., Kawai, Y., Iwanaga, T., and Saito, M. (2013). Recruited brown adipose tissue as an antiobesity agent in humans. J. Clin. Invest. *123*, 3404–3408.

Zhang, J., Randall, M.S., Loyd, M.R., Dorsey, F.C., Kundu, M., Cleveland, J.L., and Ney, P.A. (2009a). Mitochondrial clearance is regulated by Atg7-dependent and -independent mechanisms during reticulocyte maturation. Blood *114*, 157–164.

Zhang, Y., Goldman, S., Baerga, R., Zhao, Y., Komatsu, M., and Jin, S. (2009b). Adipose-specific deletion of autophagy-related gene 7 (atg7) in mice reveals a role in adipogenesis. Proceedings of the National Academy of Sciences *106*, 19860–19865.

Publishing Agreement

It is the policy of the University to encourage the distribution of all theses, dissertations, and manuscripts. Copies of all UCSF theses, dissertations, and manuscripts will be routed to the library via the Graduate Division. The library will make all theses, dissertations, and manuscripts accessible to the public and will preserve these to the best of their abilities, in perpetuity.

Please sign the following statement:

I hereby grant permission to the Graduate Division of the University of California, San Francisco to release copies of my thesis, dissertation, or manuscript to the Campus Library to provide access and preservation, in whole or in part, in perpetuity.



Author Signature

11/21/2016

Date